Departament of
Life Sciences

NOVA SCHOOL OF
SCIENCE & TECHNOLOGY

Daniela Silva Felício

BSc in Biomedical Sciences

Functional characterization of a new TTBK2 variant in spinocerebellar ataxia type 11

Master in Molecular Genetics and Biomedicine

NOVA University Lisbon

November, 2021

DEPARTAMENT OF
LIFE SCIENCES

Functional characterization of a new TTBK2 variant in spinocerebellar ataxia type 11

Daniela Silva Felício

BSc in Biomedical Sciences

Adviser: Mariana Santos Moreda Graça
Junior Researcher, i3S/IBMC, University of Porto

Co-advisers: Margarida Casal Ribeiro Castro Caldas Braga
Assistant Professor, School of sciences and Technology of NOVA University Lisbon

Examination Committee:

Chair: Maria Alexandra Núncio de Carvalho Ramos Fernandes
Assistant Professor, School of Sciences and Technology of NOVA University Lisbon

Adviser: Mariana Santos Moreda Graça
Junior Researcher, i3S/IBMC, University of Porto

Members: Filipa Sá Martins
Post-Doctoratal Researcher, Institute of Biomedicine (iBiMED), University of Aveiro

Master in Molecular Genetics and Biomedicine

NOVA University Lisbon
November, 2021

Functional Characterization of a New TTBK2 Variant in Spinocerebellar Ataxia Type 11

Part of the results discussed in this thesis were presented in the following conference and meeting:

Poster communications:

Felício, Daniela; Sequeiros, Jorge; Santos, Mariana (2021) Modelling SCA11 in cells using CRISPR/Cas9: functional validation of a new TTBK2 missense variant. European Human Genetics (ESHG) Conference 2021, 28-31 August 2021 (Virtual Conference).

Oral communications:

Felício, Daniela; Santos, Mariana (2021) Functional characterization of a new TTBK2 variant in spinocerebellar ataxia type 11. Conference of the Annual Masters' Dissertations of the Departments of Chemistry and Life Sciences 2021, 11 February 2021 (Virtual Conference).

This work was performed in UnIGENe Group, at i3S – Instituto de Investigação e Inovação em Saúde. It was supported by the small research grant ZGRACA - "Modelling SCA11 in cultured cells using CRISPR/Cas9", Ataxia UK, United Kingdom.

ACKNOWLEDGMENTS

Primeiramente, quero agradecer ao mestrado em Genética Molecular e Biomedicina (UNL-FCT) e ao grupo UnIGENe (i3S) por me terem proporcionado esta oportunidade que me levou a aprofundar os meus conhecimentos e ganhar experiência numa área que tanto gosto, a genética molecular.

Aos meus colegas de laboratório, um grande obrigado por me terem acompanhado ao longo deste ano.

À professora Dra. Margarida Braga agradeço todo apoio e disponibilidade durante toda esta etapa.

Um agradecimento especial à minha orientadora Mariana que me aceitou neste projeto e esteve sempre disposta a transmitir-me a sua experiência e conhecimentos. Muito obrigado pela confiança, paciência, conselhos e companhia amiga.

E ainda, não me posso esquecer dos meus amigos e família pelo amor, coragem e apoio durante esta jornada.

“Every moment is a fresh beginning.”
(T.S. Eliot).

“Life is a succession of lessons which must be lived to be understood.”
(Helen Keller).

ABSTRACT

Spinocerebellar ataxia type 11 (SCA11) is an autosomal dominant cerebellar ataxia caused by heterozygous frameshift variants in the tau-tubulin kinase (*TTBK2*) gene. However, *TTBK2* missense variants are still not clearly associated with the disease. TTBK2 have been reported to regulate proteins related to neurodegeneration (e.g., TDP-43), microtubules (e.g., KIF2A), ciliogenesis (e.g., CEP164), transporters and receptors (e.g., BGT1 and GluK2). Currently, the pathological mechanisms behind SCA11 are not fully understood.

In this study, the creation and validation of a CRISPR/Cas9 cellular model allowed to associate for the first time a *TTBK2* (c.625C>T; p.L209F) missense variant with a decrease in TTBK2 protein expression and a loss-of-function effect, affecting TDP-43 phosphorylation. Moreover, alterations in autophagy markers and microtubule associated proteins were observed. The phosphoproteome data suggests a dysregulation of gene expression, translation and cytoskeleton related pathways, as well as an indication of a possible involvement of SMAD2 and SMAD4 in SCA11 pathogenesis.

Overall, the TTBK2 missense variant seems to dysregulate microtubule, transcription and autophagy, which may affect neuronal morphogenesis and axonal transport. Further experiments must be done to find the degradation pathway responsible for TTBK2 decreased levels, understand the variant influence on autophagy, and search for other interactors in pathways linked to neurodegeneration.

Keywords: Spinocerebellar ataxia type 11 (SCA11); Tau-tubulin kinase 2 (TTBK2); CRISPR/Cas9; Microtubule dynamics; Autophagy; Phosphoproteomics.

RESUMO

A ataxia espinocerebelosa tipo 11 (SCA11) é uma ataxia cerebelosa autossómica dominante progressiva causada por variantes *frameshift* no gene Tau-tubulina cinase (*TTBK2*). Contudo, as variantes *missense* na TTBK2 ainda não estão claramente associadas à doença. A TTBK2 foi associada com a neurodegenerescência, microtúbulos, ciliogénese, canais e recetores. Os mecanismos de patogenicidade responsáveis pela SCA11 ainda não são totalmente compreendidos.

Neste estudo, a criação e validação de um modelo celular CRISPR/Cas9 permitiu associar pela primeira vez uma variante *missense* da TTBK2 (c.625C> T; p.L209F) a um efeito de perda de função, afetando a fosforilação da TDP-43. Além disso, foram observadas alterações em marcadores de autofagia e proteínas associadas aos microtúbulos. Os dados do fosfoproteoma sugerem uma desregulação das vias que regulam a expressão genética, tradução e citoesqueleto, bem como indicam um possível envolvimento de SMAD2 e SMAD4 na patogénese da SCA11.

Concluindo, a variante *missense* da TTBK2 parece desregular os microtúbulos, a transcrição e a autofagia, provavelmente afetando a morfogénese neuronal e o transporte axonal. Experiências adicionais devem ser feitas para encontrar a via de degradação responsável pela redução dos níveis de TTBK2, entender a sua influência na autofagia e procurar outros interatores nas vias associadas à neurodegenerescência.

Palavras chave: Ataxia espinocerebelosa tipo 11 (SCA11); Tau-tubulina cinase 2 (TTBK2); CRISPR/Cas9; Dinâmica dos microtúbulos; Autofagia; Fosfoproteómica.

CONTENTS

LIST OF FIGURES

LIST OF TABLES

ABBREVIATIONS

+TIP	Plus-end tracking protein
AD	Alzheimer's disease
ADCA	Autosomal dominant cerebellar ataxia
AFG3L2	ATPase family gene 3-like 2
ALS	Amyotrophic lateral sclerosis
ANOVA	Analysis of variance
AOA	Ataxia with ocular apraxia
APTX	Aprataxin
ARCAs	Autosomal recessive cerebellar ataxias
ARE	Antioxidant response element
AT	Ataxia-telangiectasia
Atg7	Autophagy Related 7
ATM	Ataxia-telangiectasia mutated
ATN1	Atropine-1
AVED	Ataxia with vitamin E deficiency
BCA	Bicinchoninic acid
BGT1	Betaine/GABA transporter 1
BP	Biological Process
BRCA1	Breast cancer 1
BSA	Bovine serum albumin
CACNA1A	Calcium voltage-gated channel subunit alpha1 A
CACNB4	Calcium Voltage-Gated Channel Auxiliary Subunit Beta 4
CC	Cellular Component
CCDC92	Coiled-Coil Domain Containing 92
CCFS	Composite Cerebellar Functional Severity Score
CDK1	Cyclin-dependent kinase 1
cDNA	Complementary DNA
CEP	Centrosomal Protein
CK1	Casein kinase
CMA	Chaperone mediated autophagy
CNS	Central nervous system
CP110	Centriolar coiled-coil protein
CRISPR	Clustered Regularly Interspaced Short Palindromic Repeats
CTIF	Cap Binding Complex Dependent Translation Initiation Facto
DA	Distal appendages
DMEM	Dulbecco's Modified Eagle Medium

DNA	Deoxyribonucleic acid
DRPLA	Dentatorubral-pallidoluysian atrophy
DVL2/3	Dishevelled 2/3
EA	Episodic ataxia
EAAT1	Excitatory amino acid transporter 1
EB	End Binding Protein
ECL	Enhanced chemiluminescence
EOCA	Early onset cerebellar ataxia
ER	Endoplasmic reticulum
ERAD	ER-associated protein degradation
FACS	Fluorescence-activated cell sorting
FBS	Fetal bovine serum
FDR	False discovery rate
FGF14	Fibroblast Growth Factor 14
FHM1	Familial hemiplegic migraine 1
FMR1	Fragile X mental retardation 1
FRDA	Friedreich ataxia
FTDP-17	Frontotemporal dementia and parkinsonism linked to chromosome 17
FTLD	Frontotemporal lobar dementia
FXN	Frataxin
FXS	Fragile X syndrome
GABA	γ-aminobutyric acid
GAD	Anti-glutamic acid decarboxylase
GluK2	Glutamate (kainate) receptor subunit 2
GM130	Cis-Golgi matrix protein 130 kDa
GMR1	Glutamate metabotropic receptor 1
GO	Gene Ontology
GSEA	Gene Set Enrichment Analysis
GSK-3β	Glycogen synthase kinase 3
H3F3A	H3 histone, family 3A
HD	Huntington's disease
HDAC	Histone Deacetylase
HDR	Homology-directed repair
HEK293T	Human embryonic kidney 293 incorporated with SV40 large T antigen cells
HIST2H3C	Histone cluster 2 H3 family member c
HRP	Horseradish peroxidase
HSC70	Heat shock cognate 71 kDa protein
ICARS	International Cooperative Ataxia Rating Scale
IDRs	Intrinsically disordered regions
IFT	Intraflagellar transport
Ig	Immunoglobulin
ILK	integrin linked kinase
ILOCA	Idiopathic late onset cerebellar ataxia
KCNA1	Potassium Voltage-Gated Channel Subfamily A Member 1
KD	Kinase dead
Keap1	Kelch-like ECH-associated protein 1
KIF	kinesin family member
LAMP1	Lysosomal-associated membrane protein 1
LC3B	Microtubule-associated protein 1A/1B-light chain 3
LC-MS/MS	Liquid Chromatography with tandem mass spectrometry

LFQ	Protein-label-free quantitation
LHON	Leber hereditary optic neuropathy
LIMS1	LIM zinc finger domain containing 1
MAP	Microtubule associated protein
MAPK	Mitogen-activated protein kinase
MARK4	MAP/microtubule affinity-regulating kinase 4
MELAS	Mitochondrial encephalopathy, lactic acidosis, and stroke-like episodes
MERRF	Myoclonic epilepsy with ragged red fibers
MF	Molecular Function
MJD	Machado-Joseph disease
MPP9	M-Phase Phosphoprotein 9
MRI	Magnetic resonance imaging
mRNA	Messenger RNA
MS/MS	Tandem mass spectrometry
MSA	Multiple system atrophy
mtDNA	Mitochondrial DNA
mTOR	Mammalian target of rapamycin
MW	Molecular weight
NARP	Neuropathy, Ataxia, and Retinitis Pigmentosa
NDD	Neurodegenerative disease
nDNA	Nuclear DNA
NEDD4L	Neuronal precursor cell expressed developmentally downregulated 4-like
NES	Normalised Enriched score
NHEJ	Non-homologous end joining
NMD	Nonsense-mediated decay
Nrf2	Nuclear factor (erythroid-derived 2)-like 2
ORA	Over-Representation Analysis
PAM	Protospacer adjacent motif
PARVA/B	Parvin alpha or beta
PBS	Phosphate buffered saline
PC	Primary cilium
PCR	Polymerase chain reaction
PD	Parkinson’s disease
PDB	Protein Data Bank
PET	Positron emission tomography
PIP	PINCH–ILK–parvin
PKACα	Protein kinase A catalytic subunit alpha
PMID	PubMed reference number (ID)
PNKP	Polynucleotide kinase 3'-phosphatase
polyQ	Polyglutamine
PVDF	Polyvinylidene fluoride
RT-qPCR	Reverse-transcription quantitative polymerase chain reaction
Raptor	Regulatory-associated protein of mTOR
RIPA	Radioimmunoprecipitation assay
RNA	Ribonucleic acid
ROS	Reactive oxygen species
RT	Room temperature
SARA	Scale for the Assessment and Rating of Ataxia
SCA	Spinocerebellar ataxia
SCAFI	SCA Functional Index

SD	Standard deviation
SDS	Sodium dodecyl sulfate
SDS-PAGE	SDS-polyacrylamide gel electrophoresis
SETX	Senataxin
SGK1	Serum/Glucocorticoid Regulated Kinase 1
SGLT1	Sodium-coupled Glucose Transporter 1
sgRNA	Single-chain guide RNA
SHh	Sonic hedgehog
SIRT2	Sirtuin 2
SLIT2	Slit guidance ligand 2
SMAD	Mothers against decapentaplegic homolog
SPECT	Single-photon emission computed tomography
SQSTM1/p62	Sequestosome 1
ssODN	Single-stranded oligodeoxynucleotide
SV2A	Synaptic vesicle protein 2A
SxIP	Serine any amino acid isoleucine proline
TAK1	Transforming growth factor beta-activated kinase 1
TBS-T	Tris-buffered saline-Tween 20
TDP-43	transactive response DNA-binding protein 43 kDa
TGF-β	Transforming growth factor beta
TTBK	Tau-tubulin kinase
ULK1	Unc-51 Like Autophagy Activating Kinase 1
UPR	Unfolded protein response
UPS	Ubiquitin–proteasome system
VRK	Vaccinia-related kinase
XLCAs	X-linked cerebellar ataxias
αTAT1	α-tubulin acetyltransferase 1

1 INTRODUCTION

Neurodegenerative diseases (NDDs) are a group of life-threatening or chronically debilitating disorders caused by pathogenic genetic variants (i.e., mutations), harmful environmental exposures during embryonic development or later in life, brain tumours, autoimmune or infectious diseases[1]. Neurodegeneration usually affects the cerebral cortex, thalamus, hypothalamus brain stem and/or cerebellum, resulting in a progressive neuronal loss within the central nervous system (CNS) (Figure 1.1)[1,2]. In addition, involvement of the peripheral nervous system is also relatively common in some NDDs[1,2].

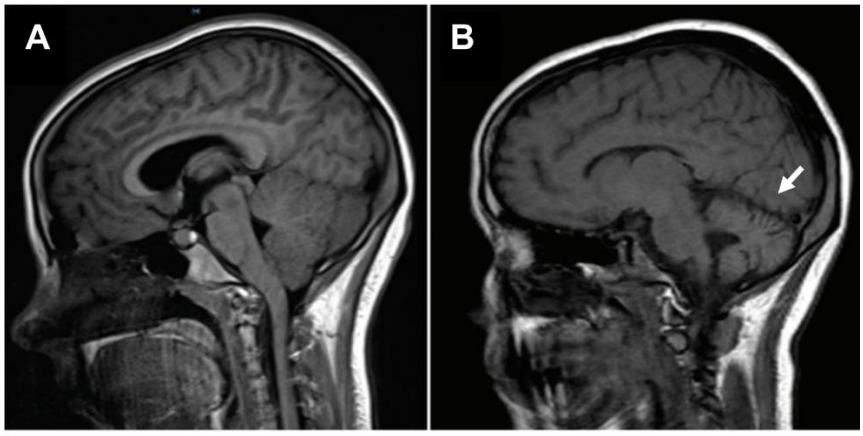

Figure 1.1 Brain magnetic resonance imaging (MRI) showing progressive cerebellar atrophy. In a female Caucasian diagnosed with autoimmune anti-glutamic acid decarboxylase (GAD) associated cerebellar ataxia was acquired brain MRI, sagittal view, T1-weighted image obtained at (A) the disease onset and (B) follow-up at 6 months. Adapted from Gomez, J. and Jin, D. (2019)[3].

1.1 Cerebellar Ataxias

The term *ataxia*, meaning “absence of order”, designate specific neurological diseases primarily characterised by gait imbalance, and decreased coordination[2,4]. These symptoms result mainly from impairment of the cerebellum, responsible for motor planning and limb control, and the midline vermis, which controls motor execution, balance, gait, and ocular movements (Figure 1.2)[5]. Consequently, occurs the dysfunction of Purkinje cells which receive excitatory input mainly from granule cells (via mossy

fibers) and the inferior olive (via climbing fibers), being responsible for the inhibitory regulation of cerebellar nuclei neurons through the neurotransmitter γ-aminobutyric acid (GABA) (Figure 1.2)[5,6].

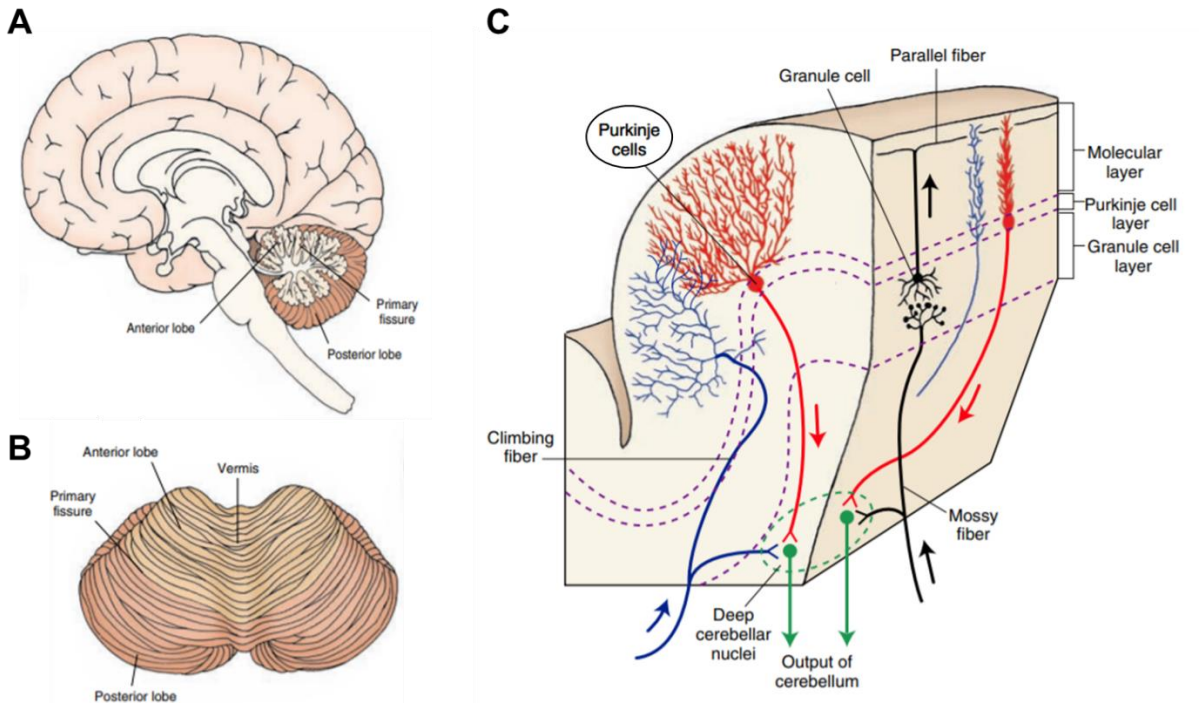

Figure 1.2 Structure and organization of the cerebellum. Superior (A) and midsagittal (B) views of the cerebellum, presenting the cerebellar hemispheres and vermis along with the anterior and posterior lobes. (C) Basic organization and circuitry of the cerebellar cortex. Adapted from Siegel, A. and Sapru, H. (2011) (Figure 11.7 and 21.8)[7].

There is evidence that in cerebellar ataxias exists a pre-ataxia period of several years that is characterized by mild coordination deficits, non-ataxia symptoms and the start of brainstem and cerebellum degeneration[8]. So, in most cases, the first abnormality identified is gait unsteadiness, and as ataxia progresses, the coordination deteriorates, resulting in intention tremor, dysarthria, dysphagia, nystagmus, and the loss of fine motor skills. Moreover, sleep disorders (such as restless leg syndrome and rapid eye movement sleep behaviour disorder), cerebellar cognitive affective syndrome, dementia and depression may also occur in cerebellar ataxia patients[8]. In some systemic cerebellar ataxias, it may appear gastrointestinal problems, autonomic dysfunction, dizziness, spasticity, neuropathy, dystonia, and parkinsonism[5].

In the early twentieth century, neuropathological classification for cerebellar ataxias was introduced: olivo-pontocerebellar atrophy, cerebello-olivary atrophy or spinocerebellar degeneration[2]. However, as pathological data were not always available and several families showed clinical heterogeneity, Harding proposed a classification based on the age of onset, mode of transmission and clinical signs: (1) early onset cerebellar ataxia (EOCA) with age of onset before 20 years and usually with autosomal recessive (AR) transmission; (2) autosomal dominant cerebellar ataxia (ADCA) with adult onset that comprises ADCA type I – ataxias with ophthalmoplegia, optic atrophy, dementia, extrapyramidal features and/or

amyotrophy, ADCA type II – ataxias with retinal degeneration, ophthalmoplegia, with or without dementia and extrapyramidal features, and ADCA type III – ataxias with pure cerebellar symptoms; (3) idiopathic late onset cerebellar ataxia (ILOCA)[2].

Still, nowadays, as cerebellar ataxias comprise disorders of both genetic and non-genetic causes, there are two main categories: hereditary (dominant, recessive, mitochondrial and x-linked inheritance) and sporadic ataxias, the latter being of acquired or idiopathic nature[4].

1.1.1 Hereditary Ataxias

Hereditary ataxias comprise about 60–75% of ataxias, and can present with autosomal dominant, autosomal recessive, X-linked or mitochondrial inheritance[1].

1.1.1.1 Autosomal Dominant Ataxias

The autosomal dominant cerebellar ataxias (ADCAs), also named spinocerebellar ataxias (SCAs), are a heterogeneous group that also includes the complex ataxia dentatorubral-pallidoluysian atrophy (DRPLA) and nine episodic ataxias (EAs)[1,9]. In some SCAs, progressive loss of balance, coordination and dysarthria are the only findings (e.g., SCA6), whereas others may present non-ataxic signs (e.g., SCA1, SCA3, SCA7 and DRPLA), such as spasticity, amyotrophy, parkinsonism, dystonia, chorea, epilepsy, oculomotor, and muscle abnormalities[8]. In ataxias due to conventional mutations, the age of onset tends to be earlier (childhood or early adulthood) with a slower progression and a more benign course than in the repeat expansion ataxias, which typically start in mid or later adulthood with the presentation of extra-cerebellar signs[9]. Clinical variation exists between genotypes, within genotypes and even within families. Their prevalence is estimated to be approximately 1-5:100,000 population[10], being SCA3/Machado-Joseph disease (SCA3/MJD) the most common worldwide (20-50% of families with SCA), followed by SCA2 (13-18%), and SCA6 (13-15%)[8]. SCA3/MJD is caused by CAG coding repeats in the ataxin *3* gene, a deubiquitinase that participates in protein quality control. Interestingly, the different SCA subtypes shows marked geographical and ethnic variability, due to founder effects[8].

Regarding SCAs, 48 SCA types were described, numbered from SCA1 to SCA48 in the chronological order in which the disease locus of the subtype was identified[6]. However only 43 loci have been identified since SCA9 and SCA33 are unassigned, SCA15, 16 and 29 were linked to the same chromosomal locus, and SCA24 proved to be recessively inherited. The genetic background of the SCAs revealed several underlying mutational mechanisms (Figure 1.3): (1) classical mutations, such as missense mutations (e.g., SCA13), frameshift mutations (e.g., SCA11), deletions (e.g., SCA15) and duplications (e.g., SCA20); (2) coding repeat expansions of CAG (glutamine-codon) triplets (e.g., SCA1-3, 6, 7, 17, DRPLA), also referred to as polyglutamine (polyQ) expansions because their translation produces monomers and oligomers of polyglutamine proteins; (3) other triplet coding repeat expansion (e.g., SCA8, where a CTG expansion is transcribed in both directions, provoking the transcription and the translation of a CAG repeat in the antisense strand, also generating a polyQ protein); (4) noncoding triplet, quintuplet or hexaplet repeat expansions (e.g., SCA10, 12, 31, 36, 37), which primarily cause

disease at the RNA level, and tend to be much larger expansions compared to CAG repeats[2,8]. Although other SCAs have been successfully linked to distinct genetic loci, the disease gene and/or the causative mutations are still unknown for SCA4, SCA18, SCA25, SCA30, SCA32, and SCA39.

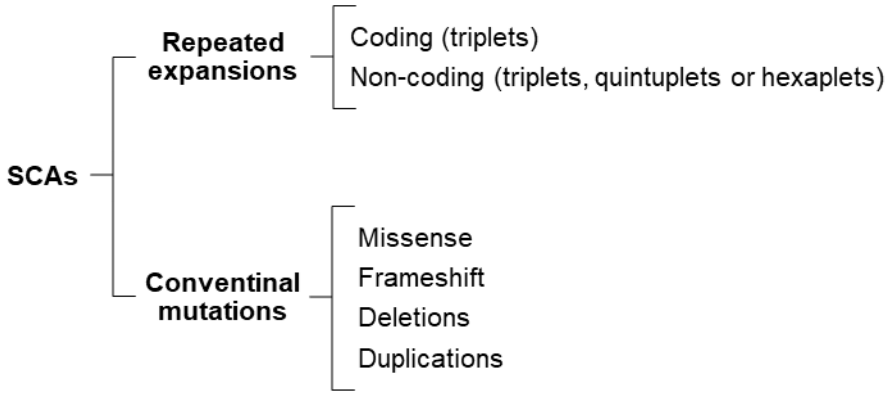

Figure 1.3 SCAs division according to the underlying mutations.

The polyQ ataxias are the most common SCAs, found in approximately 50% of families with dominant ataxia, while noncoding repeats and conventional mutations have been identified in a smaller number of cases of ataxia[8]. Among the SCAs due to conventional mutations, the most frequent forms are SCA14 and SCA28. A substantial percentage of SCA-affected families have no identifiable genetic defect (30-48%), indicating a set of ataxias yet to be characterised[8].

A typical aspect of repeat expansion ataxias is the instable or “dynamic” nature of the expanded sequence, which leads to clinical “anticipation”, i.e., an earlier onset of the clinical manifestations in affected offspring due to a further expansion of the triplet repeat[8,11]. So, the age of onset inversely correlates with the length of the expanded repeat. However, the length of the expanded repeat explains only about 50% of age at onset, suggesting that other factors may also participate. Also, the phenotype tends to be dependent on the repeat expansion size, i.e., larger expansions typically cause a more severe phenotype[8,11].

The EAs differentiates from SCAs due to the episodic occurrence of symptoms, existing an intermittent (i.e., minutes to hours) unsteady gait, often associated with nystagmus or dysarthria[12]. Permanent ataxia and even cerebellar atrophy may be seen late in the disease course[5]. There are nine EA subtypes, numbered from EA1 to EA9 with mutations identified in five genes (potassium voltage-gated channel subfamily A member 1 *(KCNA1),* calcium voltage-gated channel subunit alpha1 A *(CACNA1A),* calcium voltage-gated channel auxiliary subunit beta 4 *(CACNB4),* excitatory amino acid transporter 1 *(EAAT1),* and fibroblast growth factor 14 *(FGF14)*)[12]. Although most have been successfully linked to distinct genetic loci, the disease gene and/or the causative mutations are still unknown for EA3, 4 and 7.

The DRPLA caused by a CAG repeat expansion in the atropine-1 (*ATN1*) gene, a transcriptional co-repressor, is classified as SCA given its clinical features of progressive ataxia, myoclonus, epilepsy, choreoathetosis, seizures, dystonia, and dementia[2,5]. As in other polyQ diseases, “anticipation” occurs frequently, and typically larger expansions cause an earlier onset (before age 20) and a more severe

phenotype, whereas smaller expansions lead to an older onset and development of ataxia accompanied by choreoathetosis and dementia[5,11].

1.1.1.2 Autosomal Recessive Ataxias

The autosomal recessive cerebellar ataxias (ARCAs) include a group of genetically and clinically heterogeneous disorders, characterized by cerebellum and spinal cord impaired development or degeneration[13]. More than 50 ARCAs represent loss-of-function variants implicated in mitochondrial metabolism, calcium homeostasis and DNA repair, and most of them were only reported in 1 to 5 families[13]. Typically, in ARCAs there is an early onset characterized by ataxia, dysarthria, and pyramidal signs, however many of them present particular phenotypes and multisystemic manifestations[14]. In this group, the Friedreich ataxia (FRDA) and ataxia-telangiectasia (AT) are the most common, with a prevalence of 1:50000 and 1:100000 individuals, respectively[14]. FRDA is caused by a GAA repeat expansion within the frataxin (*FXN*) gene and AT derives from variants in the ataxia telangiectasia mutated (*ATM*) gene, altering the mitochondrial iron metabolism and DNA repair, respectively[13,14].

Recently, ARCAs were classified in six subtypes based on genetic and pathophysiological criteria: primary autosomal recessive cerebellar ataxias, congenital ataxias, ataxias associated with metabolic disorders, ataxias with a DNA repair defect, degenerative ataxias, and ataxia associated with other features[15]. But the classification criteria remain controversial, and the recessive disorders included in this category still need further assessment. Moreover, diseases in which cerebellar involvement is a minor or late finding in a multisystem phenotype or ones that are already classified on their own, such as the congenital Joubert syndrome, were excluded. An important future challenge will be addressing the issue of a proper nomenclature system[15] .

1.1.1.3 X-linked and Mitochondrial Inherited ataxias

X-linked cerebellar ataxias (XLCAs) are a group of heterogeneous disorders caused by genomic imbalances or gene variations on the X chromosome genes and generally involved in brain development and synaptic function[16] . The XLCAs present developmental delay, intellectual disability, ataxia, and other disease specific features like mild facial anomalies, sensorineural deafness and macro-orchidism[16]. These disorders are quite rare, except for fragile X syndrome (FXS) with an estimated prevalence of 1,4:10000 males[17]. This disorder is caused by CGG triplet expansions in the 5'untranslated region of the fragile X mental retardation 1 (*FMR1*) gene, a synaptic regulator, which causes loss of neuronal plasticity and intellectual disability[16,17].

Furthermore, cerebellar ataxia is found in many mitochondrial diseases because, as a highly metabolically active structure, the cerebellum may be affected by mitochondrial disfunction[18]. Mitochondrial diseases are divided into disorders due to primary mitochondrial DNA (mtDNA) mutations and disorders due to abnormalities of mitochondrial-related nuclear genes (nDNA)[18,19]. In a study was found that mitochondrial diseases in adults have a prevalence of 9,6 and 2,9 per 100000 individuals in case of mu-

tation in mtDNA and nDNA, respectively[19]. So, mtDNA mutations seem to cause most of the mitochondrial diseases in adults, while childhood-onset ones are normally caused by autosomal recessive mutations in nDNA[19]. Examples of mitochondrial diseases with associated ataxia caused by mtDNA mutations include myoclonic epilepsy with ragged red fibers (MERRF), mitochondrial encephalopathy, lactic acidosis, and stroke-like episodes (MELAS), neuropathy, ataxia, and retinitis pigmentosa (NARP), Leber hereditary optic neuropathy (LHON), Kearns-Sayre and Leigh syndrome[1,18]. As multisystemic disorders, it is essential to discriminate mitochondrial aetiology by observing the presence of ophthalmoplegia, elevated lactic acid in the cerebrospinal fluid, and other features, like deafness[18,19].

Still, there is very few information about the mechanisms underlying the neurodegeneration in XLCAs and mitochondrial diseases.

1.1.2 Sporadic or Nonhereditary Ataxias

Sporadic ataxias have a diverse aetiology but are mainly divided in acquired and idiopathic disorders[1]. Acquired ataxias are due to structural lesions or malformations in the cerebellum, trauma, toxics, endocrine dysfunction, diabetes, gastrointestinal disorders, vitamin E or B12 deficiencies, abetalipoproteinemia, neoplasia, demyelinating, autoimmune and infection diseases, among others[1,5].

Idiopathic ataxias include ILOCA and multiple system atrophy (MSA)[1,5]. MSA is the most common cause of isolated late-onset cerebellar ataxia with a prevalence of about 4 cases per 100000 individuals, and a mean survival of 6–9 years[1,20]. It is a α-synucleopathy with glial cytoplasmatic inclusions in the CNS, and presents autonomic and urinary dysfunction, parkinsonism, and cerebellar signs[1,5]. Additional symptoms may be hyperreflexia, myoclonus, and facial dystonia, among others. Moreover, MSA can be classified as parkinsonian or cerebellar depending on the symptoms, being the first one more predominant (80%)[1,5].

Intriguingly, the clinical and neuropathological findings are often indistinguishable between inherited and the sporadic ataxias, suggesting an overlap of pathological mechanisms[1].

1.1.3 Differential Diagnosis

The key elements for the diagnosis of cerebellar ataxia include the onset age, time course and progression, and medical, social, and family history of the patient[5,11]. In children, congenital and hereditary ataxias as well as metabolic, infectious, or neoplastic brain diseases are often part of the differential diagnosis, whereas in adults, the sporadic and hereditary ataxias are most common. A hereditary form of ataxia is suggested by a slowly progressive neurodegeneration, and symmetrical findings. To distinguish between dominant or recessive inheritance, the main factors are the family history and age of onset. A positive family history of ataxia or gait imbalance in a patient's progenitors, and an adulthood onset strongly suggests a dominantly inherited disorder. In other hand, the absence of a family history of ataxia and an early onset, suggest a recessive form of ataxia[5,11].

The general physical assessment should help to screen for specific features of some cerebellar ataxias such as orthostatic hypotension in MSA; thyroid, eyes and cardiac dysfunctions in for FRDA;

and endocrine and skin defects in AT[5]. During the neurological examination, there should be particular attention on cerebellar functionality by analysing speech, ocular abnormalities, limb coordination, stance, and gait. Besides that, non-cerebellar symptoms like cognitive deficits, dementia, peripheral neuropathy, and movement disorders (parkinsonism, dystonia, and myoclonus) should be examined[5]. This way, a combination of cerebellar features and anomalies in other systems may provide diagnostic clues and help to direct the molecular genetic testing[5,21]. Also, neuroimaging techniques, such as the brain MRI, allow to exclude non-genetic causes of ataxia (e.g., multiple sclerosis, cerebrovascular disease, congenital disorders, or brain tumours) by identifying spinal, olivopontocerebellar and cortical cerebellar atrophy[8,21]. In addition, metabolic studies may be done recurring to positron emission tomography (PET) and the single-photon emission computed tomography (SPECT) scans[21].

The clinical evaluation of cerebellar ataxia may involve the utilization of scales, which assesses ataxia symptoms severity and disease progression[5]. Currently, the most widely used is the scale for the assessment and rating of ataxia (SARA) which evaluates gait, stance, sitting, speech, and limb movements, and can be complemented by performance tests[5,8]. Other ataxia assessment scoring methods are the SCA functional index (SCAFI), the composite cerebellar functional severity score (CCFS) and the international cooperative ataxia rating scale (ICARS)[5].

The genetic screening to search known, novel disease-associated genes or pathogenic variants is crucial to confirm the clinical diagnosis. A systematic approach is recommended for the genetic diagnosis, where a suggestive clinical phenotype of an autosomal dominant or recessive cerebellar ataxia point to an initial screening for polyQ (SCA1, 2, 3, 6, 7, 17 and DRPLA) expansions, or FRDA and AT, respectively, given their high prevalence[8,11,21]. In case of known family genotype, high regional prevalence, a targeted gene test may be suitable[8]. Other genetic causes can be screened on a targeted gene basis to search for known ataxia-genes or expansions using exome or genome sequencing[8,11]. A genetic testing must also be considered in patients with sporadic ataxia and without a family history of ataxia because these patients might have a *de novo* mutation, reduced penetrance of the mutation, or the parents may have been misattributed or died before ataxia symptoms manifested[8]. A resumed flowchart of the approach used to diagnose cerebellar ataxia patients can be found in Figure 1.4.

After the symptomatic patient has been counselled on the potential consequences of the results, both positive and negative, and the genetic diagnosis is made, there may be the need to assist other family members in obtaining predictive testing[8,11]. Even when there is no treatment available, as with the SCAs, establishing a specific diagnosis can permit an informed discussion of the prognosis, available therapies, and the genetic risk within the family members[8,11].

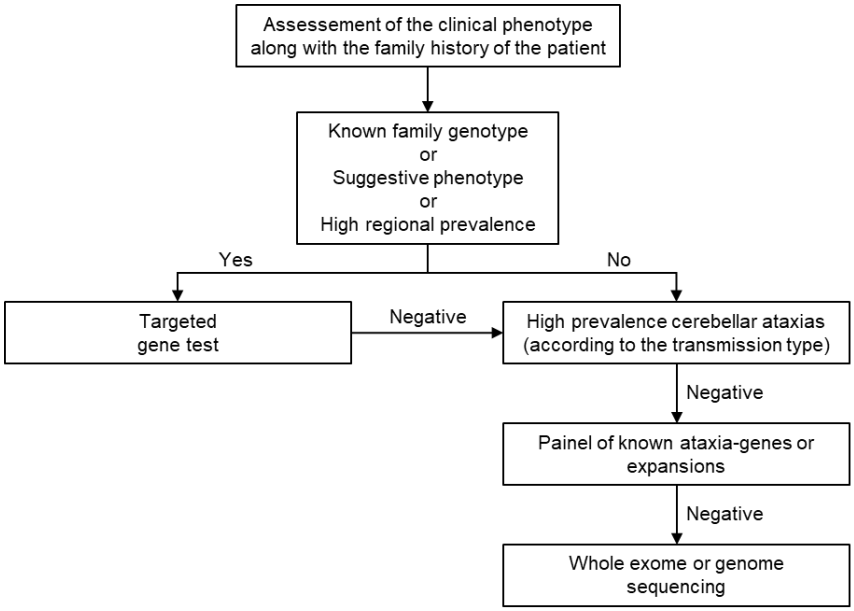

Figure 1.4 General flow-chart for molecular genetic diagnosis of cerebellar ataxias.

1.1.4 Management and Therapies

Currently, no approved pharmacological treatments are available for routine use in patients with cerebellar ataxia, except episodic ataxia that can be treated with aminopyridines and acetazolamide[22]. In non-hereditary ataxias such as ataxia with vitamin E deficiency (AVED) the symptoms can also be improved by vitamin E supplementation[22]. Additionally, some symptoms as gait and balance can ameliorate by rehabilitation through physiotherapy (conventional exercises, computer-assisted training, treadmill training and/or biofeedback therapy), occupational therapy, and speech therapy[8,22].

The main problem in finding effective therapies for cerebellar ataxias is their heterogeneity, which leads to a need for specific therapeutics focused on genotypes/affected disease mechanisms[8]. Thus, some potential pharmacological treatments that targets specific ataxia and non-ataxia-associated symptoms are being tested[8]. An example is the encouraging results on several ion channel modulators, such as riluzole, valproic acid and 4-aminopyridine, which could have symptomatic benefit and even alter the course of disease in SCAs characterised by an ion-channel dysfunction[8,22]. In addition, gene therapies are being tested, for example, through the viral delivery of small interfering RNAs or microRNAs to the CNS[8,23]. These can be used to silence or reduce the expression of the mutated gene, transcript, or protein[8]. Also, antisense oligonucleotides or other small molecules have already been successfully tested to selectively target repeat expansions[8,23].

1.1.5 Pathogenic Mechanisms Behind Neurodegeneration in Cerebellar Ataxias

The cerebellar atrophy along with cellular degeneration and loss, especially the Purkinje cell layer, is the main neuropathological feature of cerebellar ataxias[24]. So, during disease progression the neurons present "dark cell degeneration" characterised by apoptotic and necrotic features along with cellular shrinkage, protein aggregates, dysmorphic mitochondria, and endoplasmic reticulum (ER)[24].

Scientific research has identified several cellular and molecular processes underlying these pathologic aspects, including transcriptional dysregulation, protein aggregation and clearance, autophagy, alterations of calcium homeostasis, mitochondria defects, and apoptosis[8,24]. However, the reason why all these mechanisms lead to cerebellar Purkinje cell death remains largely elusive. The diversity of altered genes in cerebellar ataxias may trigger cell death by affecting different levels of the same cellular processes [24], as described below in the Figure 1.5.

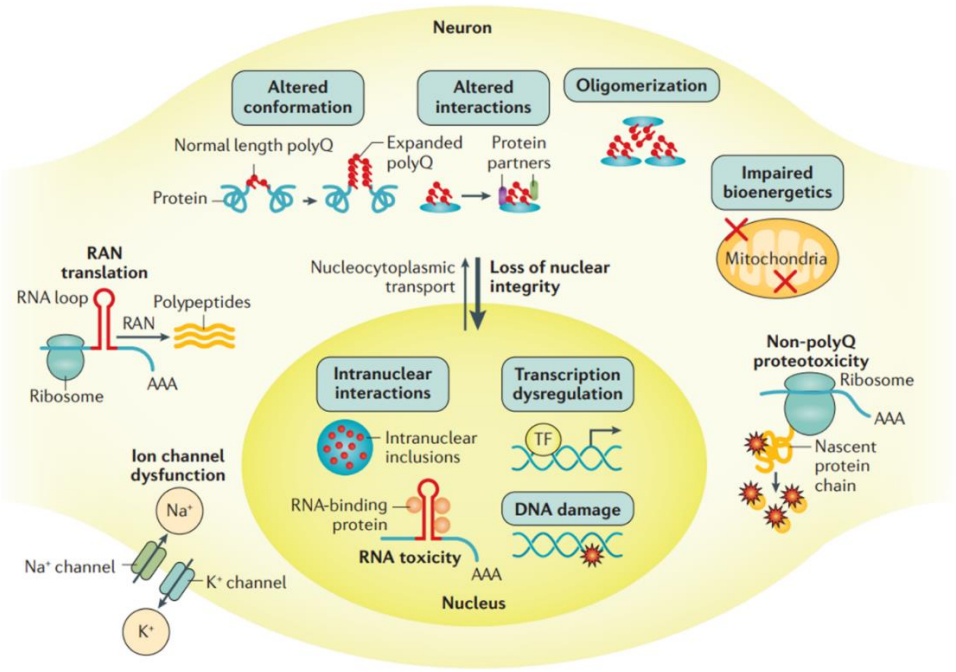

Figure 1.5 Pathogenic mechanisms shared by cerebellar ataxias. A detailed description of the pathways illustrated can be found in the text. Adapted from Klockgether, T. et al. (2019)[8].

1.1.5.1 Abnormal Protein Folding and Aggregation

The expansions of coding repeats (e.g., SCA1, 2, 3, 6, 7, 17 and DRPLA) were hypothesised to adopt conformations prone to aggregation or generate protein fragments, triggering intracellular protein inclusions in affected brains and *in vitro* studies[8,11]. Importantly, the repeat length threshold for aggregation *in vitro* strongly relates with the repeat length known to cause disease[11]. Therefore, polyQ protein inclusions seems to be the main feature for the disease process, where initial oligomers and microaggre-

gates have a toxic effect and macroagregates may reflect a protective response towards neuronal survival by isolating abnormal accumulated proteins into relatively neutral complexes (e.g., large fibrillar structures)[8,11,24].

The misfolded polyQ protein places a continual burden on protein homeostasis pathways[8,11]. Simultaneously, these mutant protein oligomers or fragments may participate in aberrant protein-protein interactions, including its normal partners and novel interactors, or may be unable to achieve its complete range of functions; thus, compromising several cellular processes such as cargo trafficking in neurons[8,11]. Moreover, proteins caused by conventional mutations may also misfold, altering protein function and promoting aggregation[8]. Some have been implicated in protein fidelity reduction (e.g., in SCA26), unfolded protein response (UPR) induction (e.g., in SCA35), fibril formation (e.g., in SCA14), and altered cytoskeletal dynamics (e.g., in SCA5)[8].

1.1.5.2 Gene Transcription Dysregulation

The expansion repeats proteins or their proteolytic fragments can concentrate in the nucleus engaging in aberrant protein-protein or protein-DNA interactions, altering transcription factors and other nuclear proteins activity (e.g., in SCA3)[8]. Consequently, chromatin state and promoter's activity of genes crucial for neuronal development and function can be altered[8,11]. These pathological nuclear peptides also contribute to altered nucleocytoplasmic transport and loss of nuclear integrity. Moreover, several polyQ proteins directly affect transcription (e.g., in SCA7, SCA17, SCA1), being observed alterations in gene expression profiles in patients' brains[8,11].

Additionally, in some SCAs the dysregulation of neuronal calcium homeostasis may alter calcium-mediated pathways, such as the mitogen-activated protein kinase (MAPK) cascade which catalyses the phosphorylation of transcription factors and thereby regulating transcription and chromatin remodelling[24].

Regarding noncoding repeats causing cerebellar ataxias, the current hypothesis states that they act through an RNA dominant toxic mechanism by binding and sequestering RNA-binding proteins, perturbing splicing or other RNA-related processes[8,11]. Also, this non-coding expansions may accumulate in aggregates and negatively influence protein homeostasis[8,24].

1.1.5.3 Channelopathies

Several cerebellar ataxias are directly caused by mutations in genes encoding transmembrane channels or associated regulatory proteins that lead to channel dysfunction, possibly affecting tissues like the muscle and nervous system[8,24]. The mutation of genes such as the *CACNA1A* (causing SCA6, EA2 and familial hemiplegic migraine 1 (FHM1)) and glutamate metabotropic receptor 1 (*GMR1* causing SCA44) lead to alterations in the calcium channel physiological proprieties and an increase in the glutamate receptor activity, respectively[8,23]. Thus, these channel's dysfunction possibly leads to excitotoxicity in Purkinje cells causing cerebellar ataxia[24].

Therefore, channel modulators represent an appealing approach to ameliorate disease symptoms caused by neuronal dysfunction and neurodegeneration[8,24].

1.1.5.4 Mitochondrial Dysfunction

Several genes related to mitochondrial function have been related to cerebellar ataxias[23]. For example, in SCA28 and FRDA, mutations in the genes ATPase family gene 3-like 2 (*AFG3L2*) and *FXN* respectively, lead to alterations in oxidative phosphorylation, mitochondrial respiration, and iron homeostasis[8]. However, the role of reactive oxygen species (ROS) in the pathogenesis of cerebellar ataxias still needs further clarification.

Still, as cellular pathways from transcription to degradation pathways influence mitochondrial function, in most of the cases there is an indirect mitochondrial impairment like in Huntington's disease (HD)[8]. The mitochondrial dysfunction and ROS may affect cellular processes like proliferation and differentiation and provoke oxidative damage and apoptosis via the intrinsic mitochondrial pathway in neurodegenerative diseases[23,24]. However, little is known about the contribution of mitochondrial disfunction and impaired bioenergetics in cerebellar ataxias.

1.1.5.5 Defective DNA Repair

The neurons are submitted to high levels of oxidative stress, generating ROS that potentially cause DNA damage, and trigger cell death[25]. Several cerebellar ataxias are caused by defects in DNA repair, including the ARCAs: AT, and ataxia with ocular apraxia type 1, 2 and 4 (AOA1, AOA2 and AOA4), caused by mutations in the *ATM*, aprataxin (*APTX*), senataxin (*SETX*) and polynucleotide kinase 3'-phosphatase (*PNKP*) genes, respectively[5,8]. In addition, it was found a significant association between DNA repair pathways and the age of onset in SCAs[26].

Thus, the inability to repair DNA damage may cause neuronal degeneration. The increase in DNA damage have been linked to Alzheimer's disease (AD) and HD, and DNA repair factors like breast cancer 1 (BRCA1) have shown to be neuroprotective[26].

1.1.5.6 Protein Degradation Pathways: UPS and Autophagy

The main pathways responsible for protein homeostasis are autophagy and ubiquitin–proteasome system (UPS). UPS have been associated with several polyQ ataxias where the proteosome machinery dislocation near the aggregates and their consequent ubiquitination suggests an attempt to prevent proteotoxicity[27]. However, the proteosome complex might be sequestrated to the inclusions or blocked by the polyQ expansions, preventing the degradation of other proteins, causing UPS impairment[27]. Also, protein misfolding and ER stress is linked to UPR and ER-associated protein degradation (ERAD) as a way to restore protein homeostasis, although in irreversible cases apoptosis is induced[28]. Though, the role of these mechanisms in cerebellar ataxias is still not well understood.

Additionally, some studies demonstrated that decreased autophagy could cause ataxia in the absence of aberrant proteins[24]. Therefore, in the context of polyQ cerebellar ataxias when UPS is impaired, misfolded proteins tend to aggregate and saturate the autophagy pathway, consequently reducing the ability of the cell to deal with other cellular processes. Alterations in autophagy have been described in several NDDs including AD, HD, Parkinson's disease (PD), and Frontotemporal lobar dementia (FTLD-TDP). In SCAs caused by conventional mutations, the mutant proteins were also found to be targeted to autophagy. It also has already been shown that the pharmacological modulation of autophagy decrease toxicity and improve the phenotype in different disease models of AD and PD, so if autophagy impairment will be defined as a common feature in ataxias, therapies to increase autophagy may help ataxias in a general manner[24].

1.2 Spinocerebellar Ataxia Type 11

The spinocerebellar ataxia type 11 (SCA11) is a slowly progressive cerebellar ataxia, characterised by limb and gait imbalance, dysarthria, dysphagia, nystagmus, and hyperreflexia[29,30]. In some cases, pyramidal features, peripheral neuropathy, and dystonia were observed in patients[29,31,32]. Onset of SCA11 varies from early to late adulthood, with an average of 30 years[29,31–33]. The life span is thought to be normal, but most patients require a wheelchair decades after onset[31,33]. SCA11 prevalence is unknown, however it accounts for less than 1% of autosomal dominant ataxias in Europe[33].

SCA11 was first described in a large British family as a slowly pure progressive cerebellar ataxia, genetically linked to the locus 15q14–21[29,30]. After screening, the candidate gene tau tubulin kinase 2 *(TTBK2)* was analysed, leading to the identification of a one-base insertion (c.1329_1330insA, p. Arg444Thrfs*7) in patients[29]. In the same study, a deletion of a dinucleotide in another family of Pakistani ancestry (c.1284_1285delAG, p. Glu429Aspfs*21) was identified[29]. Afterwards, more 3 families with TTBK2 truncating variants have been reported, one from France and other from Germany (c.1306_1307delGA, p. Asp435Tyrfs*14), and one from Denmark (c.1205_1207delinsA, p. Thr402fs*48)[31,33]. Interestingly, in a 2013 next-generation sequencing pilot study, a patient with cerebellar atrophy had the same variant as the one found in the British family (c.1329_1330insA), suggesting a possible link between them[34]. More recently, two missense variants in *TTBK2* were identified and linked to cerebellar ataxia, but no functional studies were performed to clearly associate the variants to the disease[32,35]. A detailed description of the SCA11 cases along with the identified TTBK2 variants can be found in Table 1.1.

Table 1.1 Description of the SCA11 cases along with the identified *TTBK2* variants.

Origin	TTBK2 variant	Age of onset	Main findings	Symptoms	Walking aid	References
England	c.1329InsA; p.Arg444Thrfs*7	16-35 years old	Cerebellar atrophy	Imbalance; dizziness; diplopia; staggering; dysarthria; cerebellar ataxia; gait and limb ataxia; nystagmus; hyperreflexia	Wheelchair	29, 30
Pakistan	c.1284_1285DelAG; p.Glu429Aspfs*21	11-60s years old	Cerebellar atrophy	Imbalance; staggering; clumsiness; dysarthria; gait and limb ataxia; nystagmus; hyperreflexia	Wheelchair	
France	c.1306_1307delGA; p.Asp435Tyrfs*14	35-58 years old	Cerebellar atrophy	Cerebellar ataxia; dysarthria	Wheelchair	33
Germany		40-50 years old	Pancerebellar atrophy	Imbalance; gait ataxia; dysarthria; nystagmus	Wheelchair	
Denmark	c.1205_1207delinsA; p.Thr402fs*48	4 year old-adolescence	Cerebellar atrophy and reduced metabolic activity in the cerebellum	Imbalance; gait ataxia; clumsiness; diplopia; dysarthria; nystagmus; ophthalmoplegia; hyperreflexia	Wheelchair	31
China	c.3290T>C; p.Val1097Ala	38-44 years old	Cerebellar atrophy, mild atrophy of the medulla ablongata and neurogenic damage	Dysarthria; gait and limb ataxia; nystagmus; dysphagia; muscle atrophy; limb weakness	-	32
No data	c. 239T>A; p. Phe80Tyr	≥40 years old	No data	No data	No data	35

These variants are all heterozygous frameshift mutations, except for the ones found in the Chinese and in the Italian reports, leading to the generation of a premature stop codon and ultimately to protein truncation of the non-catalytic C-terminal moiety[36] .

The SCA11 patients (c.1329_1330insA, p. Arg444fs*7) presented mRNA levels reduced by 50%, when compared to unaffected individuals, suggesting that the premature stop codon leads to nonsense-mediated decay (NMD) of the mutated mRNA and cause haploinsufficiency of the TTBK2 protein[29]. When affected individuals lymphoblasts' were treated with cycloheximide, a known inhibitor of NMD, the total *TTBK2* mRNA increased, showing that a proportion of the abnormal mRNA escapes NMD. Thus, the truncated protein could still be produced and cause a dominant-negative effect on the normal allele[29].

Interestingly, homozygous mutant TTBK2 mice for the truncating variant c.1329_1330insA were embryonic lethal at embryonic day 10, showing development delay, indistinct brain subdivisions and distorted caudal bodies[36]. While heterozygous mutant TTBK2 mice were completely normal and exhibited a regular lifespan[36].

Post-mortem neuropathological examination of the brain of one affected individual of the British family (c.1329_1330insA, p. Arg444fs*7) revealed gross atrophy of the cerebellum accompanied by severe loss of Purkinje and granule cells, and a marked preservation of the basket cells, as well as neuronal loss in the dentate nucleus and proliferation of Bergmann glial cells[29]. There were also alterations related with pathological aging, such as tangles and β-amyloid-positive plaques observed in the neocortex, hippocampus, transentorhinal, entorhinal and insular cortex[29]. The cerebellum degeneration was also accompanied by tau deposition, like what happens to aberrantly phosphorylated tau in taupathies such as AD[29,37]. Therefore, the dominant basis of disease may reflect aberrant action of TTBK2 on tau. *In* vivo brain MRIs showed predominantly vermal atrophy of the cerebellum, along with a moderate atrophy of the pons and medulla[38]. Occasionally, atrophy has also been described in the medulla, but this was not associated with disease severity[32,38]. In a Danish proband, a PET scan showed reduced metabolic activity in the cerebellum and pons, and brain MRI four years later showed worsening of cerebellar atrophy with olivopontine atrophy[31].

1.2.1 Tau Tubulin Kinase-2

The *TTBK2* gene located at chromosome 15q15.2 can encode multiple alternatively spliced mRNAs that translate into a protein up to 1244 amino acids in length, with ubiquitous expression in human adult and fetal tissues[29,30] (Figure 1.6A and B). *TTBK2* mRNA is expressed in all brain regions, with a particularly higher expression in the Purkinje and granular cell layers of the cerebellum, the hippocampal CA1 sector, midbrain, and substantia nigra. Contrarily, a lower expression was seen in the brain cortex[29]. At the protein level, TTBK2 is highly expressed in brain and testis, which corresponds to the elevated kinase activity of this protein in these tissues[36].

TTBK2, as a serine-threonine protein kinase, belongs to the casein kinase (CK1) group of eukaryotic protein kinases, composed of CK1 isoforms (α1, α2, δ, ε, γ1, γ2 and γ3), vaccinia-related kinase (VRK)

isoforms (1, 2 and 3) and TTBK isoforms (1 and 2)[39]. TTBK2 possesses 38% identity with CK1δ within the kinase domain, but there is no obvious homology beyond the catalytic moiety[40]. Moreover, TTBK1 (35–294) and TTBK2 (21–280) have highly homologous kinase domains (88% identity and 96% similarity)[39] (Figure 1.6B). Despite of the lack of homology in the rest of the sequences, there is a small C-terminal domain (TTBK1 1053–1117; TTBK2 942–1006) with 43% identity and 58% similarity[36,39] (Figure 1.6B), corresponding to the SxIP (serine any amino acid isoleucine proline) motifs location[41]. Although TTBK1 and TTBK2 are distinctly conserved among vertebrates, only the catalytic domain is preserved in invertebrates (such as *C. elegans* and *D. melanogaster*, suggesting that TTBK1 and TTBK2 genes diversified from a common shorter TTBK gene during the evolution from invertebrates to vertebrates[39].

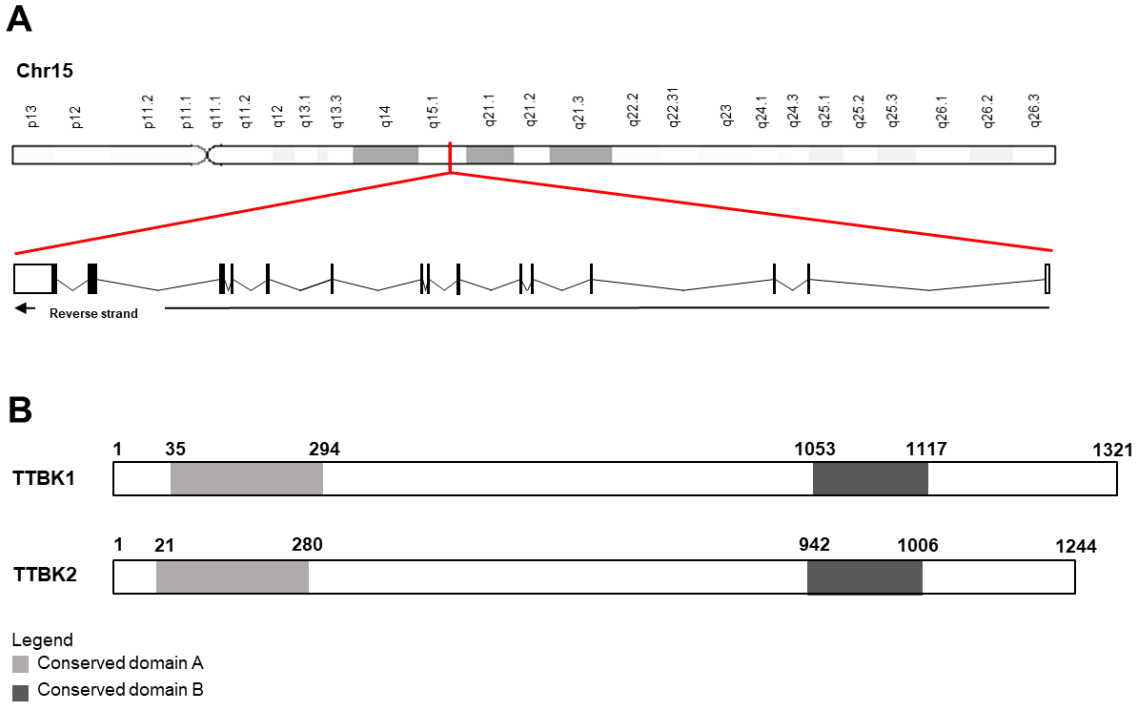

Figure 1.6 *TTBK2* genomic location and protein characterization. (A) *TTBK2* gene located at chromosome 15q15.2, with 14 coding exons. (B) TTBK1 (35–294) and TTBK2 (21–280) have highly homologous kinase domains (Conserved domain A, 88% identity and 96% similarity) and a small C-terminal domain (TTBK1 1053–1117; TTBK2 942–1006) with some grade of conservation (Conserved domain B, 43% identity and 58% similarity), indicating the existence of a functional motif.

TTBK2 was first identified based on its ability to phosphorylate microtubule-associated proteins tau and β-tubulin *in vitro*[42–44]. Since then, several cellular functions have been attributed to TTBK2, but few have been described in detail, including:(1) initiation of ciliogenesis, possibly by modulating sonic hedgehog (SHh) signalling[45–47]; (2) microtubule plus-end tracking protein (+TIP), regulating the microtubule-depolymerizing activity of kinesin family member 2A (KIF2A)[41,48]; (3) regulation of membrane transporters like the betain/GABA transporter 1 (BGT1)[49], the sodium-coupled glucose transporter (SGLT1)[50] and the glutamate (kainate) receptor subunit 2 (GluK2)[51]; (4) phosphorylation of the transactive response DNA-binding protein 43 kDa (TARDBP or TDP-43)[52], a nucleotide binding protein linked to several neurodegenerative diseases[53]; and (5) role in sensitivity of tumour cells against antiangiogenic

treatment[54]. Furthermore, TTBK2 may also play a role in mitosis[55,56], interact with the inositol/IP3 pathway, and stabilize Purkinje cells to resist calcium-induced cell death[57]. A summarised description of TTBK2 involvement with some cellular processes or structures can be found in Table 1.2.

Table 1.2 TTBK2 involvement in several cellular processes have been identified.

Cellular processes	Targets	References
Cytoskeleton	tau, β-tubulin, KIF2A	42-44, 48
Transcription	TDP-43	52
Ciliogenesis	CEP164, CEP97, MPP9, CEP83, CEP89, CCDC92, Rabin8, and DVL2/3	46, 62-66
Mitosis	Midbody and mitotic spindle	55, 56
Transporters and receptors	SGLT1, BGT1, GluK2, SV2A	49-51, 59

1.2.1.1 TTBK2 phosphorylation of tau, TDP-43 and SV2A

One of the main targets of TTBK2 is the cytoskeletal tau protein[42–44], which abnormal phosphorylation is associated with neurodegeneration in AD[37]. The abnormal deposition of tau in SCA11 patients together with the knockdown experiences of the TTBK2 *C. elegans* homolog in FTDP-17 (frontotemporal dementia and parkinsonism linked to chromosome 17) suggest an indirect interaction between TTBK2 and tau that prevents tau toxicity[29,43]. Also, the two TTBK2 phosphorylation sites in tau (Ser208 and Ser210) are known priming sites for the phosphorylation of tau by glycogen synthase kinase 3 (GSK-3β), supporting the existence of a common pathway that involves TTBK2, GSK-3β and tau[43,58].

TTBK2 has also been found to phosphorylate TDP-43 at Ser409/410 *in vitro* and in cellular and animal models of amyotrophic lateral sclerosis (ALS)[52]. TDP-43 is a DNA/RNA binding protein that undergoes several modifications including ubiquitination, phosphorylation, and proteolytic processing, possibly promoting aggregation[53]. TDP-43 hyperphosphorylated inclusions are hallmarks of ALS and FTLD-TDP and may also be present in some other neurodegenerative diseases, such as AD, PD and HD[53]. Still, the neurodegeneration may to be related to an alteration in TDP-43 function rather than toxic inclusions[53].

In FTLD-TDP and ALS it was observed an increase of TTBK1/2 levels, and a cytoplasmatic co-localization of TTBK1/2 with phosphorylated TDP-43 aggregates[52]. TTBK2 overexpression resulted in phosphorylation and re-localization of TDP-43 from the nucleus to the cytosol, like the neuronal cytoplasmic inclusion pathology observed in FTLD-TDP and ALS[52]. Thus, TTBK1/2 phosphorylation at Ser409/410 may have a central role in TDP-43 loss-of-function and neurotoxicity by impairing its autoregulation mechanism and increasing TDP-43 expression[53]. Moreover, decreased phosphorylation of TDP-43 may ameliorate the motor defects resulting from pathological TDP-43[52].

Therefore, tau and TDP-43 proteinopathies appear to share a common aetiology, caused by impaired TTBK2 activation leading to neuropathology.

Furthermore, TTBK2 phosphorylates the synaptic vesicle protein 2A (SV2A) in the cytoplasmic N-terminal domain (Thr84), which promotes its interaction with synaptotagmin-1[59]. This interaction is important for synaptic vesicle trafficking and regulation of neurotransmitter release[59].

1.2.1.2 TTBK2 and Microtubule's Dynamics

Microtubules are dynamic structures composed of α/β tubulin heterodimers tightly controlled to ensure the normal function and division of eukaryotic cells. Besides the phosphorylation of β-tubulin and tau[42,43], TTBK2 also act as a +TIP by tracking growing microtubule ends and binding to the end binding protein 1 (EB1), connecting both to several proteins and cellular structures in a kinase-independent manner (SxIP motifs)[41]. The binding of TTBK2 to EBs enables the phosphorylation of KIF2A at Ser135 *in vitro*, inhibiting its interaction with the microtubules and decreasing the depolymerizing activity[48]. Contrarily, in the absence of TTBK2, KIF2A exhibit an extensive localization to the microtubules, which induces short-lived microtubules with an increased shrink rate and a decreased rescue frequency[48]. Moreover, overexpression of TTBK2 displaced EB1 from the microtubules, suggesting that it may regulate the association of +TIPs and other microtubule-associated proteins with newly polymerized ends[41,48]. Therefore, the EB–TTBK2 interaction appears to antagonize the microtubule-depolymerizing machinery, primarily affecting KIF2A[48].

Furthermore, a study suggested that the centrosomal protein of 164 kDa (CEP164) may play a role in recruiting TTBK2 to the midbody during cytokinesis[56]. However, the TTBK2 role at the midbody remains elusive. Additionally, the TTBK homolog in *D. melanogaster* (Asator) appeared to be localized at the mitotic spindle interacting with the spindle matrix protein Megator, homolog of the human nucleoprotein translocated promotor region, that functions as a spatial regulator of the spindle assembly checkpoint, ensuring a correct spindle maturation[55].

1.2.1.3 TTBK2 in Ciliogenesis

Ciliogenesis is perhaps the most well studied function of TTBK2. Ciliogenesis is closely regulated according to the phase of the cell cycle, as well as other cellular activities, and require a delicate control of axonemal cytoskeleton remodelling[60]. On quiescent cells, the primary cilium (PC) extends its axoneme from its basal body after the transportation of tubulin precursors by intraflagellar transport (IFT) proteins and molecular motors that are added to the ciliary tip until it reaches its stable length. Before re-entering the cell cycle, the cilium is resorbed after disassembly of the axonemal microtubules subunits and shortening of the cilium, for preparing for centriole duplication[60]. These processes regulate signalling pathways such as SHh and Wnt signalling's that are essential to embryonic patterning, organogenesis, and cellular homeostasis[47]. Mutations in ciliary proteins result in early embryonic lethality or in the development of ciliopathies such as the Joubert syndrome and the Bardet-Biedl syndrome[61].

Several proteins associated with cilia, namely CEP164[62,63], CEP97[63], M-Phase Phosphoprotein 9 (MPP9)[64], CEP83[65,66], CEP89, coiled-coil domain containing 92 (CCDC92), Rabin8, and dishevelled 2/3 (DVL2/3)[66] are subjected to TTBK2 phosphorylation in their intrinsically disordered regions (IDRs)[66]. Given that phosphorylation of IDRs might affect protein structure, it was speculated that TTBK2 phosphorylation leads the cilia proteins to achieve a novel conformation that ensures their timely interactions and formation of complexes necessary for the PC assembly[66–68].

Moreover, TTBK2 controls the cilia assembly pathway by turning the cilia initiation to cilia elongation process[46]. First, the cell cycle regulators target CEP164 to induce PC formation by recruiting TTBK2 to the basal body distal appendages (DA)[62,63,69]. Then, at the basal body DA, TTBK2 promotes the removal of CP110, probably through the phosphorylation of CEP97 and MPP9, which leads to the displacement of the CP110/CEP97/CEP290/KIF24 cilia suppression complex from the distal end of the microtubules (mother centriole), allowing the beginning of ciliary axoneme elongation[46,70]. Furthermore, TTBK2 seems to promote the recruitment or retention of IFT proteins at the base of the cilium, to construct the ciliary axoneme[46]. Then, through an unknowing mechanism, TTBK2 is removed from the basal body for cilia disassembly[46].

Recent studies suggested that SCA11-associated variants cause defects in ciliogenesis[46,71]. It was reported that SCA11 cells have a failure in axoneme elongation, since truncated TTBK2 is unable to interact with CEP164 and fail to localize to DA[46,62]. Thereby, it cannot displace the cilia suppression complex or recruit IFTs for the cilia assembly, which causes loss of SHh activity[46]. Also, it was proposed that these effects are due to a dominant negative mechanism that disturbs wild-type TTBK2[46]. As apart from TTBK2, only the Microtubule Associated Protein (MAP)/microtubule affinity-regulating kinase 4 (MARK4) has been implicated in cilium initiation and assembly, suggesting that no other kinase can compensate for defects caused by SCA11-associated mutations[57,71].

The finding that TTBK2 is essential for ciliogenesis along with the phenotype present in SCA11 animal models and the loss of Purkinje cells raises the possibility that cilia are important to promote cerebellar development and prevent neural degeneration[46,57,71].

1.2.1.4 TTBK2 Interaction with Transporters and Receptors

TTBK2 seems to up-regulate SGLT1[50] and BGT1[49], by increasing their protein abundance in the cell membrane. However, this effect of TTBK2 depends on the kinase activity as it is disrupted by SCA11 truncating mutations[49,50]. Contrarily, TTBK2 down-regulates the GluK2 activity by decreasing the channel protein abundance in the cell membrane and neuroexcitation that would cause neurodegeneration[51]. Also, it was reported that the SCA11-associated protein accumulates perinuclearly, which is consistent with reduced effects on plasma membrane GluK2[36,51].

Thus, TTBK2 could be modulating the protein abundance in the cellular membrane by participating in the regulation of transport processes, through the modification of the microtubules[36]. However, additional studies are needed to elucidate the mechanisms behind TTBK2 activity and transporters abundance, and whether it influences excitatory neurotransmission and consequently neuronal function and survival[36].

1.3 Aims of the Study

SCA11 is a rare autosomal dominant cerebellar ataxia, so far linked to four frameshift and two missense heterozygous variants in *TTBK2*[29,31–33,35]. The heterozygous truncating variants were reported to reduce TTBK2 mRNA and proteins levels in patients[29], provoke a nuclear dislocation[36], as well as impair TTBK2 kinase activity[46,51,52]. From a previous genetic study, we identified a novel heterozygous missense variant in TTBK2 (c.625C>T; p.Leu209Phe) in two siblings presenting progressive cerebellar ataxia, nystagmus, and dysarthria. So, the main purpose of this project was to confirm and characterize the pathological potential of the new TTBK2.

Therefore, the following objectives were proposed:

(1) Create and validate a cellular model expressing the novel TTBK2 missense variant using Clustered Regularly Interspaced Short Palindromic Repeats (CRISPR)/Cas9 technology.

(2) Evaluate TTBK2 gene and protein expression by RT-qPCR and immunoblotting, respectively, and the subcellular localization of TTBK2 by fluorescence microscopy and subcellular fractionation assays.

(3) Characterise the impact of the novel variant in TTBK2 molecular functions such as microtubule dynamics and TDP-43 phosphorylation, as well as investigate autophagy impairment, a mechanism associated with neurodegeneration recurring to immunoblotting and immunofluorescence protocols.

(4) Analyse the phosphoproteome of the mutated cell line by mass spectrometry to look for changes in cellular kinases activity.

2

MATERIALS AND METHODS

2.1 *In Silico* Analysis

The pathogenicity of the missense variant was evaluated across four criteria: (a) functional *in silico* prediction of the variant pathogenicity recurring to the Variant Effect Predictor (VEP) tool (https://www.ensembl.org/Tools/VEP)[72]: MutationTaster[73], Mutation Assessor[74], MutPred[75,76], FATHMM[77], FATHMM-MKL[78], FATHMM-XF[79], LRT[80], Deogen2[81], Eigen/Eigen PC[82], SIFT[83], Provean[84,85], MVP[86], Revel[87], Primate AI[88], MetaSVM/MetaLR[89], M-CAP[90], PolyPhen[91], LoFtool[92], Condel[93], BayesDel (addAF and noAF)[94], ClinPred[95], LIST-S2[96], VEST[97,98], DANN[99] and CADD[100,101]; (b) minor allele frequency <1% in gnomAD (https://gnomad.broadinstitute.org/)[102], 1000 Genomes Project (https://www.internationalgenome.org/)[103], and dbSNP (https://www.ncbi.nlm.nih.gov/snp/)[104] databases; (c) conservation analysis prediction by PhyloP[105], PhastCons[106], Integrated fitCons[107] and GERP++[108], also obtained from the VEP tool; (d) prediction of protein stability changes was performed with DynaMut (http://biosig.unimelb.edu.au/dynamut/) and DynaMut2 (http://biosig.unimelb.edu.au/dynamut2/) web servers, obtaining six different predictions of changes in folding free energy (ΔΔG): DynaMut2[109], DynaMut[110], ENCoM[111,112], mCSM[113], SDM[114], and DUET[115], recurring to the partial or complete 3D structure available in the Protein Data Bank (PDB) (https://www.rcsb.org/)[116,117]. The DynaMut2 web server was also used to generate images of the interatomic interactions.

2.2 Expression Vectors

The pEGFP-C1-TTBK2-WT plasmid (MRC PPU, University of Dundee) was modified by site-directed mutagenesis using the QuikChange II Kit (Agilent) to produce the TTBK2 kinase dead (KD) Asp163Ala variant and the new Leu209Phe variant plasmids. The following primers pairs were used to introduce Asp163Ala and Leu209Phe variants: forward primer 5′-GGAAATGTTACATGCTTGCTTTTGGCTTGGCTCGACA-3′ and reverse primer 5′- TGTCGAGCCAAGCCAAAAGCAAGCATGTAACATTTCC-3′; and forward primer 5′-GAAATGGGAAGACATGATGACTTTTGGTCCTTATTCTACATGT-3′ and reverse primer 5′-ACATGTAGAATAAGGACCAAAAGTCATCATGTCTTCCCATTTC-3′, respectively.

2.3 Cell Culture and Transfection

Human embryonic kidney 293 cells incorporated with SV40 large T antigen (HEK293T) cells were grown in Dulbecco's Modified Eagle Medium (DMEM) high glucose GlutaMAX™ supplemented with 10% fetal bovine serum (FBS) and 1% antibiotic-antimycotic (Gibco, Life technologies) at 37 °C in a humidifed 5% CO_2 atmosphere. Cells were transiently transfected for 24h with each plasmid using Lipofectamine™ 2000 (Invitrogen) according to the manufacturer's protocol. For autophagy analysis, cells were incubated with the autophagy inhibitor chloroquine (25 μM for 2h for immunofluorescence assays; 10 μM for 18h for immunoblotting experiments; Sigma-Aldrich)[118], or control vehicle DMEM (Gibco, Life technologies).

2.4 CRISPR-Cas9 System

The knock-in of the *TTBK2* c.625C>T (p.Leu209Phe) variant (Figure 2.1) was performed on HEK293T cell line genetically modified using CRISPR/Cas9 system to insert an N-terminal 3xFLAG-tag in *TTBK2* (FLAG-TTBK2-WT), according to methods already described[119,120]. A single-chain guide RNA (sgRNA) in the variant flanking zone was designed using the CRISPOR online tool (http://crispor.tefor.net/): 5'-ACATGTAGAATAAGGACCAA-3', considering that it should be as close as possible to the modification site and preferentially near a protospacer adjacent motif (PAM) sequence (NGG) for a more successful edition[119]. A single-stranded oligodeoxynucleotide (ssODN) with 50 bp homology arms (5´- tgtgactggattctgttttgtttatgaagGAAATGGGAAGACATGATGACTTTTGGTCATTATT CTACATGTTGGTGGAGTTTGTGGTTGGTCAGCTGCCCTGGAGAAA-3´) was designed to serve as a template for homology-directed repair (HDR)[119]. A silent point mutation within the PAM sequence was also introduced in the ssODN to easily select/genotype the cells through the AvaII restriction site (would be destroyed in case of HDR). After annealing, single-stranded oligos containing the sgRNA sequence (forward 5′- CACCGTTGGTCCTTATTCTACATGT-3′ and reverse primer 5′- AAACACATGTAGAA-TAAGGACCAAC-3′) were cloned through BbsI restriction sites into the mammalian expression construct pSpCas9(BB)V2.0 (Addgene), bearing both sgRNA scaffold backbone and *S. pyogenes* Cas9 (pSpCas9(BB)V2.0).

The Cas9/sgRNA (2 μg) plasmid was co-transfected along with the ssODN (10 μM) and an inhibitor of an enzyme involved in non-homologous end joining (NHEJ) repair - NU7026[121,122] (10 μM, Sigma-Aldrich) for 24h using DreamFect Gold reagent (OZ Biosciences, 1:2.5 ratio) according to the manufacturer's protocol. Following transfection, clonal cell lines were sorted through fluorescence-activated cell sorting (FACS) and further genotyped through PCR amplifications (forward 5′-ACACATTAACTAATGGGCTGTT-3′ and reverse primer 5′-TCTTCTACCACAATTGACATCT-3′), using Ranger Mix (Bioline), followed by digestion with AvaII (New England Biolabs) at 37ºC for 4 hours with an inactivation step at 80ºC for 20 min. In addition, the purified PCR products with Exo/SAP (GRiSP) were further analysed by Sanger sequencing using BigDye Terminator Cycle Sequencing v1.1 (Applied

Biosystems) and an ABI 3130xl Genetic Analyzer (Applied Biosystems). Sequencing analysis was carried out using the BioEdit Sequence Alignment Editor V7.0.5.3 software[123].

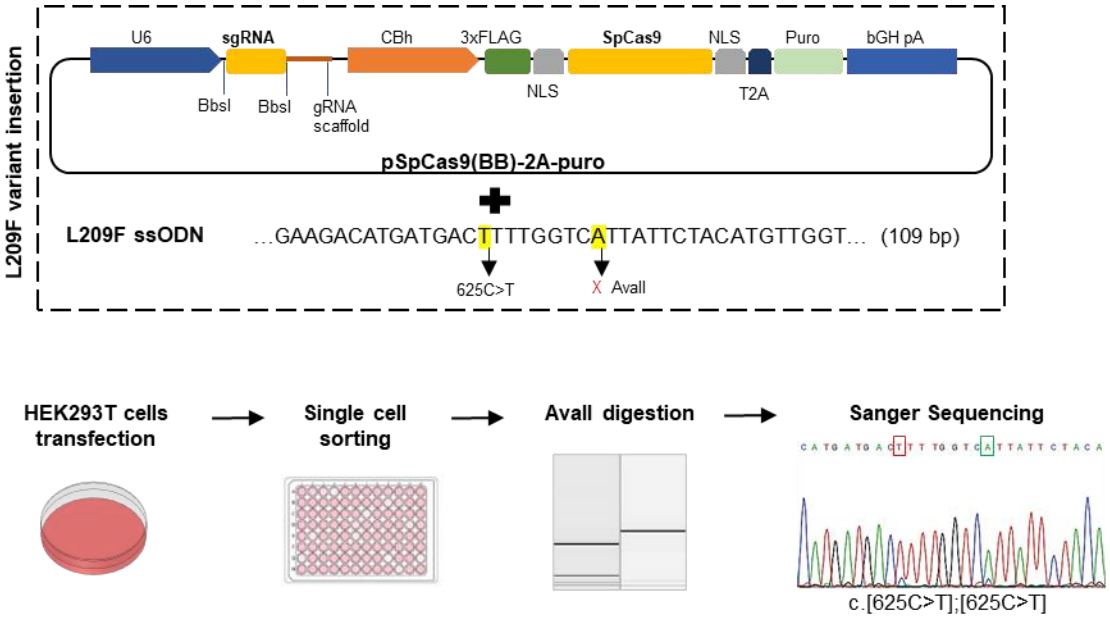

Figure 2.1 CRISPR/Cas9 system workflow. The sgRNA was cloned into the mammalian expression construct pSpCas9(BB)-2A-puro, and co-transfected in HEK293T cells with a HDR template (ssODN). Then isolation of clonal cell lines and genotyping were performed.

Table 2.1 The primers used to check alterations in off-targets sequences.

Mismatches	Gene	Off-target Sequence	PCR Primers
4	*SLC7A2*	TCAAGATGAATAAGGACCAAGGG	ACTGTTTGCTGGGAGCATTA TAATCAGGTGTAGGCCAGAGA
	CLYBL	ACATGCTGAATAGGGAACAATGG	CAGGACTCCCTCAGTCATAAAC CTTAAGGAACAGTCGTCCAGAG
	TTBK1	GCATGTAGAAGAGGGACCACAGG	GGAAGCACACACGGTAGTT CATCCGGTGCTCATACTTCTC
	TMEM181	GCATGTAGAATATGTACCATAGG	TTCAACTTGTCTTCCCTGGTAT CTGGTCATCTTCCAGGTTCTC
3	*TAFA1*	ATATGTAGAATAACAACCAATGG	AACCAGCAGTCTTTGGTGAA TGAATCCAACTGTGCCTGAA
	PIBF1	AAATGTAGCATAAGGACAAATGG	TCCTTCAGAGCAAACCATCAG CCAACAGTGAGGAACTGATGAT
	NEBL	ACATGTACAATAAGGAAAAATGG	TACCAGTTCCCTGAGGCATT AACTAGCGCAGTCTAATTGTGTA
	STAT5B	ACATGAAGAATAAGGGCCCAGGG	GACCAAGGAGAACCTCGTG ACATCTGCTTTGCTCTATTTCC
	DEPDC5	GCAGGTAGAATCAGGACCAATGA	GCTTACAAGGGTAGAACAGTAGG ATTCAGAGGGTCCAGAAATCAC
	TCF4	ACCTTTTGAATAAGGACCAAAGA	GGTTCAGGCTTTCAGAGCTAAT CATATCACACGAGGGCAGAAT
2	*KALRN*	ACATATAGAATAAGGACCAGAAG	TGACATGAGGAAGAGCTTGTG GTGGAGGCTCTGGATGTATAAG

The off-targets were predicted with the CRISPOR and CRISPR Finder (https://wge.stem-cell.sanger.ac.uk/) tools and checked for alterations using Sanger sequencing (as described above) in

the selected clonal cell line (FLAG-TTBK2-L209F). Off-targets with four or less mismatches were selected for sequencing[119,124] (Table 2.1): off-targets with four mismatches that fell within exons or splice sites (4 in total).; off-targets with three mismatches that fell within introns (6 in total; none was located in exons/splice sites); off-targets with two mismatches that fell within introns (1 in total); none was located in exons/splice sites); none off-target with less than two mismatches was predicted. Also, the other *TTBK2* exons (2-15) and intron 8-9 were checked for off-target effects (Table 2.2) (as described above). The detailed information of PCR and sequencing reactions can be found in Annex I.

Table 2.2 The primers used to check alterations in *TTBK2* gene.

Gene	PCR Primers
TTBK2_Ex2	TATTAGTAGTGCTTCCTGATGCTG AGGGTATAAACAGAGCTTAATCATAG
TTBK2_Ex3	AAGAGATCAATTGCTTTCAAGTTAG GAATGTAATTAAGGTTCAGGAAGATAC
TTBK2_Ex4	CTGGGAGGAGAAGAGGTAGGTAG CTGTTTAAATACAGTTCCATCTGC
TTBK2_Ex5	AATGGTAAGTGAGTAGTTTCCCAG CCACAGCAAATACACAAAGC
TTBK2_Ex6	TGGAACATGTGTGTTATATAGAG TCATTAAATGTATATGCCACTTC
TTBK2_Ex7	TTTCTTCCATTTACTTCATGGTTC GCAAGACTCTGTCTCAACAAATATAC
TTBK2_Ex8	GCTTGCTTCCCTTATTTCTACC AAGCTAAGAGGGAGGGCTATAA
TTBK2_In8_9	GCTTGCTTCCCTTATTTCTACC TGCTGAATTCTGGAGGGAGA
TTBK2_Ex9	GAGCTCAGTTCTTGCTTTATGC TGAAGTTAAGTCCATCCAGAGG
TTBK2_Ex10	GCAATTTGAGCCATCAGTTT TCTGAGGGAATCTGGATGAA
TTBK2_Ex11	AACCTCCGCCTTCTAGATTC CCCTCATGAATGAGAGTGGT
TTBK2_Ex12	TTTGAAAGGCTTCAATGATTC GGAGCTGAATAGACTCAGTGTTAC
TTBK2_Ex13.1	GAACTGAGCTCCATCTTCCA TGAAGCAGCAGTAGGAGGAC
TTBK2_Ex13.2	TAGGTCCTTGGGCAGAAAAT CAGTGGCCATCAATGTTAGA
TTBK2_Ex14.1	TGTGTTCTTCCTATAAATTAGAATTGG GTCTTGATTTGGCACCACAC
TTBK2_Ex14.2	TTAAGTAGAGGGCAGCATTG TTTTGCAGAAACTGGAGAGG
TTBK2_Ex14.3	GGATATGGTTAGGTCATCCTTTG TGGTGGACTACAATAAAGCAG
TTBK2_Ex15	AATTTGTCCAGGGTCATACAAC TTTACATAGAAAGTACAGGGACACAC

2.5 Reverse-Transcription Quantitative Polymerase Chain Reaction (RT-qPCR)

Total RNA was isolated from HEK293T, FLAG-TTBK2-WT and -L209F cells, using NZY Total RNA Isolation kit (Nzytech) as per the manufacturer's recommendations. RNA quantification was performed on NanoDrop 2000 Spectrophotometer (ThermoFisher Scientific). cDNA was synthesized by reverse transcription-PCR of 3 µg total RNA with oligo(dT), using the NZY First-Strand cDNA Synthesis Kit (Nzytech), according to the manufacturer's protocol. RT-qPCR was performed using PowerUp™ SYBR™ Green Master Mix (Applied Biosystems) and primers against *TTBK2* exon 4_5 and exon 8_9 (Table 2.3). Human *β-actin* was used as endogenous control. All reactions were performed in triplicate and replicated three times, using the Applied Biosystems 7500 Fast Real-Time PCR (Applied Biosystems). The analysis was carried out using 7500 Software v2.0.6 (Applied Biosystems), and mRNA expression was calculated by the $2^{-\Delta\Delta CT}$ method[125,126]. The detailed information of RT-qPCR reactions can be found in Annex I.

Table 2.3 The RT-qPCR primers used to analyse *β-actin* and *TTBK2* expression.

Gene	RT-qPCR Primers
TTBK2_Ex4_5	TGTAGATTTATTGGCTGTGG TGGTACTAATGGTGAATGTG
TTBK2_Ex8_9	TGGAGTTTGTGGTTGGTCAG TGAGCCTGTGGTCATATCTCT
ACTB	GCACTCTTCCAGCCTTCCTTC GTGATCTCCTTCTGCATCCTGTC

2.6 Subcellular Protein Fractionation

For subcellular protein fractionation, FLAG-TTBK2-WT and -L209F cells were washed, scrapped from the plate in ice-cold 1x phosphate buffered saline (PBS). The whole cell extract (corresponding to the total fraction) was centrifuged at 500 x*g* for 3 min and the supernatant discarded. Subcellular protein extraction was then performed, using the Subcellular Protein Fractionation Kit for cultured cells (Thermo Fisher Scientific), according to the manufacturer's instructions. Subcellular fractions corresponding to cytoplasm, membranes, soluble nuclear and chromatin-bound nuclear extracts were isolated. A fraction of the whole cell extract was collected and sonicated (Branson sonifier 250, ThermoFisher Scientific).

2.7 Immunoblotting

HEK293T, FLAG-TTBK2-WT and -L209F cells were collected in Radioimmunoprecipitation Assay (RIPA) buffer (Sigma; 150 mM NaCl, 1.0% IGEPAL® CA-630, 0.5% sodium deoxycholate, 0.1% SDS, 50 mM Tris, pH 8.0) supplemented with cOmplete Protease Inhibitor Cocktail (Roche) and then sonicated (Branson sonifier 250, ThermoFisher Scientific). Total protein concentration was measured with

the Pierce Bicinchoninic Acid (BCA) protein assay kit (ThermoFisher Scientific) according to manufacturer's instructions.

The samples (30–50 µg of total protein) were denatured in laemmli 1x loading buffer with β-mercaptoethanol at 95ºC for 10 minutes. After sample loading on a sodium dodecyl sulfate-polyacrylamide gel electrophoresis (SDS-PAGE) (Mini-PROTEAN, Bio-Rad), proteins were electrophoretically transferred onto polyvinylidene fluoride (PVDF) membranes (Merck-Milipore) using a wet (Mini Trans-Blot electrophoretic transfer cell, Bio-Rad) or a semi-dry (SemiPhor transfer unit, Hoefer) transfer systems depending on the proteins' molecular weight (MW). Membranes were stained with Ponceau S and images acquired with a ChemiDoc XRS+ Imaging System (Bio-Rad). After washing, membranes were blocked in 5% non-fat dry milk or bovine serum albumin (BSA) in Tris-buffered saline-Tween 20 (TBS-T) for 1 hour with agitation, at room temperature (RT), and subsequently incubated with specific primary antibodies as indicated (Table 2.4; diluted in 5% BSA in TBS-T and 1% sodium azide), overnight at 4°C with agitation.

Table 2.4 List of primary antibodies used in immunoblotting assays.

Antigen	Description	Manufacturer	Commercial reference	Dilution
EGFP	mouse monoclonal	Abnova	MAB1765	1:3000
FLAG	mouse monoclonal	Sigma-Aldrich	F1804	1:500
β-actin	mouse monoclonal	Sigma-Aldrich	A5441	1:50000
GM130	mouse monoclonal	BD Biosciences	610822	1:1500
Caspase 3	mouse monoclonal	Cell Signalling	9668	1:1500
HDAC2	mouse monoclonal	Santa Cruz	sc-9959	1:1000
Histone H3	rabbit polyclonal	Abcam	ab1791	1:10000
Vimentin	rabbit polyclonal	Proteintech	10366-1-AP	1:30000
KIF2A	rabbit polyclonal	Proteintech	13105-1-AP	1:2000
α-Tubulin	mouse monoclonal	Santa Cruz	sc-5286	1:10000
Acetylated α-tubulin	mouse monoclonal	Sigma	T7451	1:10000
TDP-43/TARDBP	rabbit polyclonal	Proteintech	10782-2-AP	1:30000
Phospho (S409/410) TDP-43	rabbit polyclonal	Proteintech	22309-1-AP	1:1000
p62/SQSTM1	mouse monoclonal	Proteintech	66184-1-Ig	1:1000
LC3B	rabbit polyclonal	Cell Signalling	2775	1:1000
LAMP1	rabbit monoclonal	Cell Signalling	3243	1:1000
ULK1	rabbit monoclonal	Cell Signalling	8054	1:1000
Phospho (Ser555) ULK1	rabbit monoclonal	Cell Signalling	5869	1:2000
Beclin1	rabbit monoclonal	Cell Signalling	3495	1:1000
Phospho (Ser93) Beclin1	rabbit monoclonal	Cell Signalling	14717	1:1000
Raptor	rabbit monoclonal	Cell Signalling	2280	1:1000
Phospho (Ser792) Raptor	rabbit polyclonal	Cell Signalling	2083	1:1000
CEP97	rabbit polyclonal	Proteintech	22050-1-AP	1:5000
CEP164	rabbit polyclonal	Sigma	SAB3500022	1:2000

The membranes were washed with TBS-T and then incubated with horseradish peroxidase (HRP)-conjugated secondary antibody (diluted in 3% non-fat dry milk or BSA in TBS-T) for 1 hour with agitation at RT (Table 2.5). Following three washes with TBS-T, detection was achieved using WesternBright Sirius or WesternBright Standard enhanced chemiluminescence (ECL)-HRP substrates (Advansta) and chemiluminescence detected with a ChemiDoc XRS+ Imaging System (Bio-Rad). Ponceau S staining and protein bands were quantified using the ImageLab 6.1 Software (Bio-Rad). Quantitative comparisons between samples of each experiment were always performed on the same blot. When necessary, membranes were stripped by incubation in stripping solution (62,5 mM Tris-HCl pH 6.7, 2% SDS, 100mM β-mercaptoethanol) at 50°C for 30min with gentle agitation.

Table 2.5 List of secondary antibodies used in immunoblotting assays.

Type of antibody	Description	Manufacturer	Commercial reference	Dilution
HRP-conjugated	Goat anti-mouse IgG	Santa Cruz	sc-2005	1:5000
HRP-conjugated	Goat anti-rabbit IgG	Merck-Millipore	401393	1:10000

2.8 Immunofluorescence

FLAG-TTBK2-WT and -L209F cells were fixed using 4% paraformaldehyde/4% sucrose (Merck-Millipore) for 20min, and permeabilised with 0.3% triton X-100 (Merck-Millipore) for 20min; or permeabilised/blocked in microscopy buffer (1% BSA, 0,1% saponin, and 0,02 % NaN3) for 1h. When necessary, cells were fixed and permeabilised in ice-cold methanol 100% (ThermoFisher Scientific) for 10 min. After washing with PBS, cells were blocked in 3% BSA/PBS for 45 min (except in case of permeabilisation in microscopy buffer) and further incubated with the primary antibodies for 3h at 4ºC (Table 2.6).

Table 2.6 List of primary antibodies used in immunofluorescence assays.

Antigen	Description	Manufacturer	Commercial reference	Dilution
FLAG	mouse monoclonal	Proteintech	66008-3-Ig	1:200
LC3A/B XP	rabbit monoclonal	Cell Signalling	12741	1:200
p62/SQSTM1	mouse monoclonal	Proteintech	66184-1-Ig	1:200
Acetylated α-tubulin	mouse monoclonal	Sigma	T7451	1:200
KIF2A	rabbit polyclonal	Proteintech	13105-1-AP	1:200

Then, cells were incubated with the secondary antibodies for 1 hour at RT (Table 2.7), washed with PBS and stained with Hoechst 33342 (1:10000, Life Technologies) for 5 min to label the nucleus. Preparations were mounted with ProLong™ Gold Antifade Mountant (Life Technologies) and visualized using an epifluorescence Zeiss Axio Imager Z1 microscope equipped with an Axiocam MR3.0 camera and Axiovision 4.7 sofware.

Table 2.7 List of secondary antibodies used in immunofluorescence assays.

Type of antibody	Description	Manufacturer	Commercial reference	Dilution

Alexa fluor 568 conjugated	Goat polyclonal anti-rabbit IgG	Thermo Fisher Scientific	A-11011	1:200
Alexa fluor 568 conjugated	Goat polyclonal anti-mouse IgG	Thermo Fisher Scientific	A-11004	1:200
Alexa fluor 488 conjugated	Goat polyclonal anti-rabbit IgG	Thermo Fisher Scientific	A-11008	1:200
Alexa fluor 488 conjugated	Goat polyclonal anti-mouse IgG	Thermo Fisher Scientific	A-11029	1:200

2.9 Phosphoproteome Analysis

2.9.1 Phosphoprotein Enrichment

Phosphoprotein enrichment was performed using the phosphate metal affinity chromatography (TALON® PMAC Phosphoprotein Enrichment Kit, Clontech) columns, which allows for the selective binding of proteins that contain a phosphate group on any amino acid (including serine, threonine or tyrosine), according to the manufacturer's instructions. Briefly, FLAG-TTBK2-WT and -L209F cells (in three replicates) were washed with PBS, scrapped in PBS supplemented with the phosphatase inhibitor NaF (10 mM) and protease inhibitors (cOmplete Protease Inhibitor Cocktail; Roche), centrifuged at 500 *xg* for 5 min and washed with PBS with NaF (10 mM) for two times, and the resulting pellet was frozen at −80°C. Extraction buffer was added to each sample according to pellet weight (30 µL buffer A/1mg of pellet), supplemented with the phosphatase inhibitor NaF (10 mM) and protease inhibitors. The samples were then incubated at 4°C for 10 min with mixing, followed by ultrasonic chromatin/DNA/RNA shearing (Bioruptor Plus, Diagenode) and centrifugation at 10000 *xg*, for 10 min at 4°C. In parallel, columns were washed with distilled water and twice with buffer A to equilibrate the columns. Protein concentration of supernatants obtained by centrifugation was determined by Pierce BCA protein assay to add about 7 mg of total phosphoproteins extracts to the columns and shaken at 4°C for 20 min for phosphoprotein binding. Then the non-adsorbed material (non-phosphorylated protein fraction) was allowed to flow through the column. After 4 washes, phosphorylated proteins were eluted (into 5 fractions) using 1ml of buffer B for 5 times, determining in the end their protein concentration by Pierce BCA protein assay. Samples were stored at −80°C before protein precipitation.

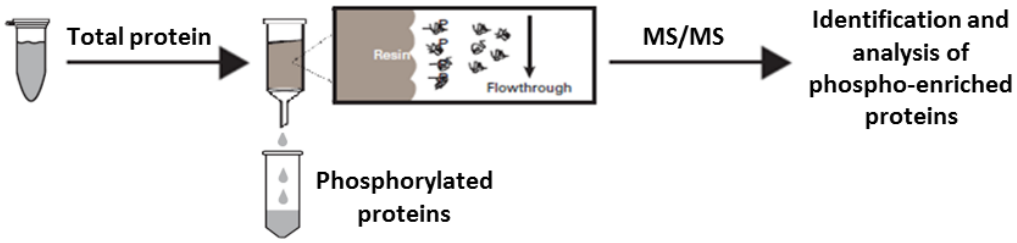

Figure 2.2 Overview of the phosphoprotein enrichment approach. Adapted from TALON® PMAC Phosphoprotein Enrichment Kit User Manual (https://www.takarabio.com/documents/User%20Manual/TALON%20PMAC%20Phosphoprotein%20Enrichment%20Kit%20User%20Manual%20%28PT3731/TALON%20PMAC%20Phosphoprotein%20Enrichment%20Kit%20User%20Manual%20%28PT3731-1%29_071414.pdf).

2.9.2 Phosphoprotein Precipitation and Preparation

The phospho-enriched fractions 2 and 3, which had the highest concentration of proteins, needed to be concentrated to reduce sample volume. This was achieved by reducing the volume to 500 µL using a speed vacuum concentrator (SpeedVac, ThermoFisher Scientific). Then to remove the high concentration salt in the samples buffer, we used the ProteoExtract® Protein Precipitation Kit (Merck-Millipore). Samples were mixed with the cold precipitation agent, incubated overnight at -20ºC and centrifuged at 10000 *xg* for 10 min at RT. After 2 washes in cold wash solution, the pellet was dried at room temperature. Then, in the spectrometry service (i3S, Porto) 100 µg of protein from each sample were processed for proteomic analysis following the solid-phase-enhanced sample-preparation protocol as described in Hughes, C.S. et al.[127]. Enzymatic digestion was performed with trypsin/LysC (2 µg) overnight at 37ºC at 1000 rpms, and the resulting peptide concentration was measured by fluorescence.

2.9.3 Phosphoprotein Data Acquisition

Following sample preparation, protein identification and quantitation were performed by nano Liquid Chromatography with tandem mass spectrometry (LC-MS/MS) (Ultimate 3000 liquid chromatography system coupled to a Q-Exactive Hybrid Quadrupole-Orbitrap mass spectrometer; ThermoFisher Scientific) in the spectrometry service (i3S, Porto) according to the protocol described in Osório et al.[128]. The data acquisition was controlled by Xcalibur 4.0 and Tune 2.9 software (ThermoFisher Scientific).

In collaboration with the spectrometry service of i3S, the acquired raw data were processed using the Proteome Discoverer 2.5.0.400 software (ThermoFisher Scientific). Protein identification analysis was performed with the data available in the UniProt protein sequence database for the Reviewed Homo sapiens Proteome 2021_03 with 20,371 entries and a common contaminant database from MaxQuant (version 1.6.2.6, Max Planck Institute of Biochemistry). Two protein search algorithms were considered: (i) the mass spectrum library search software MSPepSearch, with the NIST human HCD Spectrum Library and (ii) the Sequest HT tandem mass spectrometry peptide database search program, through an ion mass tolerance of 10 ppm for precursor ions and 0.02 Da for fragment ions. The maximum allowed missing cleavage sites was set to 2. Cysteine carbamidomethylation was defined as constant modification. Methionine oxidation, asparagine and glutamine deamidation, phosphorylation of serine, threonine and tyrosine, peptide N-terminus Gln->pyro-Glut, protein N-terminus acetylation, and loss of methionine and Met-loss+Acetyl were defined as variable modifications. Peptide confidence was set to high. The Inferys rescoring node, which calculates intensity-based similarity scores for peptide-to-spectrum matches (PSMs), was considered for this analysis. The Percolator node was enabled to filter PSMs with the following settings: maximum delta Cn 0,05; decoy database search target False Discovery Rate (FDR) 1%; validation based on q-value.

Protein-label-free quantitation (LFQ) of isotope features was performed with the Minora feature detector node. Precursor ion quantification was performed at the processing step with the following parameters: peptides - unique plus razor; precursor abundance was based on intensity; normalization

mode was based on the total peptide amount; the minimum number of replicate files that a feature must be detected in to be used was set to half in the sample group; the pairwise protein ratio calculation and hypothesis test were based on a t-test (background based). The ptmRS node was used to calculate the probability (confidence) that the phosphorylation of serine, threonine and/or tyrosine is present within the peptide. Based on the observed fragment ions, it assigns a percent confidence score that represents the localization probability. The Feature Mapper node was used to create peptide features from unique peptide-specific peaks, reducing missing values, by applying a chromatographic retention time alignment with a maximum shift of 10 min and 10 ppm of mass tolerance. For feature linking and mapping, the minimum Mutant vs. Wild-type signal to noise threshold was set at 5.

2.9.4 Phosphoprotein Functional Enrichment Analysis

For the determination of differentially expressed proteins between the FLAG-TTBK2-WT and -L209F (Mutant) cell samples, the following filters were considered: (1) the minimum number of samples that a protein must be detected was set to 50% per experimental group; (2) the use of at least two unique peptides with the exception of proteins with a MW lower than 30 kDa; (3) the *P-value* adjusted using Benjamini-Hochberg correction for the FDR set to ≤0.05; (4) the L209F/WT considered ratio was set to ≥1.60 for the selection of upregulated proteins and to ≤0.625 for downregulated proteins; (5) in least 50% of samples (minimum 2 out of 3) with protein-related peptides sequenced by MS/MS.

The protein functional enrichment analysis was performed with the WebGestalt tool[129]. The Over-Representation Analysis (ORA) was performed by inputting a list of significant differentially expressed proteins under the following conditions: minimum/maximum number of genes for a category 5/2000 and significance level $P \leq 0.05$, with the *P-values* adjusted following the Benjamini-Hochberg methodology. The reference list was the default genome protein-coding present in the software. The weighted set cover redundancy reduction method was included as a post-processing step, allowing to identify the most representative significant sets by finding a minimum subset of gene sets that can cover all the enriched sets of genes, associated with its *P-value*. The Gene Set Enrichment Analysis (GSEA) is based on a ranked list determined by t-statistic values between the two groups for all quantified proteins, and the following parameters were considered: minimum/maximum number of genes for a category, 5/2000; significance level $P \leq 0.05$; 1000 permutations. For both ORA and GSEA approaches, the following Functional Databases were considered: Gene Ontology (BP - Biological Process, CC - Cellular Component and MF - Molecular Function)[130,131], Pathway (KEGG[132,133], Panther[134], Reactome[135,136] and Wikipathway[137] and Disease (Disgenet[138], GLAD4U[139] and OMIM[140]).

2.9.5 Phosphosites Analysis

The phosphosites identified in the differentially expressed proteins were analysed using: PhosphositePlus v6.6.0.2 (https://www.phosphosite.org/homeAction)[141], Phospho.ELM v.9.0 (http://phospho.elm.eu.org/index.html)[142], and PhosphoNet (http://www.phosphonet.ca/)[143] databases.

2.10 Statistical Analysis

The statistical analysis was performed using the IBM SPSS Statistics 25.0 sofware. All quantitative data are expressed as mean ± standard deviation (SD) of at least three independent experiments. Statistical significance analysis was conducted using one-way Analysis of variance (ANOVA) with Tukey' post-hoc tests, when comparing means of more than two groups, or two-tailed Student's t-test to compare means between two groups. Non-parametric tests were used when normality (Shapiro-Wilk) and/or homogeneity of the variances (Levene) was not observed, such as Mann-Whitney U test. The level of statistical significance was set at *P*-value ≤0.05.

3
RESULTS

3.1 Identification of a novel potentially pathogenic *TTBK2* variant

In a previous study in collaboration with the CGPP (Centro de Genética Preditiva e Preventiva, i3S, Porto), two siblings exhibiting cerebellar ataxia without a conclusive genetic diagnosis were identified. The available medical history of the proband (II.1) (Figure 3.1A) indicates a clinical diagnosis of sensitive ataxia and cerebellum atrophy, presenting gait imbalance at 48 years old, which progressed to visual impairment, nystagmus, and ataxia at 53 years old. In addition, there was a first-degree case (II.2, sister) (Figure 3.1A) with progressive ataxia and neuropathy, dysarthria and cerebellum atrophy. The two affected Portuguese siblings (Figure 3.1A) were first excluded for all autosomal dominant ataxias of triplets expanded repeats, as well as the most common recessive ataxias, such as FRDA, AOA1 and AOA2. Then, since the clinical phenotype of the patients suggest that SCA11 might be the genetic cause[29,31,33], PCR amplification of all *TTBK2* exons and intronic flanking regions was performed. This analysis led to the identification of a novel heterozygous missense variant in *TTBK2* gene (ENST00000267890.11: c.625C>T; p.Leu209Phe) (Figure 3.1B and C).

The variant (chr15:42,811,759; c.625C>T; p.Leu209Phe) located within the exon 8 of *TTBK2* (Figure 3.1C) had a minor allele frequency of $6{,}58 \times 10^{-06}$ in the population with only one allele count described in the gnomAD database. The variant was reported as rs1595936604 in the dbSNP.

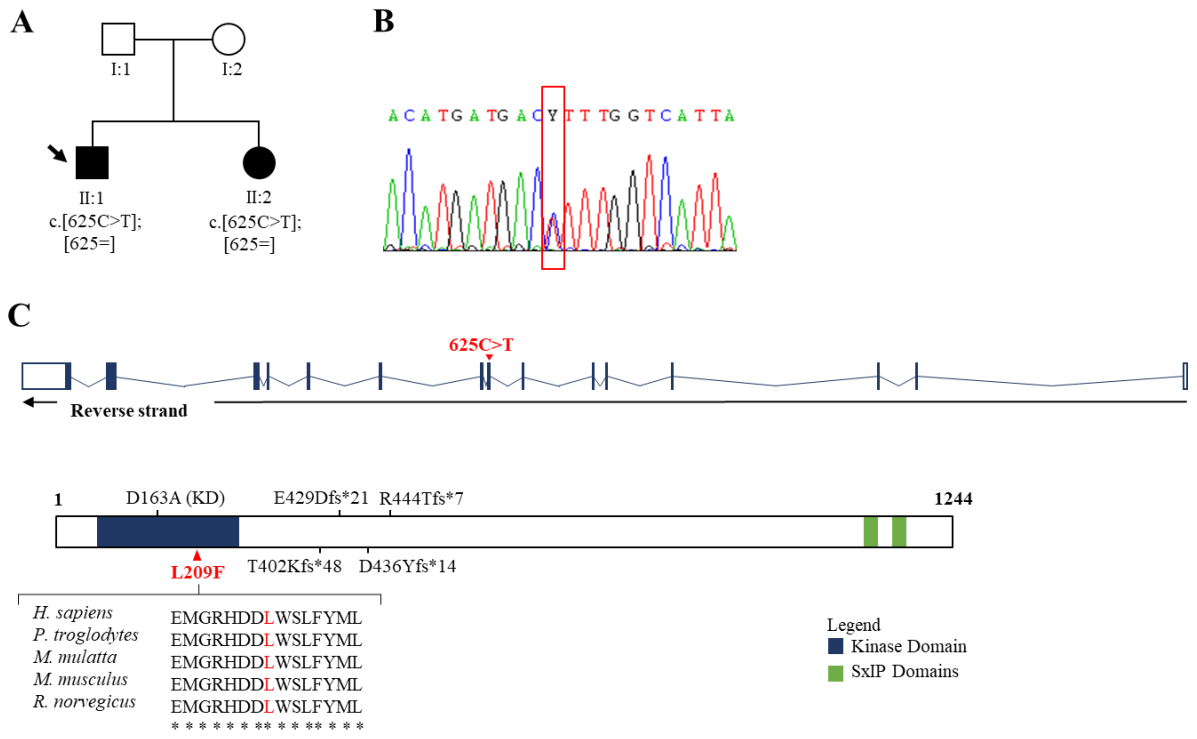

Figure 3.1 The family pedigree and a schematic representation of the TTBK2 gene and protein. (A) A pedigree with the new *TTBK2* variant (c.625C>T; p.Leu209Phe) identified in two siblings. The arrow indicates the proband, filled black symbols indicate affected family members by cerebellar ataxia, circles indicate females and squares indicate males. (B) An electropherogram showing the heterozygous *TTBK2* c.625C>T variant boxed in red. (C) The localization of the identified variant (c.625C>T; Leu209Phe) (in red) in the *TTBK2* gene and protein (NP_775771.3/Q6IQ55-1), a KD variant (Asp163Ala) that disables the kinase domain activity and known SCA11 frameshift variants (Thr402fs; Glu429Aspfs*21; Asp435Tyrfs*14; Arg444Thrfs*7). A sequence alignment of the flanking residues of L209 of human TTBK2 against other species was performed using the Clustal Omega program.

The p.Leu209Phe variant locates within an alpha helix of an annotated kinase domain (Figure 3.1C, 3.2) and leads to the alteration of a leucine (aliphatic side chain) to a phenylalanine (aromatic side chain) on a residue buried in the core of the protein (Figure 3.2). A functional *in silico* analysis based on several pathogenicity prediction programs was done, which predicted the amino acid substitution (p. Leu209Phe) to be deleterious (e.g., SIFT = 0.01 (deleterious); Polyphen = 0.999 (probably damaging); CADD = 28; Mutation Taster = 1 (disease causing); MutPred = 0,6) (Table 3.1; Annex II - Table S3.1). The phylogenetic analysis showed that the new variant is within a highly conserved position in terms of nucleotide (GERP++ RS = 5,57; PhastCons100way = 1,00; PhyloP100way = 10,003) and protein, across different species (Table 3.1; Figure 3.1C).

Table 3.1 Summary table showing the TTBK2 variant (c.625C>T; p.Leu209Phe) nucleotide conservation and pathogenicity prediction scores.

Nucleotide Conservation			Pathogenicity				
GERP++ RS	PhastCons 100way	PhyloP 100way	SIFT	Polyphen	CADD	MutationTaster	MutPred
5,57	1,00	10,003	0,01	0,999	28,00	1	0,6

CADD and Mutpred scores are considered as pathogenic above 20 and 0,5, respectively. In nucleotide conservation scores, the larger the score, the more conserved the site. GERP++ RS, PhastCons100way and PhyloP100way

scores range from -12,3 to 6,17; 0 to 1; and -20 to 10,003, respectively. Additional programs and scores can be found in Annex II - Table S3.1.

To complement the previous results, an analysis on the protein stability was done based on prediction programs that evaluates changes in folding free energy (ΔΔG). This converged to assess a destabilizing effect of the missense variant in TTBK2 protein (PDB accession: 6VRF[144]) (Table 3.2), predicted to increase on aromatic and hydrophobic contacts with the neighboring residues (Figure 3.2).

Table 3.2 Prediction of protein stability changes of TTBK2 Leu209Phe variant.

ΔΔG predictions					
DynaMut	DynaMut2	mCSM	SDM	ENCoM	DUET
0.228 kcal/mol (stabilizing)	-1,95 kcal/mol (Destabilizing)	-1.891 kcal/mol (Destabilizing)	-1.390 kcal/mol (Destabilizing)	0.260 kcal/mol (Destabilizing)	-2.132 kcal/mol (Destabilizing)

The protein stability analysis revolves around bioinformatic assessment of ΔΔG variations between WT and altered proteins.

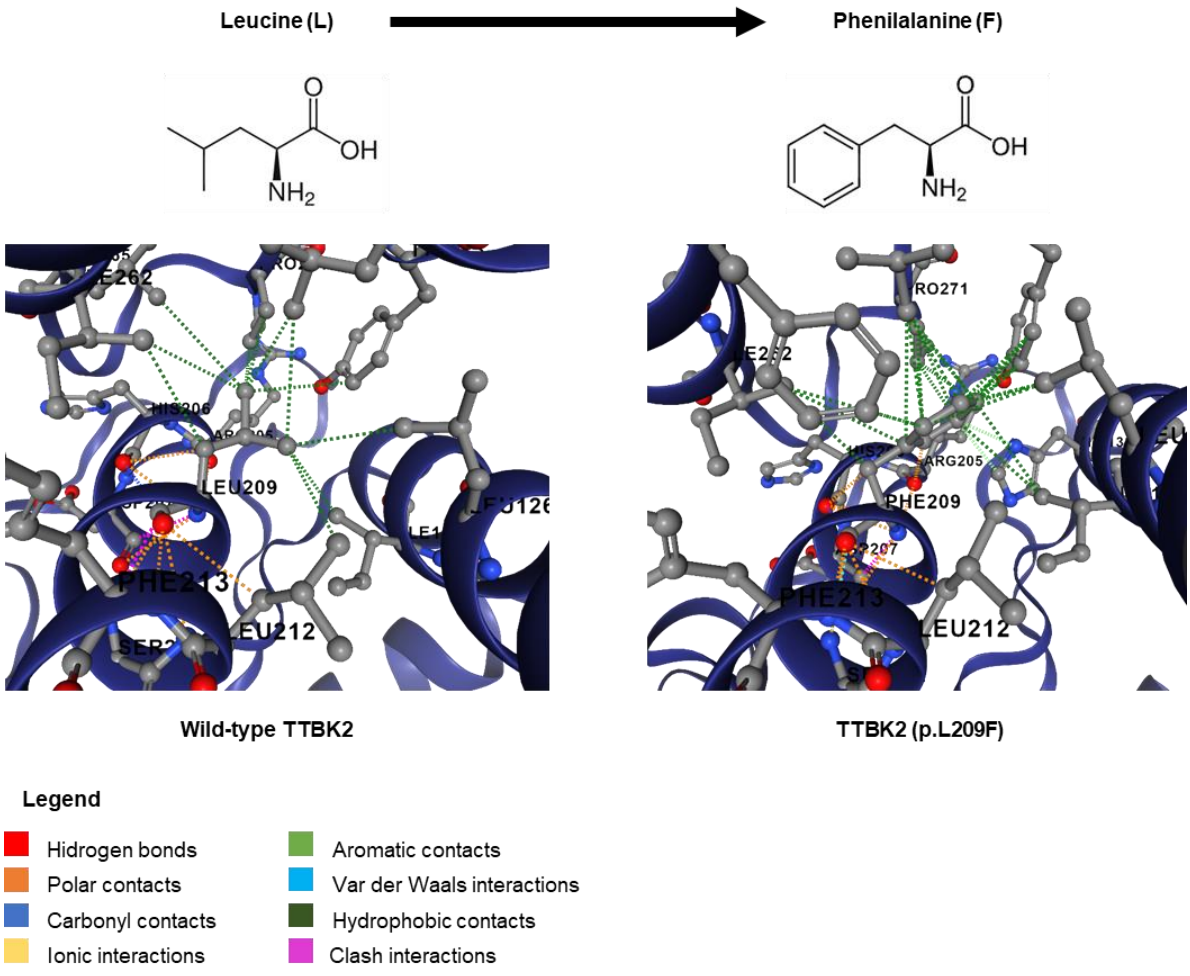

Figure 3.2 The Leu209Phe variant alters residues interactions in the core of the protein. The prediction of the variant impact on stability and protein dynamics was done using the web server DynaMut2. The 209 residue is centered displaying the various interactions with nearby residues in different colours.

3.2 The new variant (c.625C>T; p.Leu209Phe) affects TTBK2 protein expression

To study the impact of p.Leu209Phe variant on the expression of TTBK2, constructs that direct the expression of TTBK2 wild-type (EGFP-TTBK2-WT), TTBK2 carrying the D163A variant (loss of kinase function; EGFP-TTBK2-KD), or the L209 variant (EGFP-TTBK2-L209F), in fusion with a N-terminal EGFP-tag, were generated. Constructs, including the control construct (empty vector), were transfected into HEK293T cells. Immunoblotting analysis revealed that EGFP-TTBK2-KD and EGFP-TTBK2-L209F had significantly reduced protein levels compared with EGFP-TTBK2-WT (Figure 3.3A, about an 80% and 60% decrease; *P-value* = 0,005 and 0,001, respectively). To note that, both TTBK2 KD and Leu209Phe proteins presented the expected molecular weight of about 164 kDa (about 137 kDa from TTBK2 plus 27 kDa from EGFP) (Figure 3.3A).

Then, to analyse endogenous TTBK2, CRISPR-Cas9-mediated knock-in of the variant c.625C>T (FLAG-TTBK2-L209F) was performed in a HEK293T cell line expressing TTBK2 in fusion with an N-terminal 3xFLAG-tag (FLAG-TTBK2). After the CRISPR-Cas9 assay (co-transfection with the gRNA, ssODN, in the presence of the NHEJ inhibitor NU7026) and single cell sorting, the cell clones repaired by HDR were first genotyped through AvaII digestion. Then, the correct insertion of the *TTBK2* c.625C>T variant (in homozygosity) and surrounding genomic sequence was verified by Sanger sequencing. All *TTBK2* exons and predicted off-targets were also sequenced to exclude potential off-target effects. The newly created and validated FLAG-TTBK2-L209F (FLAG-L209F) CRISPR/Cas9 modified cell line and the control FLAG-TTBK2-WT (FLAG-WT) CRISPR/Cas9 modified cell line (previously established) were used to perform the following experiments.

The TTBK2 protein expression, evaluated by Western blot, revealed a significant decrease in TTBK2 proteins levels on the FLAG-TTBK2-L209F cell line compared to the FLAG-TTBK2-WT cell line (Figure 3.3B, about a 60% decrease; *P-value* = 0,023). Quantitative RT-PCR showed no significant reduction on TTBK2 mRNA levels (using either primers targeting exon 4 or exon 8 of *TTBK2*), confirming that the variant does not result in reduction or instability of the mRNA (Figure 3.3C). In addition, we also showed that the introduction of the 3xFLAG-tag does not influence TTBK2 mRNA expression (comparison between HEK293T and FLAG-TTBK2-WT and -L209F modified cells) (Figure 3.3C).

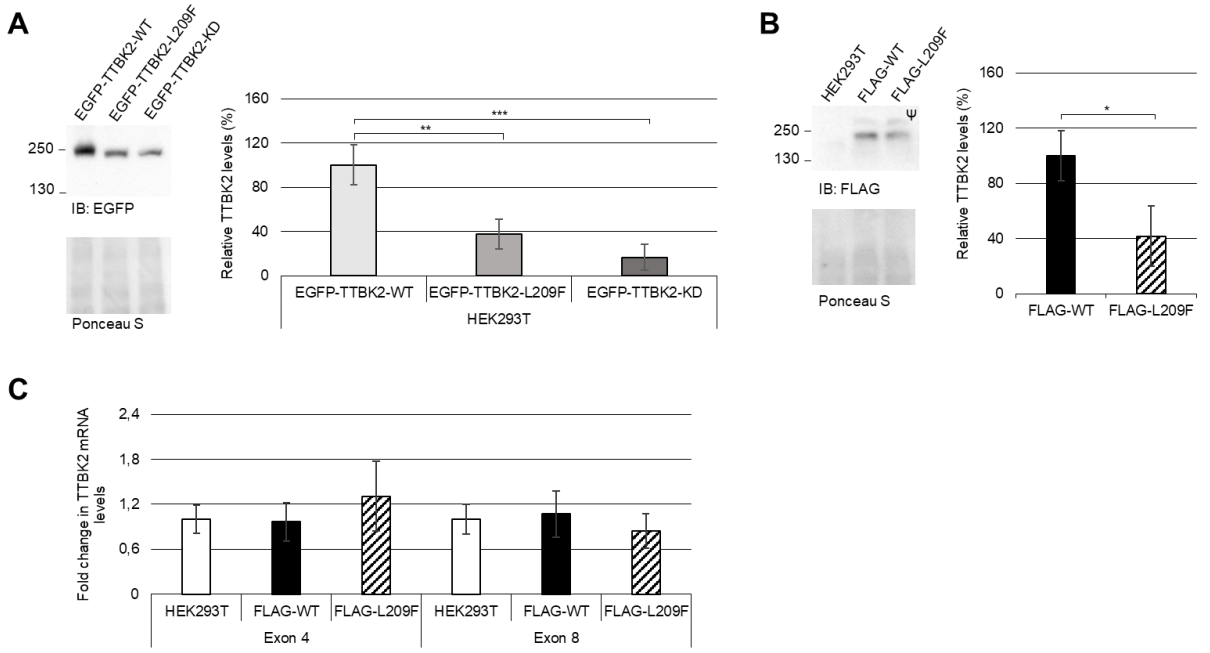

Figure 3.3 The Leu209Phe variant reduce TTBK2 protein expression. (A) Analysis of TTBK2 protein expression of EGFP-tagged TTBK2 clones in HEK293T cells by immunoblotting with anti-EGFP antibody. Ponceau S staining was used as the loading control. Quantification data (graph) are presented in percentage as the mean ± SD of three independent experiments; **p ≤ 0.01, ***p ≤ 0.001 compared with FLAG-TTBK2-WT transfection condition (one-way ANOVA/Tukey). (B) Analysis of endogenous TTBK2 protein expression in FLAG-TTBK2-WT and –L209F cells (CRISPR-cas9 modified cells) by immunoblotting with anti-FLAG antibody. Ponceau S staining was used as the loading control. Quantification data (graph) are presented in percentage as the mean ± SD of three independent experiments; *P ≤ 0,05 compared with FLAG-TTBK2-WT cell line (T-test). Ψ identifies an unspecific band. (C) Analysis of TTBK2 mRNA levels in CRISPR-cas9 modified HEK293T cells by RT-qPCR. Quantification data (graph) are presented in fold change as the mean ± SD of three independent experiments; compared with HEK293T (one-way ANOVA/Tukey).

3.3 Characterization of the subcellular localization of TTBK2

Previous studies showed a protein localization of TTBK2 in the cytoplasm[46,145], also being present in cytoskeleton related structures as primary cilia, midbody and mitotic spindle during cell division[46,55,56]. However, SCA11 variants had been reported to enhance nuclear localization[36]. Thus, a study on the subcellular localization of TTBK2 was performed by fluorescence microscopy and subcellular fractionation of FLAG-TTBK2-WT and -L209F cells. TTBK2 proteins were labelled with anti-FLAG antibody and Hoechst was used to mark the nucleus. Both WT and Leu209Phe TTBK2 proteins were located mainly in the cytoplasm and seemed to be present within the nucleus in a minor extent (Figure 3.4A).

The subcellular localization of WT and Leu209Phe TTBK2 was confirmed by subcellular protein fractionation. The fractionation method efficiency was controlled by immunoblotting using specific antibodies for each fraction isolated: β-actin (total fraction), caspase 3 (cytoplasmic fraction), Cis-Golgi matrix protein 130 kDa (GM130) (membrane fraction), HDAC2 (soluble nuclear fraction), histone H3 (chromatin-bound nuclear fraction), and CEP97, α-tubulin and vimentin (cytoskeletal fraction). Presence of TTBK2 in each fraction was analysed by immunoblotting with anti-FLAG antibody. TTBK2 protein was mainly present in the cytoplasmic fraction. In addition, a band with a high molecular weight of about 300

kDa was also detected in the cytoskeletal fraction; but the specificity of this band remains unknown and have not yet been reported in other studies. (Figure 3.4B). Moreover, most of the cytoskeleton specific markers seem to be extracted not only with the cytoskeleton fraction but also with the cytoplasmic and other fractions (Figure 3.4B). The Leu209Phe variant was collected in a similar pattern to TTBK2 WT, showing no apparent changes in TTBK2 levels in the cytoplasm or cytoskeletal fractions (Figure 3.4B).

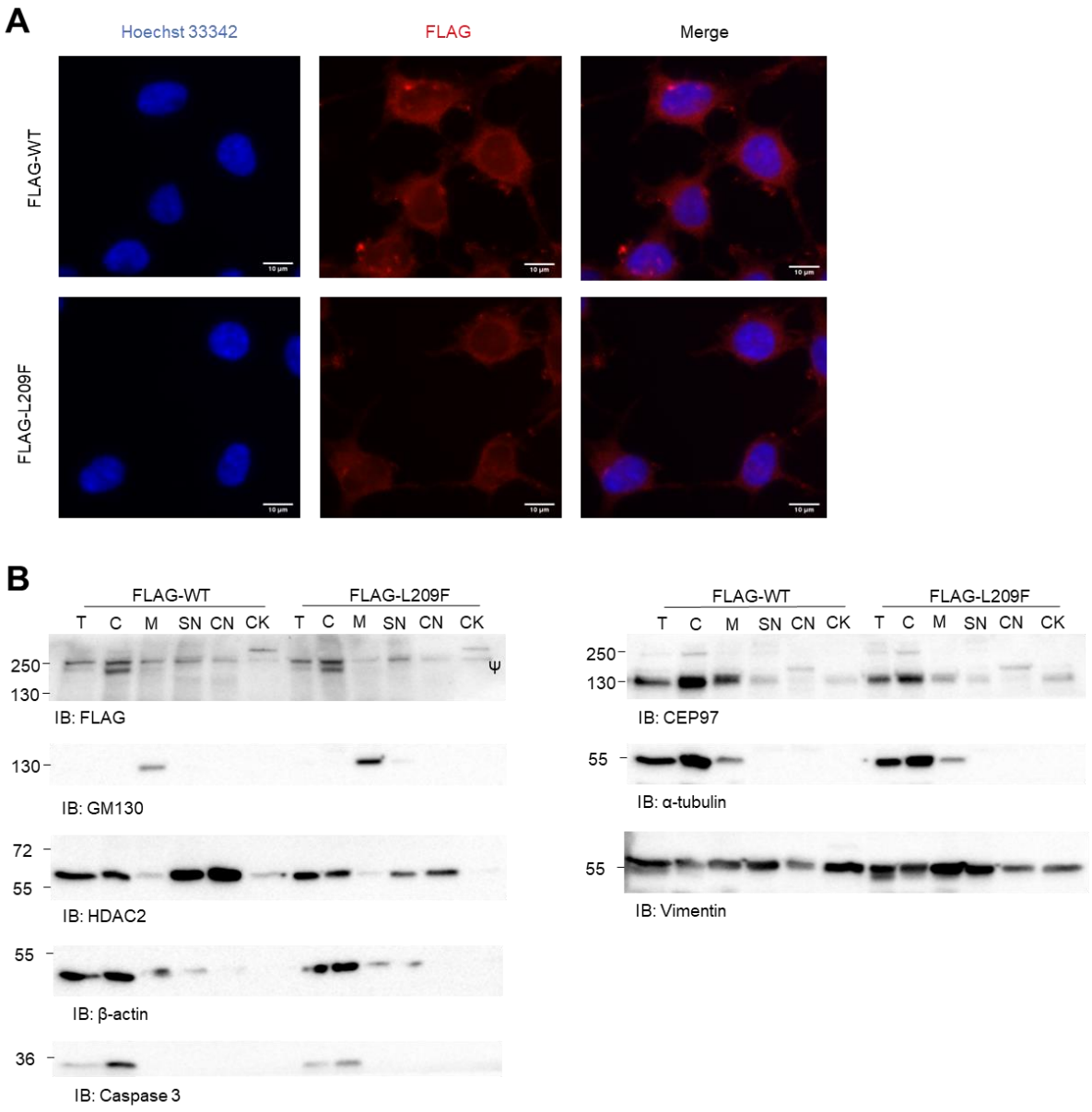

Figure 3.4 TTBK2 locates in the cytosol and Leu209Phe variant does not affect its subcellular localization. (A) Immunofluorescence showing the localization of endogenous TTBK2 in FLAG-TTBK2-WT and –L209F cells fixed in microscopy buffer and incubated with anti-FLAG antibody, followed by detection with Alexa Fluor 568-conjugated secondary antibody (red) (n=1). The nucleus was stained with Hoechst 33342 (blue). Photographs were acquired using a Zeiss Axio Imager Z1 microscope. Bars, 10 µm. (B) Subcellular fractionation of FLAG-TTBK2-WT and -L209F cells. Presence of TTBK2 with the anti-FLAG antibody was evaluated in each fraction with specific markers such as β-actin (total fraction), caspase 3 (cytoplasmic fraction), GM130 (membrane fraction), HDAC2 (soluble nuclear fraction), histone H3 (chromatin-bound nuclear fraction), and CEP97, α-tubulin and vi-

mentin (cytoskeletal fraction) antibodies (n=1). Ψ identifies an unspecific band. T, total protein fraction; C, cytoplasmatic protein fraction; M, membrane protein fraction; SN, soluble nuclear protein fraction; CN, chromatin-bound nuclear protein fraction; CK, cytoskeletal protein fraction.

3.4 The TTBK2 Leu209Phe variant may affect cytoskeleton dynamics

The TTBK2 protein was first reported as a tau and tubulin kinase *in vitro*[42,43], and since then TTBK2 have been described to be essential for ciliogenesis initiation[46,71] and to regulate microtubule-depolymerisation by inhibiting KIF2A activity via EB1[48]. Therefore, protein expression of KIF2A and acetylated α-tubulin, known as an indicator of microtubules stability[146,147], was assessed by immunoblotting. Both KIF2A and acetylated α-tubulin protein levels were decreased in FLAG-TTBK2-L209F cells comparing to FLAG-TTBK2-WT cells (Figure 3.5A, about a 50% decrease in both; *P-value* = 0,035 and 0,031, respectively). The changes in acetylated α-tubulin protein levels were not due alterations in α-tubulin protein expression (Figure 3.5A). The fluorescence microscopy of FLAG-TTBK2-WT and -L209F cells support the immunoblotting data, but quantification of fluorescence intensity still needs to be performed (Figure 3.5B).

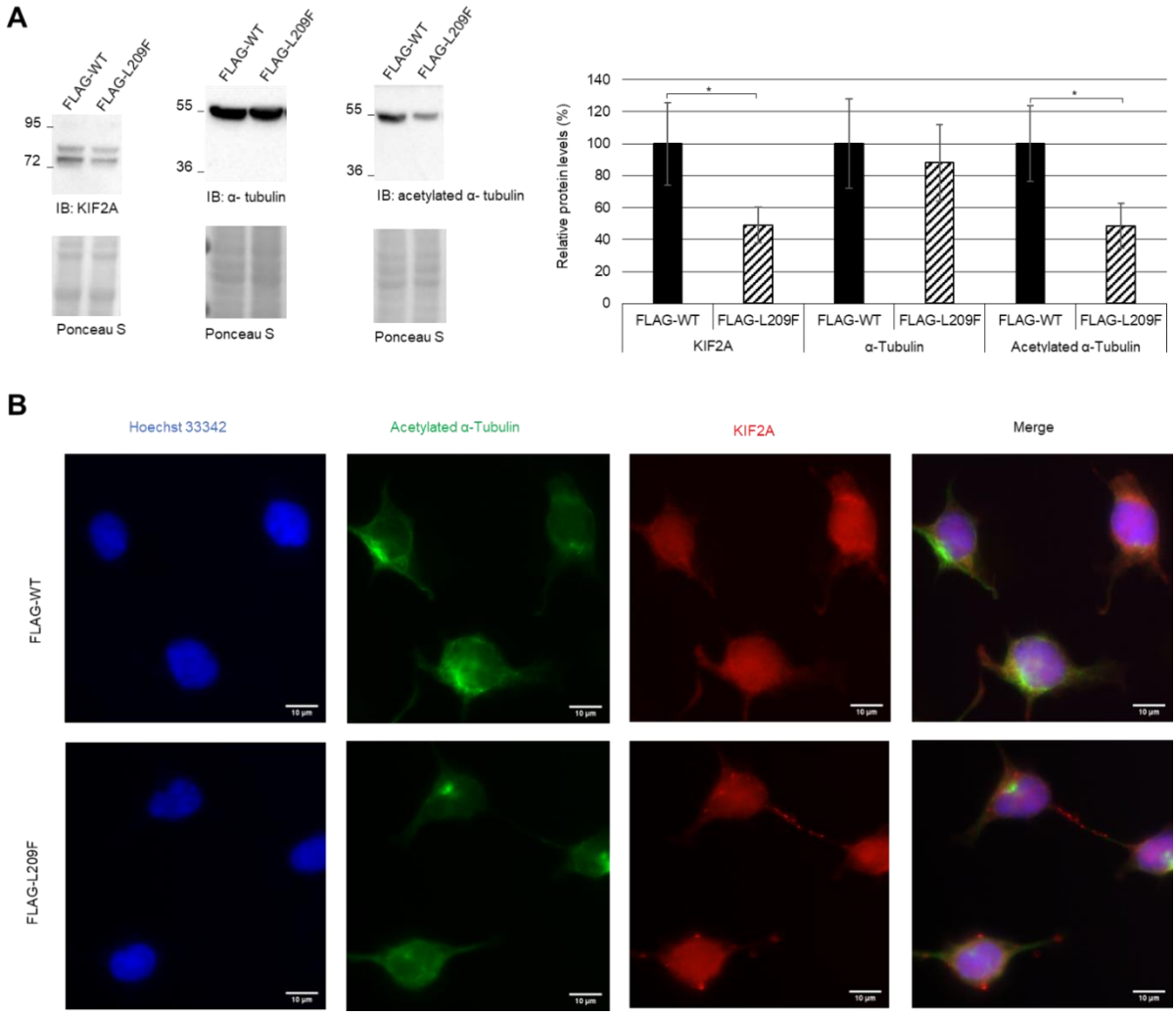

Figure 3.5 The Leu209Phe variant alters KIF2A expression and α-tubulin acetylation. (A) Analysis of KIF2A, α-tubulin and acetylated α-tubulin protein expression in FLAG-TTBK2-WT and –L209F cells by immunoblotting with anti-KIF2A, anti-α-tubulin and anti-acetylated α-tubulin antibodies. Ponceau S staining was used as the loading control. Quantification data (graph) are presented in percentage as the mean ± SD of three independent experiments, *p ≤ 0,05 (T-test). (B) Immunofluorescence of KIF2A and acetylated α-tubulin in FLAG-TTBK2-WT and –L209F cells fixed in 4% paraformaldehyde/4% sucrose, followed by incubation with anti-KIF2A and anti-acetylated α-tubulin antibodies and detection with Alexa Fluor 568 (red) and Alexa Fluor 488 (green) -conjugated secondary antibodies, respectively (n=1). The nucleus was stained with Hoechst 33342 (blue). Photographs were acquired using a Zeiss Axio Imager Z1 microscope. Bars, 10 µm.

To confirm the direct involvement of the Leu209Phe variant in KIF2A expression levels, a rescue experiment was performed by the transient transfection of the empty vector EGFP, EGFP-TTBK2-WT or EGFP-TTBK2-L209F in FLAG-TTBK2-WT and –L209F cells.

Immunoblotting analysis showed that FLAG-TTBK2-L209F cells transfected with EGFP-TTBK2-WT revealed twice the KIF2A proteins levels observed in the presence of EGFP or EGFP-TTBK2-L209F (Figure 3.6). Therefore, KIF2A defects in FLAG-TTBK2-L209F cells seem to be rescued by the EGFP-TTBK2-WT transfection. In addition, EGFP-TTBK2-L209F transfection decreases about 20% of KIF2A protein expression in FLAG-TTBK2-WT cells, but since the EGFP-TTBK2-L209F levels are much smaller than of the EGFP-TTBK2-WT, these findings may not demonstrate the total effect of the Leu209Phe variant (Figure 3.6).

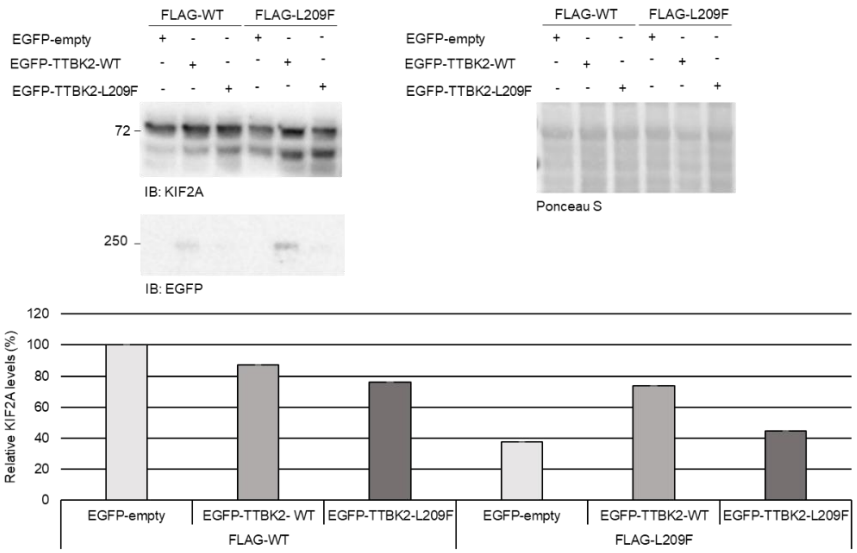

Figure 3.6 KIF2A expression was rescued by the TTBK2-WT overexpression. Analysis of KIF2A protein expression in FLAG-TTBK2-WT and –L209F cells transfected with the empty vector EGFP, EGFP-TTBK2-WT or EGFP-TTBK2-L209F by immunoblotting with anti-KIF2A and anti-EGFP antibodies. Ponceau S staining was used as the loading control. Quantification data (graph) are presented in percentage as the values of one experiment.

3.5 The TTBK2 Leu209Phe variant may influence autophagy

Autophagy impairment has been associated with neurodegeneration and the accumulation of misfolded proteins, and its induction has been shown to be beneficial[148,149]. Thus, a study on the protein expression of several autophagy players was done to verify if the Leu209Phe variant was linked to

autophagy impairment. Immunoblotting analysis demonstrated that the levels of regulatory-associated protein of mTOR (Raptor), Unc-51 like autophagy activating kinase 1 (ULK1) and Beclin 1 in the FLAG-TTBK2-L209F cells were increased for about 40%, 90% and 40%, respectively (Figure 3.7A, *P-value* = 0,087; 0,016; and 0,060, respectively). Interestingly, the cellular levels of the phosphorylated (activated) forms of these proteins significantly accompanied the increases in their expression levels (Figure 3.7A, about an increase of 60%, 100% and 40%; *P*-value = 0,008; 0,01; and 0,041, respectively) in FLAG-TTBK2-L209F cells. These results suggest that there are higher levels of autophagy-related active proteins in the presence of the Leu209Phe variant. However, when normalising the phosphorylated to the respective total protein levels, there were no significant differences in Raptor (Ser792), ULK1 (Ser555) and Beclin 1 (Ser93) levels between FLAG-TTBK2-L209F and -WT cells (Figure 3.7A).

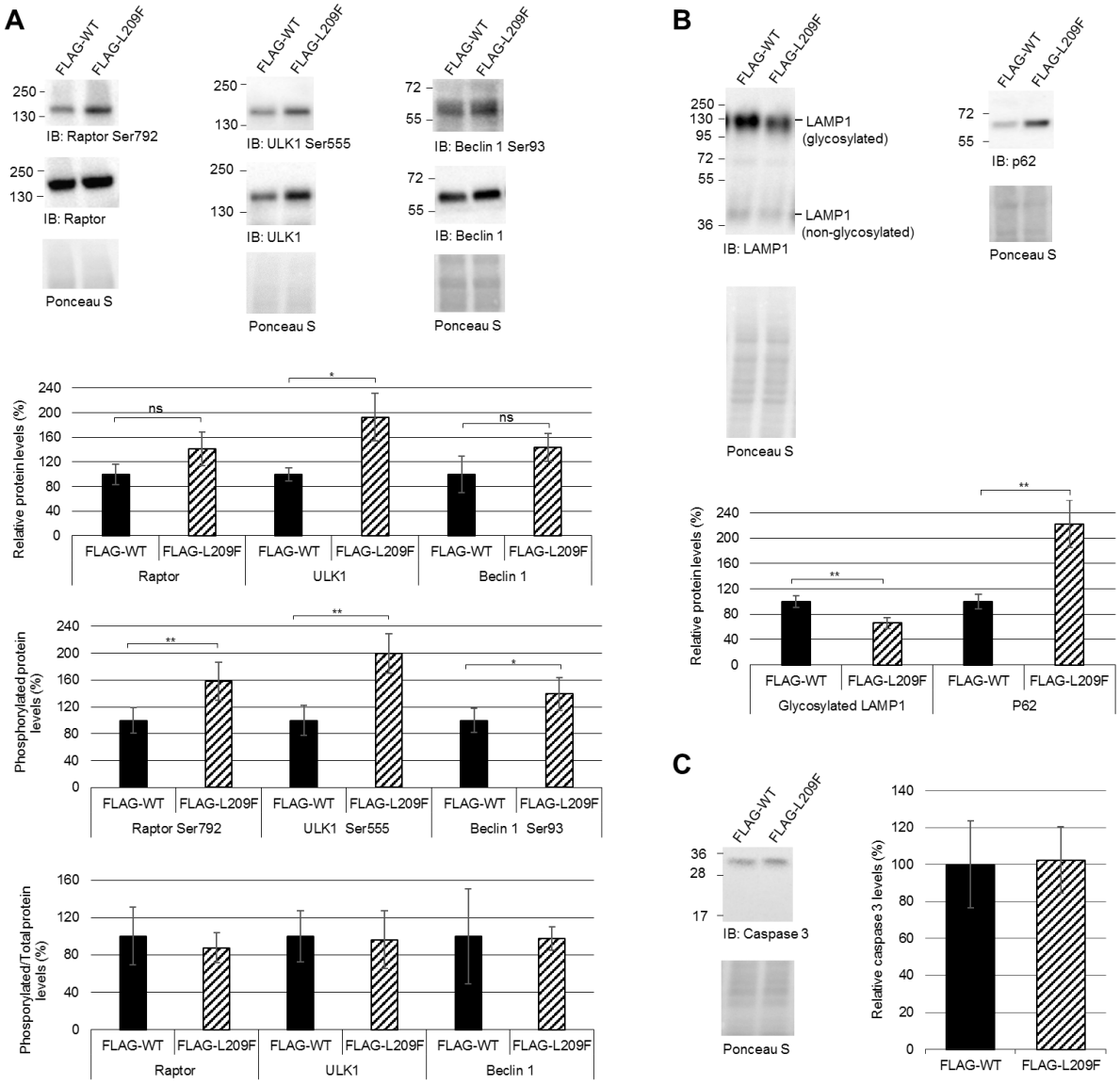

Figure 3.7 The TTBK2 Leu209Phe variant affects the expression of several autophagy related proteins. (A) Protein expression analysis of upstream autophagy proteins like Raptor, ULK1 and Beclin 1, plus their phosphorylated forms, and (B) LAMP1 and p62, was performed in FLAG-TTBK2-WT and –L209F cells by

immunoblotting with anti-raptor, anti-phospho raptor (Ser792), anti-ULK1, anti-phospho ULK1 (Ser555), anti-beclin1, anti-phospho beclin1 (Ser93), anti-LAMP1 and anti-p62 antibodies. Ponceau S staining was used as the loading control. Quantification data (graph) are presented in percentage as the mean ± SD of at least three independent experiments, *$P \leq 0{,}05$, **$P \leq 0.01$, ns (non-significant, $P>0.05$) (T-test; non-parametric T-test/Mann-Whitney U test). (C) Analysis of caspase 3 protein expression in FLAG-TTBK2-WT and –L209F cells was done by immunoblotting with anti-caspase 3 antibody. Ponceau S staining was used as the loading control. Quantification data (graph) are presented in percentage as the mean ± SD of three independent experiments (non-parametric T-test/Mann-Whitney U test).

Relatively to lysosomal-associated membrane protein 1 (LAMP1; glycosylated form), a lysosomal marker, and p62 (also known as sequestosome 1 (SQSTM1)), an indicator of both autophagy and UPS, they presented about a two-fold decrease and increase, respectively (Figure 3.7B, *P-value* = 0,009 and 0,006, respectively). In addition, caspase 3 protein levels were maintained in FLAG-TTBK2-L209F cells compared to the -WT cells and no cleaved forms of caspase 3 were detected, showing that the Leu209Phe variant does not lead to apoptosis (Figure 3.7C).

To further analyse the alterations in the autophagic flux and activity, the turnover of microtubule-associated protein 1A/1B-light chain 3 (LC3B)-I/II and p62 after autophagy blockage was assessed. FLAG-TTBK2-WT and –L209 cells were treated with either chloroquine (10 µM during 18h or 25 µM during 2h), an inhibitor of the autophagosome-lysosome fusion[118], or the control vehicle DMEM, and further prepared for immunoblotting or fluorescence microscopy.

Once more, the FLAG-TTBK2-L209F cells showed an increase in p62 protein levels compared to -WT cells, which further increased in the presence of chloroquine, reflecting the autophagy blockage (Figure 3.8A and B). The data from immunoblotting indicated an increase in LC3B-II levels, in the presence of chloroquine (Figure 3.8A and B), suggesting a normal LC3B conversion (LC3B-I to LC3B-II) in both cell lines. By fluorescence microscopy, after treatment of cells with chloroquine, it was visible the presence of LC3B in green puncta (Figure 3.8B) labelling LC3B recruitment to the autophagosomes. Moreover, p62 was also detected in puncta (label in red), some co-localizing with LC3B, possibly indicating the presence of p62 in autophagosomes. However, further co-localization studies should be performed to evaluate differences in LC3B and p62 subcellular localization between FLAG-TTBK2-WT and -L209F cells.

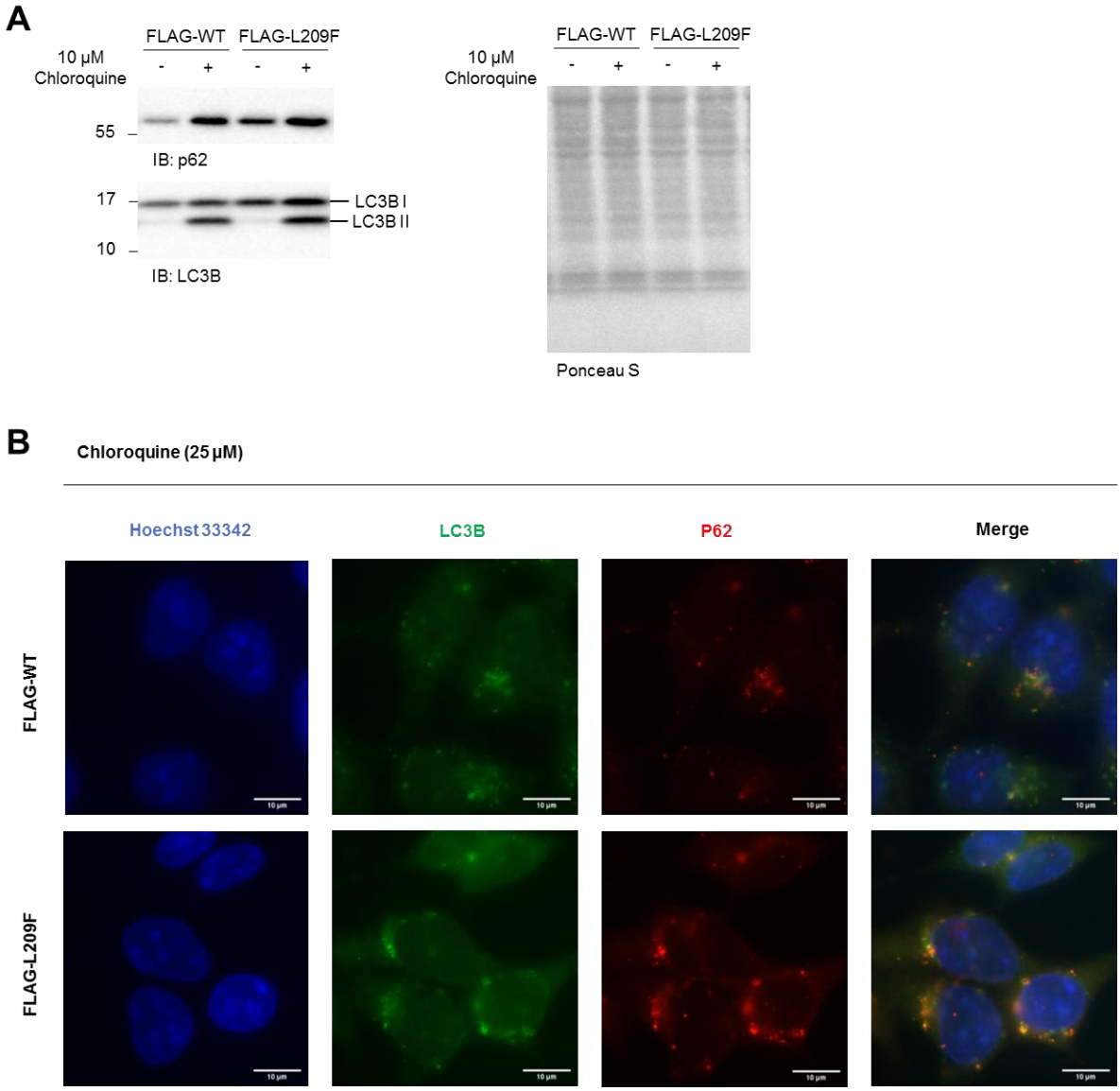

Figure 3.8 The autophagic flux does not seem to be altered in FLAG-TTBK2-L209F cells, however there is an increase in p62 expression. (A) FLAG-TTBK2-WT and –L209F cells were incubated with chloroquine (10µM) or control vehicle DMEM for 18 h, followed by immunoblotting with anti-P62 and anti-LC3 antibodies, along with ponceau S staining as loading control. (B) Immunofluorescence: FLAG-TTBK2-WT and –L209F cells incubated with chloroquine (25µM) for 2 h were fixed in methanol, incubated with anti- P62 and anti-LC3 antibodies, and detected with Alexa Fluor 488 (green) and Alexa Fluor 568 (red) -conjugated secondary antibodies, respectively (n=1). The nucleus was stained with Hoechst 33342 (blue). Photographs were acquired using a Zeiss Axio Imager Z1 microscope. Bars, 10 µm.

3.6 The TTBK2 Leu209Phe variant impairs TDP-43 phosphorylation

The TTBK2 phosphorylates TDP-43, a DNA/RNA binding protein, at Ser409/410 and leads to its re-localization from the nucleus to the cytosol, which is thought to promote toxicity in ALS, FTLD-TDP, and possibly other neurodegenerative diseases[52,53]. Hence, it was verified by immunoblotting if the Leu209Phe variant affected the TTBK2 kinase activity, causing a decrease in the phosphorylation of TDP-43 at Ser409/410. Since the phosphorylated TDP-43 proteins were difficult to analyse in FLAG-

TTBK2-L209F cells, an experiment was performed with the transient transfection of EGFP-FLAG-TTBK2-WT construct in FLAG-TTBK2-WT and –L209F cells to increase phosphorylation of TDP-43 and quantification sensitivity. Immunoblotting analysis showed that transfection of EGFP-FLAG-TTBK2-WT increases the phosphorylation of TDP-43 in FLAG-TTBK2-WT and FLAG-TTBK2-L209F cells by 60% and 80%, respectively (Figure 3.9A). Moreover, phosphorylated TDP-43 levels in non-transfected FLAG-TTBK2-L209F cells were decreased about 90% comparing to non-transfected FLAG-TTBK2-WT cells (Figure 3.9A). The level of Ser409/410 phosphorylation of TDP-43 was normalised to the total TDP-43 level.

Additionally, to analyse Leu209Phe effect on TDP-43 Ser409/410 phosphorylation, an experiment was performed by the transient transfection of the empty vector EGFP, EGFP-TTBK2-WT or EGFP-TTBK2-L209F in FLAG-TTBK2-WT and –L209F cells. Immunoblotting analysis revealed that in FLAG-TTBK2-WT and -L209F cells the TDP-43 phosphorylated levels were increased in the presence of EGFP-TTBK2-WT, but not with EGFP-TTBK2-L209F transfection (Figure 3.9B). However, as the levels of EGFP-TTBK2-L209F are much smaller than of the EGFP-TTBK2-WT, these results may not completely demonstrate the effect of the Leu209Phe variant (Figure 3.9B).

Therefore, both experiments showed that TDP-43 Ser409/410 phosphorylation seems to increase in the presence of WT TTBK2 but not by the Leu209Phe variant (Figure 3.9A and B), indicating a loss-of-function mechanism of the latter (Figure 3.9B).

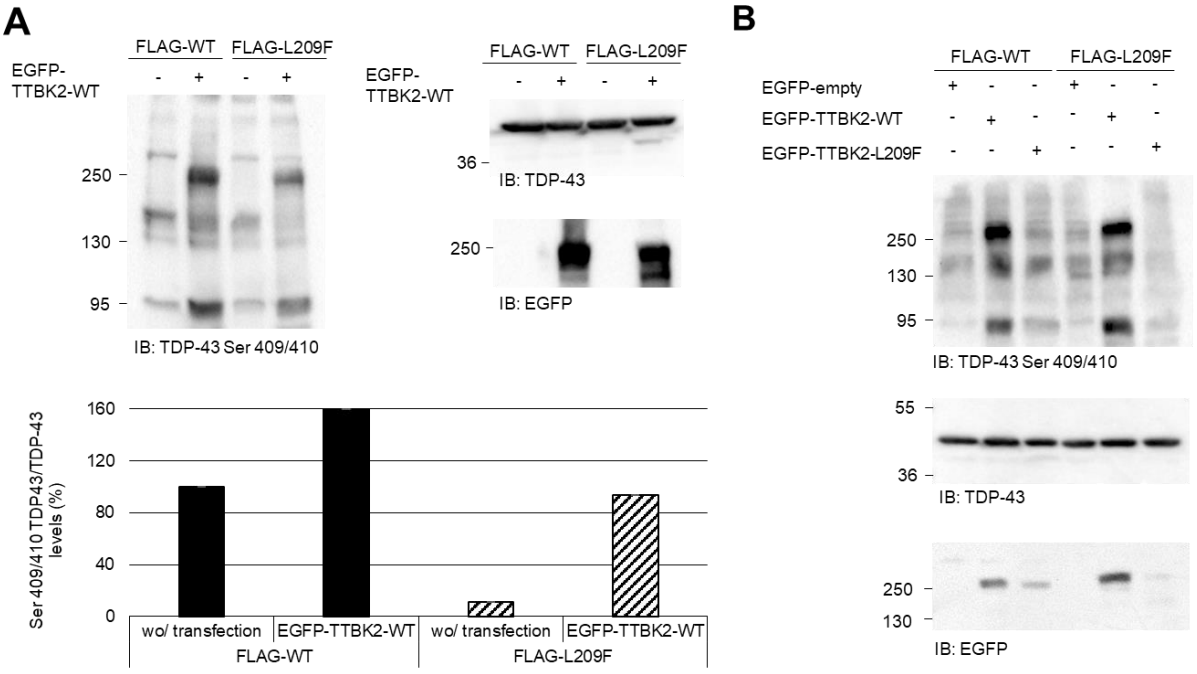

Figure 3.9 The TTBK2 Leu209Phe variant impairs TDP43 phosphorylation. (A) Analysis of TDP43 Ser409/410 levels in FLAG-TTBK2-WT and –L209F cells, non-transfected (wo/ transfection) or transfected with EGFP-FLAG-TTBK2-WT, by immunoblotting with anti-TDP43 Ser409/410, anti-TDP43 and anti-EGFP antibodies. Ser409/410 phosphorylation of TDP-43 was normalised to the total TDP-43 protein. Quantification data (graph) are presented in percentage as the value of one experiment. (B) Analysis of TDP43 Ser409/410 protein levels in FLAG-TTBK2-WT and -L209F cells transfected with the empty vector EGFP, EGFP-TTBK2-WT or EGFP-TTBK2-L209F, followed by immunoblotting with anti-TDP43 Ser409/410, anti-TDP43 and anti-EGFP antibodies (n=1). Total TDP-43 protein was used to normalize Ser409/410 phosphorylation of TDP-43 data.

3.7 The TTBK2 Leu209Phe variant may lead to abnormal protein phosphorylation

Since SCA11 is linked to the loss of function of TTBK2 as reported by others and us in section 3.7, we decided to perform a phosphoprotein enrichment analysis that allows to obtain quantitative information and identify abnormal phosphorylation in human diseases. A total of 5277 proteins were identified among the second and third phospho-enriched fractions of 6 samples, 3 replicates of FLAG-TTBK2-WT and -L209F cells (Figure 3.10). After the removal of common contaminants, the number of identified proteins decreased to 5257 (Figure 3.10). Proteins were considered for the analysis of DEP if detected in 2 out of 3 samples per experimental group, setting the *P*-value adjusted using Benjamini-Hochberg correction for the FDR to ≤0.05. In case of proteins with only one unique peptide, the ones kept had an MW lower than 30 kDa (Figure 3.10). So, in total 4429 quantified proteins were then analysed by performing the FLAG-TTBK2-L209/-WT ratio (Figure 3.10).

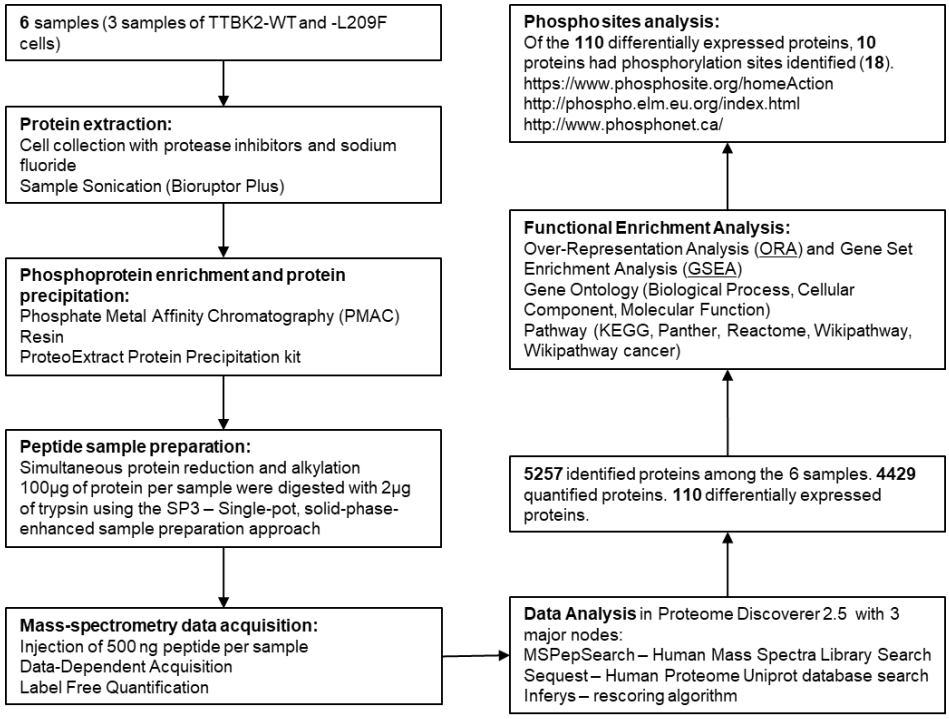

Figure 3.10 Schematic representation of the proteomics workflow for the analysis of FLAG-TTBK2-L209F and -WT cells.

The relative quantification of the phospho-enriched extracts allowed to compare the DEP between the FLAG-TTBK2-L209F cells and the -WT control cells (Figure 3.10, Table 3.3). Considering the L209/WT ratio (≥1,60 for upregulated proteins and ≤0,625 for downregulated proteins), 110 differentially expressed proteins were obtained: 50 upregulated and 60 downregulated (Table 3.3).

Table 3.3 List of DEP between FLAG-TTBK2-L209 and -WT cells.

Protein	Accession No.	Gene Symbol	Fold-Change (L209F/WT)	Unique Peptides	MW [kDa]
HAUS augmin-like complex subunit 2	Q9NVX0	HAUS2	100	1	26,9
Annexin A1	P04083	ANXA1	100	2	38,7
Forkhead box protein M1	Q08050	FOXM1	100	2	84,2
Serine/threonine-protein kinase ULK3	Q6PHR2	ULK3	100	2	53,4
Ubiquitin-associated domain-containing protein 1	Q9BSL1	UBAC1	100	2	45,3
Vesicle-trafficking protein SEC22b	O75396	SEC22B	8,689	1	24,6
Uncharacterized protein C18orf25	Q96B23	C18orf25	2,586	6	43,4
Phosphatidylinositol 3-kinase regulatory subunit gamma	Q92569	PIK3R3	2,472	3	54,4
NAD-dependent malic enzyme, mitochondrial	P23368	ME2	2,412	22	65,4
Oligoribonuclease, mitochondrial	Q9Y3B8	REXO2	2,382	3	26,8
Bardet-Biedl syndrome 7 protein	Q8IWZ6	BBS7	2,366	2	80,3
Keratin, type I cytoskeletal 9	P35527	KRT9	2,282	32	62
Acyl-CoA dehydrogenase family member 11	Q709F0	ACAD11	2,223	13	87,2
Ceroid-lipofuscinosis neuronal protein 5	O75503	CLN5	2,209	2	41,5
Neuromodulin	P17677	GAP43	2,208	1	24,8
Mothers against decapentaplegic homolog 4	Q13485	SMAD4	2,196	17	60,4
AT-rich interactive domain-containing protein 5B	Q14865	ARID5B	2,165	3	132,3
Mucosa-associated lymphoid tissue lymphoma translocation protein 1	Q9UDY8	MALT1	2,08	3	92,2
E3 ubiquitin-protein ligase Midline-1	O15344	MID1	2,062	6	75,2
Insulin receptor substrate 4	O14654	IRS4	2,034	39	133,7
Histone H3.3	P84243	H3-3A/3B	2,022	1	15,3
Asparagine--tRNA ligase, cytoplasmic	O43776	NARS1	1,993	18	62,9
Thioredoxin reductase 1, cytoplasmic	Q16881	TXNRD1	1,984	3	70,9
Slit homolog 2 protein	O94813	SLIT2	1,983	4	169,8
Angiomotin	Q4VCS5	AMOT	1,978	45	118
Profilin-2	P35080	PFN2	1,957	1	15
CBP80/20-dependent translation initiation factor	O43310	CTIF	1,951	8	67,5
Protein ERGIC-53	P49257	LMAN1	1,927	16	57,5
Carboxymethylenebutenolidase homolog	Q96DG6	CMBL	1,91	1	28
Methyl-CpG-binding domain protein 1	Q9UIS9	MBD1	1,895	6	66,6
Angiomotin-like protein 2	Q9Y2J4	AMOTL2	1,825	5	85,7
Keratin, type I cytoskeletal 10	P13645	KRT10	1,805	27	58,8
Histone-lysine N-methyltransferase MECOM	Q03112	MECOM	1,796	10	138
E3 ubiquitin-protein ligase NEDD4-like	Q96PU5	NEDD4L	1,772	13	111,9
WD repeat-containing protein 74	Q6RFH5	WDR74	1,764	10	42,4
SH2 domain-containing adapter protein B	Q15464	SHB	1,755	4	55
Histone H3.2	Q71DI3	H3C13/14/15	1,739	1	15,4
Keratin, type II cytoskeletal 1	P04264	KRT1	1,739	36	66
Sequestosome-1	Q13501	SQSTM1/p62	1,717	9	47,7
E3 SUMO-protein ligase PIAS2	O75928	PIAS2	1,698	7	68,2
Mothers against decapentaplegic homolog 2	Q15796	SMAD2	1,688	4	52,3

Table 3.3 (continued)

Protein	Accession No.	Gene Symbol	Fold-Change (L209F/WT)	Unique Peptides	MW [kDa]
Protein HEXIM1	O94992	HEXIM1	1,673	7	40,6
Zinc finger protein ZIC 2	O95409	ZIC2	1,666	3	55
HIV Tat-specific factor 1	O43719	HTATSF1	1,658	27	85,8
TRAF2 and NCK-interacting protein kinase	Q9UKE5	TNIK	1,654	16	154,8
GMP synthase [glutamine-hydrolyzing]	P49915	GMPS	1,634	16	76,7
Retinoid-inducible serine carboxypeptidase	Q9HB40	SCPEP1	1,624	8	50,8
Methyl-CpG-binding domain protein 2	Q9UBB5	MBD2	1,618	9	43,2
ATP-dependent DNA/RNA helicase DHX36	Q9H2U1	DHX36	1,617	38	114,7
Zinc finger CCCH-type antiviral protein 1-like	Q96H79	ZC3HAV1L	1,602	7	32,9
Far upstream element-binding protein 2	Q92945	KHSRP	0,624	8	73,1
Vacuolar protein sorting-associated protein 4B	O75351	VPS4B	0,624	13	49,3
Inactive phospholipase C-like protein 2	Q9UPR0	PLCL2	0,623	10	125,8
Elongation factor 2	P13639	EEF2	0,621	73	95,3
Integrin-linked protein kinase	Q13418	ILK	0,619	15	51,4
Eukaryotic translation initiation factor 3 subunit M	Q7L2H7	EIF3M	0,614	19	42,5
Cdc42-interacting protein 4	Q15642	TRIP10	0,61	13	68,3
Eukaryotic translation initiation factor 3 subunit K	Q9UBQ5	EIF3K	0,603	6	25
BAG family molecular chaperone regulator 3	O95817	BAG3	0,601	21	61,6
Ribonucleoside-diphosphate reductase large subunit	P23921	RRM1	0,592	18	90
Epiplakin	P58107	EPPK1	0,589	9	555,3
Phostensin	Q6NYC8	PPP1R18	0,581	8	67,9
NAD-dependent protein deacetylase sirtuin-6	Q8N6T7	SIRT6	0,579	7	39,1
mRNA cap guanine-N7 methyltransferase	O43148	RNMT	0,576	19	54,8
Mitochondrial glutamate carrier 1	Q9H936	SLC25A22	0,571	9	34,4
Protein kinase C and casein kinase substrate in neurons protein 3	Q9UKS6	PACSIN3	0,569	10	48,5
Ribosome biogenesis protein NOP53	Q9NZM5	NOP53	0,567	4	54,4
Nuclear pore membrane glycoprotein 210	Q8TEM1	NUP210	0,567	14	205
Alpha-parvin	Q9NVD7	PARVA	0,564	9	42,2
RNA-binding protein 20	Q5T481	RBM20	0,564	10	134,3
Carnitine O-palmitoyltransferase 1, liver isoform	P50416	CPT1A	0,558	3	88,3
Threonine synthase-like 1	Q8IYQ7	THNSL1	0,557	2	83
Alpha-internexin	Q16352	INA	0,555	6	55,4
Sodium bicarbonate cotransporter 3	Q9Y6M7	SLC4A7	0,555	11	136
Zinc finger and BTB domain-containing protein 7A	O95365	ZBTB7A	0,554	6	61,4
Beta-parvin	Q9HBI1	PARVB	0,549	8	41,7
Ubiquitin-like modifier-activating enzyme ATG7	O95352	ATG7	0,546	14	77,9
Ribonuclease inhibitor	P13489	RNH1	0,543	5	49,9

Table 3.3 (continued)

Protein	Accession No.	Gene Symbol	Fold-Change (L209F/WT)	Unique Peptides	MW [kDa]
60S acidic ribosomal protein P1	P05386	RPLP1	0,538	2	11,5
Mitochondrial mRNA pseudouridine synthase RPUSD3	Q6P087	RPUSD3	0,524	3	38,4
E3 ubiquitin-protein ligase RAD18	Q9NS91	RAD18	0,523	11	56,2
Kinesin-like protein KIF18A	Q8NI77	KIF18A	0,517	3	102,2
Krev interaction trapped protein 1	O00522	KRIT1	0,515	3	84,3
Glutamine and serine-rich protein 1	Q2KHR3	QSER1	0,513	7	189,9
Endonuclease/exonuclease/phosphatase family domain-containing protein 1	Q7L9B9	EEPD1	0,509	7	62,4
Very-long-chain 3-oxoacyl-CoA reductase	Q53GQ0	HSD17B12	0,509	7	34,3
Solute carrier family 35 member E1	Q96K37	SLC35E1	0,508	2	44,7
Histone-lysine N-methyltransferase SETMAR	Q53H47	SETMAR	0,505	4	78
Phosphatidylinositol 4-phosphate 3-kinase C2 domain-containing subunit alpha	O00443	PIK3C2A	0,499	27	190,6
Shootin-1	A0MZ66	SHTN1	0,49	12	71,6
LIM and senescent cell antigen-like-containing domain protein 1	P48059	LIMS1	0,482	2	37,2
Electrogenic sodium bicarbonate cotransporter 1	Q9Y6R1	SLC4A4	0,481	3	121,4
Cytosolic non-specific dipeptidase	Q96KP4	CNDP2	0,47	10	52,8
Microtubule-associated protein 1B	P46821	MAP1B	0,47	46	270,5
FSD1-like protein	Q9BXM9	FSD1L	0,457	3	59,5
Neurabin-1	Q9ULJ8	PPP1R9A	0,452	4	123,3
Inositol 1,4,5-trisphosphate receptor type 3	Q14573	ITPR3	0,448	7	303,9
Nuclear factor of activated T-cells, cytoplasmic 1	O95644	NFATC1	0,446	5	101,2
Carbonic anhydrase-related protein	P35219	CA8	0,44	4	33
Phosphatidate cytidylyltransferase, mitochondrial	Q96BW9	TAMM41	0,432	2	51
TLE family member 5	Q08117	TLE5	0,431	1	22
Mitochondrial import inner membrane translocase subunit Tim21	Q9BVV7	TIMM21	0,43	3	28,2
Neutral amino acid transporter B (0)	Q15758	SLC1A5	0,429	4	56,6
Excitatory amino acid transporter 1	P43003	SLC1A3	0,427	2	59,5
Metalloreductase STEAP3	Q658P3	STEAP3	0,408	3	54,6
DNA-binding protein SATB1	Q01826	SATB1	0,329	4	85,9
EKC/KEOPS complex subunit LAGE3	Q14657	LAGE3	0,01	2	14,8
Fibrosin-1-like protein	Q9HCM7	FBRSL1	0,01	2	110,8
Polypyrimidine tract-binding protein 3	O95758	PTBP3	0,01	2	59,7
tRNA-dihydrouridine (20) synthase [NAD(P)+]-like	Q9NX74	DUS2	0,01	2	55

A P-value ≤ 0.05 was considered with adjustment using the Benjamini–Hochberg correction for the FDR to ≤0.05. In total, 50 proteins were over-expressed and 60 under-expressed in the FLAG-TTBK2-L209F cell line.

On the DEP data, an ORA was performed with the web tool WebGestalt. The weighted set cover redundancy reduction method was included as a post-processing step, allowing to identify the most representative significant sets. For downregulated protein expression, the term “Cell-extracellular matrix interactions” (R-HSA-446353) from the Reactome was found, with an enrichment ratio of 73,957 and four associated proteins: LIM zinc finger domain containing 1 (LIMS1), integrin linked kinase (ILK), parvin beta and alpha (PARVB and PARVA) (Table 3.4). For the upregulated proteins, the terms “Developmental Biology”, “Negative regulation of RNA metabolic process”, “Circulatory system development”, “Negative regulation of gene expression”, “Negative regulation of organelle organization”, “Ameboidal-type cell migration” and “Cellular responses to stress” from Biological Process category of Gene Ontology and Reactome provided statistically significant results with enrichment ratios of 5,195, 4,0212, 4,3504, 3,2195, 7,0181, 6, 8339, and 6, 112, respectively (Table 3.4). In two enrichment sets (“Developmental Biology” and “Negative regulation of RNA metabolic process”) there was a mutual overlap of 4 proteins: mothers against decapentaplegic homolog 4 and 2 (SMAD4, SMAD2), H3 histone family 3A (H3F3A), and histone cluster 2 H3 family member c (HIST2H3C) (Table 3.4). Additionally, the “Circulatory system development” and “Negative regulation of gene expression” has also the SMAD2 and SMAD4 proteins; and “Developmental Biology” and “Cellular responses to stress” terms mutually relate to a set of 5 proteins: HIST2H3A, C and D, as well as H3F3A and B (Table 3.4). The four enrichment terms “Developmental Biology”, “Circulatory system development”, “Negative regulation of organelle organization”, and “Ameboidal-type cell migration” related to the protein Slit guidance ligand 2 (SLIT2) (Table 3.4). The two sets “Negative regulation of RNA metabolic process” and “Negative regulation of gene expression” only differ in the addition of cap binding complex dependent translation initiation factor (CTIF) to the later (Table 3.4).

Table 3.4 Functional enriched categories of the 110 DEP (+, upregulated; -, downregulated) in FLAG-TTBK2-L209F cells using the WebGestalt ORA enrichment method.

DEP	Gene Set	Description	Protein Name	Size	Expect	Ratio	P-value	FDR
+	R-HSA-1266738	Developmental Biology	PIAS2, SLIT2, KRT1, KRT10, GAP43, PFN2, KRT9, H3F3B, H3F3A, SMAD4, SMAD2, HIST2H3D, HIST2H3C, HIST2H3A, PIK3R3	1074	2,89	5,20	8,30E-08	4,41E-04
	GO: 0051253	Negative regulation of RNA metabolic process	HEXIM1, ZIC2, H3F3A, MECOM, FOXM1, SMAD4, SQSTM1, ARID5B, SMAD2, HIST2H3C, NEDD4L,	1295	3,48	4,02	5,25E-06	4,29E-03

			DHX36, MBD2, MBD1					
	GO: 0072359	Circulatory system development	SLIT2, HEXIM1, ANXA1, KRT1, SMAD4, SHB, SMAD2, AMOT, BBS7, PIK3R3, DHX36, MBD2	1026	2,76	4,35	1,31E-05	7,11E-03
	GO: 0010629	Negative regulation of gene expression	CTIF, SLIT2, HEXIM1, ANXA1, KRT1, SMAD4, SHB, SMAD2, AMOT, BBS7, PIK3R3, DHX36, MBD2	1733	4,66	3,22	3,25E-05	1,30E-02
	GO: 0010639	Negative regulation of organelle organization	MID1, SEC22B, SLIT2, PFN2, LMAN1, H3F3A, SMAD4	371	1,00	7,02	5,71E-05	2,06E-02
	GO: 0001667	Ameboidal-type cell migration	SLIT2, ANXA1, PFN2, ARID5B, AMOT, PIK3R3, AMOTL2	381	1,02	6,83	6,75E-05	2,28E-02
	R-HSA-2262752	Cellular responses to stress	H3F3B, H3F3A, TXNRD1, HIST2H3D, HIST2H3C, HIST2H3A, TNIK	426	1,15	6,11	1,35E-04	4,11E-02
-	R-HSA-446353	Cell-extracellular matrix interactions	LIMS1, ILK, PARVB, PARVA	18	0,05	73,96	2,17E-07	4,61E-03

Values were rounded to 2 decimal places. A *P*-value ≤ 0.05 was considered with adjustment using the Benjamini–Hochberg approach. The weighted set cover redundancy reduction method was included as a post-processing step. The ORA data before the processing step of redundancy reduction is presented in Annex III - Table S3.2

In addition, GSEA method was performed to obtain more relevant biological information on the FLAG-TTBK2-L209F/-WT comparison. Like ORA, only the statistically significant results are shown for a *P*-value ≤ 0.05 and a weighted set cover redundancy reduction method was integrated. For the Gene Ontology categories, was observed mainly a negative normalised enriched score (NES) of the protein sets indicating loss of functions related to gene expression (“ribosome”, “rRNA binding”, “structural constituent of ribosome”), mitochondrial activity, and biogenesis (“mitochondrial membrane part”, “mitochondrial inner membrane”, “mitochondrial matrix”, “oxidoreductase complex”, “generation of precursor metabolites and energy”) (Figure 3.11A). On the other hand, there was an increase in six sets namely “ciliary part”, “regulation of protein catabolic process”, “DNA conformation change”, “mRNA processing”, “regulation of cytoskeleton organization”, “activation of protein kinase activity”, and “regulation of mRNA metabolic process” (Figure 3.11A).

Other pathway analysis added information to the previous data by showing an increase in gene sets such as “angiogenesis”, “axon guidance”, “estrogen-dependent expression”, “mitotic prophase”,

“regulation of actin cytoskeleton”, “cellular senescence”, “alcoholism” and “histone modifications” (Figure 3.11B). Once more, negative NES values were observed for gene expression related sets (“metabolism of RNA”, “cytoplasmatic ribosomal proteins”, “RNA transport”, “basal transcription factors”, “ribosome”), however with the addition of “metabolism” and “translation” sets (Figure 3.11B). In the Disgenet and GLAD4U databases, we observed a decrease in the gene sets of increased serum lactate and mitochondrial diseases. Also, a decrease in PD and AD (-2,4787 and -2,2392, respectively) contrasted with an increase in Joubert syndrome and melanoma (2,3527 and 2,1821, respectively) sets was observed (Figure 3.11B and C; Annex III - Table S3.3).

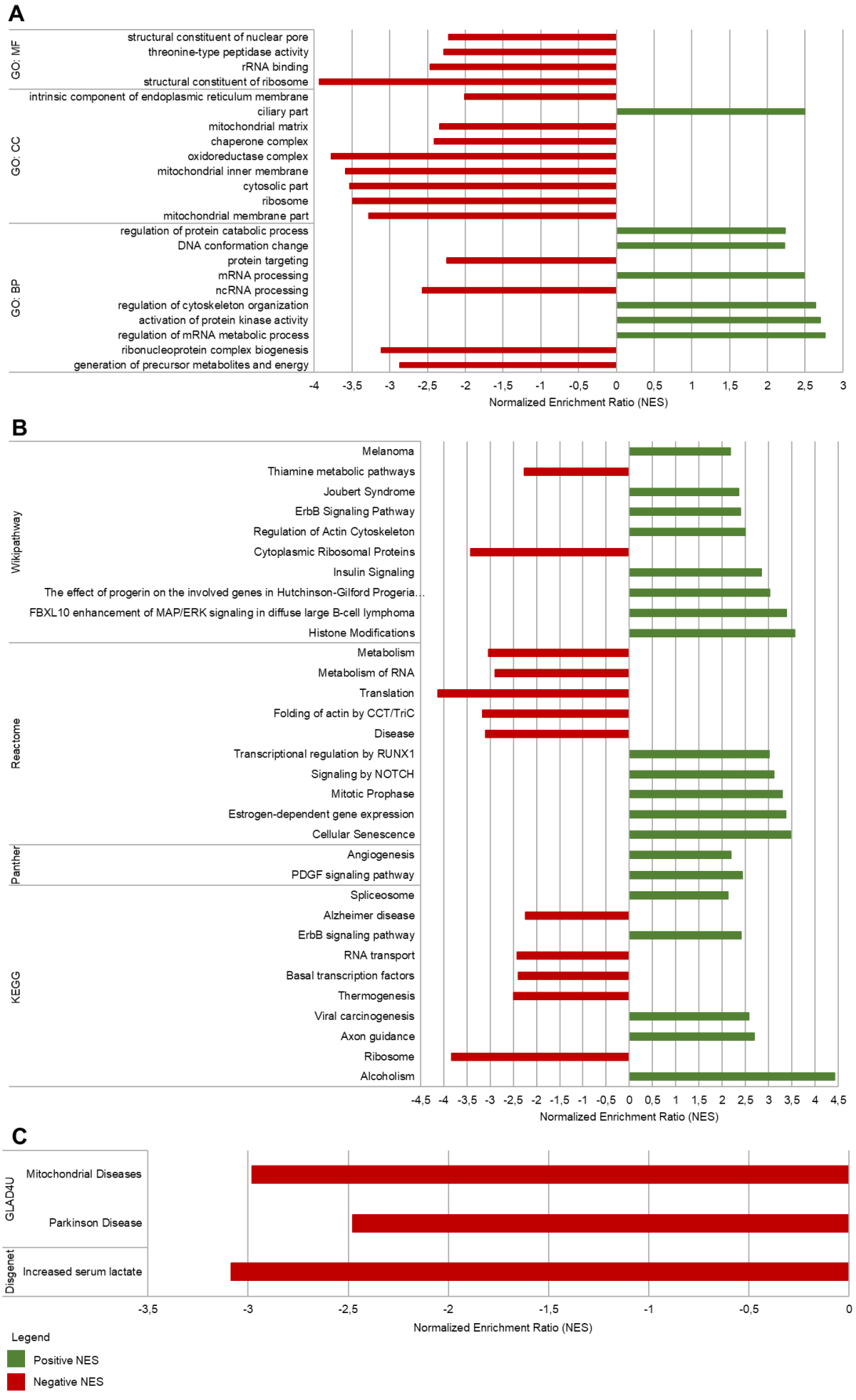
A
GO: MF
structural constituent of nuclear pore
threonine-type peptidase activity
rRNA binding
structural constituent of ribosome
GO: CC
intrinsic component of endoplasmic reticulum membrane
ciliary part
mitochondrial matrix
chaperone complex
oxidoreductase complex
mitochondrial inner membrane
cytosolic part
ribosome
mitochondrial membrane part
GO: BP
regulation of protein catabolic process
DNA conformation change
protein targeting
mRNA processing
ncRNA processing
regulation of cytoskeleton organization
activation of protein kinase activity
regulation of mRNA metabolic process
ribonucleoprotein complex biogenesis
generation of precursor metabolites and energy
-4 -3,5 -3 -2,5 -2 -1,5 -1 -0,5 0 0,5 1 1,5 2 2,5 3
Normalized Enrichment Ratio (NES)
B
Wikipathway
Melanoma
Thiamine metabolic pathways
Joubert Syndrome
ErbB Signaling Pathway
Regulation of Actin Cytoskeleton
Cytoplasmic Ribosomal Proteins
Insulin Signaling
The effect of progerin on the involved genes in Hutchinson-Gilford Progeria...
FBXL10 enhancement of MAP/ERK signaling in diffuse large B-cell lymphoma
Histone Modifications
Reactome
Metabolism
Metabolism of RNA
Translation
Folding of actin by CCT/TriC
Disease
Transcriptional regulation by RUNX1
Signaling by NOTCH
Mitotic Prophase
Estrogen-dependent gene expression
Cellular Senescence
Panther
Angiogenesis
PDGF signaling pathway
KEGG
Spliceosome
Alzheimer disease
ErbB signaling pathway
RNA transport
Basal transcription factors
Thermogenesis
Viral carcinogenesis
Axon guidance
Ribosome
Alcoholism
-4,5 -4 -3,5 -3 -2,5 -2 -1,5 -1 -0,5 0 0,5 1 1,5 2 2,5 3 3,5 4 4,5
Normalized Enrichment Ratio (NES)
C
GLAD4U
Mitochondrial Diseases
Parkinson Disease
Disgenet
Increased serum lactate
-3,5 -3 -2,5 -2 -1,5 -1 -0,5 0
Normalized Enrichment Ratio (NES)
Legend
Positive NES
Negative NES

Figure 3.11 Functional enrichment analysis using WebGestalt GSEA enrichment approach. A *P*-value ≤ 0.05 was considered with adjustment using the Benjamini–Hochberg approach. The (A) Gene Ontology (GO) categories: Biological Process (BP), Cellular Component (CC) and Molecular Function (MF); (B) Pathway databases: KEGG, Panther, Reactome and Wikipathway; and (C) Disease functional databases: Disgenet and GLAD4U, were considered. The weighted set cover redundancy reduction method was included as a post-processing step. The upregulated pathways are depicted in green, and the downregulated proteins are displayed in red, based on NES. The GSEA information before the processing step of redundancy reduction is presented in Annex III - Table S3.3. Due to the extent of the GSEA enrichment data, the complete set of enriched proteins can be seen in https://drive.google.com/file/d/1bQumR96QB5H0y6e7oCoNu6nALWnxXfv0/view?usp=sharing.

Furthermore, on this analysis were identified 18 phosphorylation sites of 10 differentially expressed proteins (Figure 3.10, Table 3.5). An annotation of the phosphorylated residues in databases such as PhosphositePlus and PhosphoELM allowed to discover that more than a half of the 18 residues have been confirmed in mammals' studies. *In vitro* upstream kinases had been described for SQSTM1/P62 (Ser272), SMAD2 (Thr8) and NEDD4L (Ser448): cyclin-dependent kinase 1 (CDK1)/ MAPK13, MAPK3, and protein kinase A catalytic subunit alpha (PKACα)/ serum/glucocorticoid regulated kinase 1 (SGK1), respectively. For the other residues, there are no known kinases or regulatory proteins identified yet.

Table 3.5 List of phosphorylated sites identified in FLAG-TTBK2-L209F DEP.

	Protein	Accession No.	Phosphorylation Site	State	PMID
+	p62/ SQSTM1	Q13501	Ser272: LTPVsPESSSTEEK	Confirmed in mammals	16565220
	SMAD2	Q15796	Thr8: mSSILPFtPPVVK	Confirmed in mammals	12193595
	AMOT	Q4VCS5	Ser200: AHPPVTSAPLsPPQPNDLYK	Predicted by Kinexus P-Site Prediction algorithm	
			Ser309: NSQPHsPTSSLTSGGSLPLLQSPPSTR	Confirmed in mammals	27869121
			Ser332: NSQPHSPtSSLTSGGSLPLLQSPPSTRLsPAR	Predicted by Kinexus P-Site Prediction algorithm	
			Ser714: DTTVISHsPNTSYDTALEAR	Confirmed in mammals	18452278
			Ser808: SLMSISnAGSGLLSHSSTLTGsPIMEEK	Predicted by Kinexus P-Site Prediction algorithm	
			Thr1061: TDGPVFHSNtLER	Confirmed in mammals	17287340
	CTIF	O43310	Ser299: LEDTAGDTGHSSLEAPRsPDTLAPVASER	Confirmed in mammals	18088087; 19664994
	NEDD4L	Q96PU5	Ser448: SLsSPTVTLSAPLEGAK	Confirmed in mammals	16716084
	HTATSF1	O43719	Ser498: ESEEGNPVRGSEEDsPKK	Confirmed in mammals	17287340
			Ser642: VFDDEsDEKEDEEYADEK	Confirmed in mammals	15302935
			Ser676: LFEEsDDKEDEDADGKEVEDADEK	Confirmed in mammals	15302935

	TNIK	Q9UKE5	Ser640: QNsDPTSENPPLPTR	Confirmed in mammals	18691976
	IRS4	O14654	Ser757: VsPPPAPsPPKAPDT	Predicted by Kinexus P-Site Prediction algorithm	
-	BAG3	O95817	Ser173: SQsPAASDCSSSSSSASLPSSGR	Confirmed in mammals	15302935
	RBM20	Q5T481	Ser742: SGsPNLPHSVSSYK	Confirmed in mammals	19276368
			Ser1048: GVESSDVHPAPTVQQMSsPKPAEER	Predicted by Kinexus P-Site Prediction algorithm	

PMID: PubMed reference number. The phosphorylated residues are represented in red lowercase letters.

4
DISCUSSION

In this work, functional studies were performed in a cellular model genetically modified by CRISPR/Cas9 with a novel missense variant in *TTBK2* (c.625C>T; p.Leu209Phe), which was identified in two Portuguese siblings affected with cerebellar ataxia. HEK293T cell line is easy to handle and grow, and allows a high transfection efficiency, which are critical features to CRISPR/Cas9 genetic editing[150]. Moreover, these cells are an interesting model for neuroscience-related studies as they derived from neuronal precursor cells in the embryonic kidney and expresses neuronal specific genes[150,151]. In addition, these cells can form PC under medium starved conditions, which allows to study TTBK2 role in ciliogenesis and its relation to cerebellar ataxia[152]. Unfortunately, we were not able to create a heterozygous cell line expressing the TTBK2 c.625C>T variant. Indeed, it has been reported that the insertion of knock-in mutations at single alleles (to create heterozygous cell models) by CRISPR/Cas9 has low efficiency[153]. Despite that, our homozygous model allowed us to study the impact of the novel variant in TTBK2 cellular and molecular functions, which was the main goal of this work. Furthermore, our results demonstrated for the first time an association between a *TTBK2* missense variant and a loss-of-function effect, linked to alterations in cytoskeleton, protein phosphorylation and autophagy.

The decreased levels of FLAG-TTBK2-L209F variant are not the result of reduction or instability of the mRNA, as previously reported for truncating variants[29], but may result instead from decreased protein stability (Figure 3.3), which is also supported by *in silico* predictions (Table 3.2, Figure 3.2). The low protein expression of this variant supports the reported theory of loss-of-function[29], but the mechanism responsible for the degradation of FLAG-TTBK2-L209F remains unclear. The treatment of cells with inhibitors of the proteasome (MG132), autophagy (chloroquine and NH_4Cl) and endoplasmic reticulum-associated degradation (ERAD and Eer1) did not allow to visualize an increase in FLAG-TTBK2-L209F protein levels by immunoblotting (data not shown). Another possible pathway that may be affecting FLAG-TTBK2-L209F protein levels is the chaperone-mediated autophagy (CMA) which function as a backup mechanism when autophagy is impaired and was previously described to participate in PD, AD, and ALS[154,155]. In CMA, the heat shock cognate 71 kDa protein (HSC70) chaperone recognizes a KFERQ sequence and deliver the cargo to the LAMP2A complex at the lysosome[154]. Therefore, it would be relevant to identify a KFERQ-consensus sequence in TTBK2 protein, and study CMA in FLAG-TTBK2-L209F cells via RT-qPCR and immunoblotting of markers such as HSC70 and LAMP2A[156].

The analysis on TTBK2 subcellular localization (Figure 3.4B) supported the previous findings[46,55,56], demonstrating a primary location in the cytoplasm (Figure 3.4A and B). At the same time, TTBK2 seemed to be present in the cytoskeletal fraction (Figure 3.4B) with a higher molecular weight that may be caused by post-translational modifications (PTMs) or protein charge changes. One hypothesis is the phosphorylation-dependent electrophoretic mobility shift[157,158], as TTBK2 can be phosphorylated by other proteins (e.g., TTBK1) or itself[41,159]. Still, there is a need for further investigate the presence of PTMs in TTBK2 through assays like phospho-tag and mass spectrometry[158]. Nevertheless, it was not observed a major dislocation of TTBK2 to the nucleus as in truncating variants[36], demonstrating that the missense variant does not cause abnormalities in the subcellular distribution of TTBK2. Thus, its presence in the microtubules[41,48] or cilia[46,62,63] seems to not be affected, in agreement with the previous reports that TTBK2 interacts with microtubules and CEP164 through the SxIP motifs independently of the kinase activity[41,63]. Still, the kinase activity needs to be fully assessed as TTBK2 phosphorylate microtubules and cilia associated proteins like tau, KIF2A, CEP164, among another[42,43,48,62,63], and this process is essential for ciliogenesis initiation[46,71]. Therefore, later, it would be interesting to analyze ciliogenesis alterations in FLAG-TTBK2-L209F cells.

The kinesin KIF2A is a target of TTBK2 phosphorylation at Ser135 through the interaction with EB1 at the microtubule ends, inhibiting KIF2A interaction with the microtubules and consequently decreasing its depolymerizing activity[41,48]. KIF2A protein expression is decreased (Figure 3.5) in FLAG-TTBK2-L209F cells, being rescued by EGFP-TTBK2-WT overexpression (Figure 3.6). This scenario may indicate that TTBK2 is essential for the proper maintenance of cytoskeleton and KIF2A. One hypothesis is the regulation of KIF2A levels by phosphorylation, but KIF2A was not detected in our phosphoproteome analysis, and we cannot take conclusions. However, KIF18A, also a microtubule depolymerase that is essential for mitotic progression[160], appear as a downregulated protein (Table 3.3, ratio = 0,517) in the phophoenrichment data. Additionally, it would be relevant to perform co-immunoprecipitation experiments to analyse changes in protein interaction between TTBK2 and KIF2A in the presence of the Leu209Phe variant. The decrease in KIF2A protein levels may affect the microtubules dynamics, disturbing neuronal morphogenesis, proliferation, and migration during brain development[161–163], as well as the regulation of the cell cycle and ciliogenesis[164,165]. The full understanding of the KIF2A-TTBK2 regulation and its influence on microtubules dynamics still needs to be explored.

Our results also demonstrated a reduction in α–tubulin acetylation in FLAG-TTBK2-L209F cells (Figure 3.5). The decrease in TTBK2 protein levels may lead to microtubule's dynamic instability, resulting in reduced α–tubulin acetylation[166] because TTBK2 might regulate microtubule assembly functioning as a +TIP (group of MAPs) and kinase of β-tubulin (part of microtubule's α/β-tubulin heterodimers) and/or MAPs[41–43,167]. Besides that, it is known that some kinases may function as MAPs in a kinase-independent manner, influencing microtubule dynamics and stability[168,169]. Another possibility is that TTBK2 may regulate α–tubulin acetylation through the stabilization of α-tubulin acetyltransferase 1 (αTAT1) or histone deacetylase 6/sirtuin 2 (HDAC6/SIRT2)[170]. The α–tubulin acetylation is crucial for axonal vesicular trafficking[171], neuronal dendritic branches growth and migration during development[172,173]. Therefore, deficits on α–tubulin acetylation cause an altered pattern of MAPs, leading to

axonal transport impairment, abnormal polarization, and migration in neurons[174]. The axonal transport defects are a common feature of neurodevelopmental and neurodegenerative disorders[174]. The increase in microtubules acetylation rescued the axonal transport and locomotor deficits in HD and PD, respectively, reverted axonal loss in Charcot-Marie-Tooth disease, and improves memory in a tau deposition context[174]. These studies reveal the HDAC inhibitors as a promising therapeutic target in neurodegenerative diseases. The effect of HDAC inhibitors can also be evaluated in FLAG-TTK2-L209F cells in future studies. Moreover, the microtubules acetylation is also intrinsically associated with the cell cycle[175] and α–tubulin acetylation alterations can cause abnormalities in cell division. Thus, it would be interesting to study the cell cycle by flow cytometry of FLAG-TTBK2-L209F cells. Also, the acetylation of α–tubulin is required for autophagosome formation and their fusion with lysosomes[176], which can somehow alter autophagy in FLAG-TTBK2-L209F cells.

The association of autophagy impairment with neurodegeneration also seems to be observed in SCA11[148]. In FLAG-TTBK2-L209F cells, it was seen an increase in p62 protein levels comparing to FLAG-TTBK2–WT cells (Figure 3.7B, 3.8A), which suggests an impairment in the autophagic flux because p62 itself is degraded by autophagy[177]. However, the turnover of LC3B-I/-II seems to indicate a normal autophagic flux in FLAG-TTBK2-L209F cells (Figure 3.8A). Interestingly, we also detected an increase in the protein expression of upstream autophagy proteins like Raptor, ULK1 and Beclin 1, which were all found to be phosphorylated (activated forms) in FLAG-TTBK2-L209F; but no phosphorylation differences were found between FLAG-TTBK2-WT and –L209F cells (Figure 3.7). Still, the increase in these active autophagy players may alter their downstream targets and alter the autophagic process in FLAG-TTBK2-L209F cells[148]. Further work is needed to understand and to confirm these results.

If the increase of these proteins levels is due to increased transcription and/or protein accumulation (e.g., in inclusions) remains to be evaluated. The kelch-like ECH-associated protein 1/nuclear factor (erythroid-derived 2)-like 2 (Keap1/Nrf2) pathway is a major cellular defense mechanism associated with neurodegenerative diseases that may explain this upregulation of autophagic proteins[178]. Under non-stressed conditions, the transcription factor Nrf2 is constitutively degraded via the ubiquitin-proteosome pathway due to the interaction with Keap1, an adaptor of the ubiquitin ligase complex[178,179]. However, in oxidative and protein stress (UPS deficiency) situations, the p62 inclusions sequesters Keap1 and stabilizes Nrf2 leading to the transcription of genes containing ARE (antioxidant response element) domains, like *ULK1*, *p62* and autophagy related 7 (*atg7*), creating a positive-feedback loop[179]. Besides that, an increase in p62 (Table 3.3, ratio = 1,717) phosphorylated at Ser272 was observed in FLAG-TTBK2-L209F cells (Table 3.5). This PTM was reported to regulate p62 protein degradation, provoking an inhibition of autophagy[180,181], control the cell cycle through CDK1[182] and activate transforming growth factor beta-activated kinase 1 (TAK1) signalling platform[180]. Therefore, it is important to evaluate autophagy markers gene expression, p62 phosphorylation (Ser272) and its co-localization with Keap1 by RT-qPCR, immunoblotting and immunofluorescence, respectively.

Furthermore, LAMP1 (glycosylated) levels were decreased in FLAG-TTBK2-L209F cells. There are several studies showing alteration in lysosomes and autophagy in neurodegenerative diseases, includ-

ing cerebellar ataxias[149] . Whether LAMP1 reduced levels correlate with a reduced number of lysosomes, or abnormalities in lysosomes, is still unknown but our results indicate that it would be pertinent to analyse it. In FTD, an abnormal LAMP1 immunostaining indicated that protein degradation through autolysosomes might be altered[183,184]. Thus, it would be relevant to analyse if p62 accumulates with LAMP1 in the lysosomes and/or with LC3B in the autophagosomes by immunofluorescence.

Additionally, it is important to understand the impact of the Leu209Phe variant in the kinase activity of TTBK2 *in vitro* by analysing the phosphorylation state of its substrates. In ALS models, TTBK2 was found to phosphorylate the DNA/RNA binding protein TDP-43 at Ser409/410, where a hyperphosphorylated state promotes a cytoplasmic re-localization and protein aggregation that may be the key mechanism behind TDP-43 neurotoxicity[52]. In FLAG-TTBK2-L209F cells it was observed a decrease in TDP-43 phosphorylation at Ser409/410 (Figure 3.5A), which demonstrated a loss-of-function mechanism. Moreover, overexpression of EGFP-TTBK2-WT increased Ser409/410 of TDP-43 phosphorylation levels, while EGFP-TTBK2-L209F overexpression did not alter the phosphorylation state of TDP-43 (Figure 3.5A and B).

TDP-43 is essential for the autophagosome formation, as it stabilizes the mRNAs of the autophagy proteins atg7, raptor and dynactin 1[185,186]. TDP-43 phosphorylation at Ser409/410 leads to the dislocation of TDP-43 to the cytoplasm, blocks autophagosome-lysosome fusion and enhance LC3-II and p62 levels by inhibiting the activity of mammalian target of rapamycin (mTOR) and expression of dynactin 1[187]. In the future, it would be important to understand the consequences behind the lack of TDP-43 phosphorylation and dislocation to the cytoplasm, and its effect on the regulation of autophagy atg7, raptor and dynactin 1 mRNAs[187]. Note that TDP-43 autoregulates its own mRNA and there were not observed changes in its total expression levels (Figure 3.5A and B), but in FTLD brain samples it was observed an increase in TDP-43 mRNA levels[188]. Nevertheless, TDP-43 gene expression should be evaluated by RT-qPCR, as well as its localization in FLAG-TTBK2-L209F cells by immunofluorescence.

A mass spectrometry-based proteomics study was performed to explore differential phosphoproteins levels between FLAG-TTBK2-L209F cells and -WT control cells. The GSEA analysis (weighted set cover redundancy reduction) showed that the most relevant pathways enriched in FLAG-TTBK2-L209F cells were “Alcoholism” (hsa05034), "Histone Modifications" (WP2369) and "Cellular Senescence" (R-HAS-2559583), with the NES of 4,4201, 3,5679 and 3,4784, respectively (Figure 3.11B, Annex III - Table S3.3). Among these enriched pathways, it was present several members of the histone cluster 1 H3 family (a, b, c, d, e, f, g, h, i and j) and H4 family (a, b, c, d, e, f, h, i, j, k and l) as well as other histone clusters (Annex III - Table S3.3, https://drive.google.com/file/d/1bQumR96QB5H0y6e7oCoNu6nALWnxXfv0/view?usp=sharing). The H3 and H4 histones are core components of the nucleosome that regulates DNA accessibility, replication, and repair[189]. PTMs on H3 and H4 histones such as phosphorylation, acetylation and methylation are associated with mitosis and gene expression regulation[189]. In addition, the redundant data (Annex III - Table S3.3) showed an enrichment in FLAG-TTBK2-L209F cells of pathways related to transcription

regulation (e.g., “RNA Polymerase I Chain elongation”, “RNA Polymerase I Transcription”, “RNA Polymerase II Transcription” and “Gene Silencing by RNA” from Reactome). Therefore, this data highlights the role of gene dysregulation in NDDs[190] .

Moreover, FLAG-TTBK2-L209F cells were found to be less enriched in phosphoproteins involved in “Translation” (R-HSA-72766) and “Ribosome” (hsa03010) pathways with a NES of -4,1307 and -3,8302, respectively (Figure 3.11B, Annex III - Table S3.3). This data agrees with the developing notion of translational repression and ribosome dysfunction, caused by UPR and oxidative stress, in NDDs[191]. Interestingly, some mitochondrial activity related pathways such as “mitochondrial membrane part”, “mitochondrial inner membrane”, “mitochondrial matrix”, “oxidoreductase complex”, and “generation of precursor metabolites and energy” (Figure 3.11B, Annex III - Table S3.3) with the NES of -3,2805, -3,5869, -2,3361, -3,7770, and -2,8683, respectively, also appeared less enriched in FLAG-TTBK2-L209F cells. This could be indirectly caused by the dysfunction of gene expression regulation and oxidative stress[8].

In the ORA data, it was found seven upregulated pathways in FLAG-TTBK2-L209F cells related to embryonic development (“Developmental Biology”, “Circulatory system development” and “Ameboidal-type cell migration”), negative transcriptional regulation (“Negative regulation of RNA metabolic process” and “Negative regulation of gene expression”), “Negative regulation of organelle organization”, and “Cellular responses to stress” (Table 3.4). Interestingly, more than a half of the enriched sets (“Developmental Biology”, “Negative regulation of RNA metabolic process”, “Circulatory system development” and “Negative regulation of gene expression”) had an overlap of the proteins SMAD4 and SMAD2 (Table 3.4). Moreover, we identified the Thr8 phosphorylation in SMAD2 protein (Table 3.3 and 3.5, ratio = 1,688). The MAPK3 phosphorylation was associated with activity induction and enhanced transcription of an activin/transforming growth factor beta (TGF-β)-responsive DNA element due to SMAD2 increased levels (protein stabilization/increased half-life) that provokes an increase in the formation of complexes with SMAD4[192]. On the other hand, calmodulin negatively regulates SMAD2 by inhibiting MAPK phosphorylation and decreasing its levels[192]. The TGF-β activin regulates several aspects of neuronal development, morphology, and function[193]. These two upregulated proteins (SMAD2 and SMAD4) should be studied in the future to better understand their role in the pathogenesis of SCA11.

Additionally, we identified the downregulated pathway "Cell-extracellular matrix interactions” (R-HSA-446353), which includes the PINCH–ILK–parvin (PIP) complexes that regulate integrins and the actin cytoskeleton, functioning as signaling transducers of several pathways[194,195]. Moreover, PIP related proteins have been reported to regulate cells morphology, migration, and proliferation, as well as neuron outgrowth[194,195]. ILK depletion showed increased in GSK3β activity, tau hyper-phosphorylation and reduced neurite extension and actin reorganization, and LIM proteins were involved in AD neuronal dysfunction and tau phosphorylation[195].

Finally, by analysing the mass spectrometry data, we identified the phosphorylated Ser448 in the neuronal precursor cell expressed developmentally downregulated 4-like (NEDD4-2/NEDD4L) (Table 3.3 and 3.5, ratio = 1,772). This protein is an E2 ubiquitin ligase crucial to correctly regulate the channel degradation and maintain neuronal excitability[196]. Previously, Ser448 phosphorylation was associated with enhanced ubiquitination of NEDD4L and consequent increased neuronal excitability[196] . In overall,

the phosphoproteome analysis provided us relevant data that will help to unravel the molecular pathways underlying SCA11 (caused by the Leu209Phe variant).

5

CONCLUSIONS AND PERSPECTIVES

Since the *TTBK2* gene was linked to SCA11 several studies have been made to understand the impact of the variants as well as discover its molecular functions. However, the mechanisms underlying SCA11 and TTBK2 loss-of-function are far from being completely understood.

In this study, for the first time, a *TTBK2* missense variant was associated with a loss-of-function effect, and alterations in cytoskeleton, protein phosphorylation and autophagy. The changes in these pathways may consequently provoke defects in axonal transport, neuronal morphogenesis and migration, which are common features of neurodegenerative diseases.

The *TTBK2* (c.625C>T; p.Leu209Phe) variant affected TTBK2 protein expression, possibly by impacting protein stability as there were not changes in gene expression. Still, the search for the mechanism responsible for TTBK2 protein degradation needs to be addressed. KIF2A and acetylated α–tubulin decreased levels in FLAG-TTBK2-L209F cells indicate that TTBK2 is probably essential to the regulation of microtubule dynamics. But it is unknown if TTBK2 regulates KIF2A and α–tubulin acetylation levels by phosphorylation, or if it is an indirect effect. Also, FLAG-TTBK2-L209F cells showed alterations in autophagy markers Raptor, ULK1, Beclin 1 and p62 that may be provoked by a positive-feedback-loop and/or sequestering in cytoplasmic inclusions. Furthermore, the increase in p62 (Ser272) phosphorylation shows that autophagy may be inhibited. The TTBK2 Leu209Phe kinase activity was proven to be impaired since phosphorylated (Ser409/410) TDP-43 was decreased in the FLAG-TTBK2-L209F cells, but the effects of this are unknown. Additionally, the phosphoproteome results point to a gene expression and mitochondrial dysregulation, translational repression, and cytoskeleton changes, as well as indicate two enriched proteins (SMAD2 and SMAD4) involved in the TGF-β pathway that may play a role in SCA11 pathogenesis.

Future studies with this cellular model should be done to further understand the mechanism behind the autophagy alterations, and the consequences of TDP-43 phosphorylation deficit and its effect on the transcriptional regulation/mRNA stabilization. TTBK2 influence in cytoskeleton dynamics and mitosis should be explored as TTBK2 may interact with other cytoskeletal proteins involved in microtubule stabilization, such as αTAT1, HDACs and MAPs. Also, an exploratory study on the obtained DEP, especially the SMAD2 and SMAD4, may increase the knowledge on the affected mechanisms in SCA11.

Furthermore, the development of cellular models to study the impact of TTBK2 variants in neurodegenerative related mechanisms, will contribute to a better understanding of SCA pathological processes as well as the development of new strategies, enabling the recovery or improvement of the deleterious effects caused by TTBK2 loss-of-function.

BIBLIOGRAPHY

1. Matilla-Dueñas, A. *et al.* Rare neurodegenerative diseases: Clinical and genetic update. in *Advances in Experimental Medicine and Biology* vol. 1031 443–496 (Springer New York LLC, 2017).
2. Seidel, K. *et al.* Brain pathology of spinocerebellar ataxias. *Acta Neuropathologica* vol. 124 1–21 (2012).
3. Gomez, J. & Jin, D. Acute cerebellar ataxia associated with modest elevation of anti-GAD antibodies in a young patient. *Tremor and Other Hyperkinetic Movements* **8**, 1–3 (2018).
4. Klockgether, T. & Paulson, H. Milestones in Ataxia. *Movement Disorders* **26**, 1134–1141 (2011).
5. Goldman, J. G. Ataxia. in *Encyclopedia of Movement Disorders* 70–86 (Elsevier Inc., 2010). doi:10.1016/B978-0-12-374105-9.00153-2.
6. Robinson, K. J., Watchon, M. & Laird, A. S. Aberrant Cerebellar Circuitry in the Spinocerebellar Ataxias. *Frontiers in Neuroscience* **14**, 1–27 (2020).
7. Siegel, A. & Sapru, H. N. *Essential Neuroscience, 2nd edition*. (2011).
8. Klockgether, T., Mariotti, C. & Paulson, H. L. Spinocerebellar ataxia. *Nature Reviews Disease Primers* **5**, 1–21 (2019).
9. Durr, A. Autosomal dominant cerebellar ataxias: Polyglutamine expansions and beyond. *The Lancet Neurology* **9**, 885–894 (2010).
10. Ruano, L., Melo, C., Silva, M. C. & Coutinho, P. The global epidemiology of hereditary ataxia and spastic paraplegia: A systematic review of prevalence studies. *Neuroepidemiology* **42**, 174–183 (2014).
11. Paulson, H. L. The spinocerebellar ataxias. *Journal of Neuro-Ophthalmology* **29**, 227–237 (2009).
12. Jen, J. C. & Wan, J. Episodic ataxias. in *Handbook of Clinical Neurology* vol. 155 205–215 (Elsevier B.V., 2018).
13. Fogel, B. L. Autosomal-recessive cerebellar ataxias. in *Handbook of Clinical Neurology* vol. 147 187–209 (Elsevier B.V., 2018).
14. Palau, F. & Espinós, C. Autosomal recessive cerebellar ataxias. *Orphanet Journal of Rare Diseases* **1**, 1–19 (2006).
15. Beaudin, M. *et al.* The Classification of Autosomal Recessive Cerebellar Ataxias: a Consensus Statement from the Society for Research on the Cerebellum and Ataxias Task Force. *Cerebellum* **18**, 1098–1125 (2019).
16. Zanni, G. & Bertini, E. X-linked ataxias. in *Handbook of Clinical Neurology* vol. 155 175–189 (Elsevier B.V., 2018).
17. Hunter, J. *et al.* Epidemiology of fragile X syndrome: A systematic review and meta-analysis. *American Journal of Medical Genetics, Part A* **9999**, 1–11 (2014).
18. Vernon, H. J. & Bindoff, L. A. Mitochondrial ataxias. in *Handbook of Clinical Neurology* vol. 155 129–141 (Elsevier B.V., 2018).
19. Gorman, G. S. *et al.* Mitochondrial diseases. *Nature Reviews Disease Primers* **2**, 1–22 (2016).
20. Vanacore, N. *et al.* Epidemiology of multiple system atrophy. *Neurol Sci* **22**, 97–99 (2001).
21. Schöls, L., Bauer, P., Schmidt, T., Schulte, T. & Riess, O. Autosomal dominant cerebellar ataxias: clinical features, genetics, and pathogenesis. *Lancet Neurol* **3**, 291–304 (2004).

22. Jones, T. M., Shaw, J. D., Sullivan, K. & Zesiewicz, T. A. Treatment of cerebellar ataxia. *Neurodegenerative disease management* **4**, 379–392 (2014).
23. Sullivan, R., Yau, W. Y., O'Connor, E. & Houlden, H. Spinocerebellar ataxia: an update. *Journal of Neurology* **266**, 533–544 (2019).
24. Matilla-Dueñas, A. *et al.* Consensus paper: Pathological mechanisms underlying neurodegeneration in spinocerebellar ataxias. *Cerebellum* **13**, 269–302 (2014).
25. Huang, M. & Verbeek, D. S. Why do so many genetic insults lead to Purkinje Cell degeneration and spinocerebellar ataxia? *Neuroscience Letters* 1–9 (2019) doi:10.1016/j.neulet.2018.02.004.
26. Jones, L., Houlden, H. & Tabrizi, S. J. DNA repair in the trinucleotide repeat disorders. *The Lancet Neurology* **16**, 88–96 (2017).
27. Bauer, P. O. & Nukina, N. The pathogenic mechanisms of polyglutamine diseases and current therapeutic strategies. *Journal of Neurochemistry* **110**, 1737–1765 (2009).
28. Hetz, C. & Mollereau, B. Disturbance of endoplasmic reticulum proteostasis in neurodegenerative diseases. *Nature Reviews Neuroscience* **15**, 233–249 (2014).
29. Houlden, H. *et al.* Mutations in TTBK2, encoding a kinase implicated in tau phosphorylation, segregate with spinocerebellar ataxia type 11. *Nature Genetics* **39**, 1434–1436 (2007).
30. Worth, P. F. *et al.* Autosomal Dominant Cerebellar Ataxia Type III: Linkage in a Large British Family to a 7.6-cM Region on Chromosome 15q14-21.3. *Am. J. Hum. Genet* **65**, 420–426 (1999).
31. Lindquist, S. G. *et al.* A Novel TTBK2 De Novo Mutation in a Danish Family with Early-Onset Spinocerebellar Ataxia. *Cerebellum* **16**, 268–271 (2017).
32. Deng, Y., Fu, J., Zhong, Y. Q., Zhang, M. & Qi, X. First finding of familial spinal cerebellar Ataxia11 in China: clinical, imaging and genetic features. *Neurological Sciences* **41**, 155–160 (2020).
33. Bauer, P. *et al.* Spinocerebellar ataxia type 11 (SCA11) is an uncommon cause of dominant ataxia among French and German kindreds. *Journal of Neurology, Neurosurgery and Psychiatry* **81**, 1229–1232 (2010).
34. Németh, A. H. *et al.* Next generation sequencing for molecular diagnosis of neurological disorders using ataxias as a model. *Brain* **136**, 3106–3118 (2013).
35. Galatolo, D. *et al.* Ngs in hereditary ataxia: When rare becomes frequent. *International Journal of Molecular Sciences* **22**, 1–23 (2021).
36. Bouskila, M. *et al.* TTBK2 kinase substrate specificity and the impact of spinocerebellar- ataxia-causing mutations on expression, activity, localization and development. *Biochemical Journal* **437**, 157–167 (2011).
37. Šimić, G. *et al.* Tau protein hyperphosphorylation and aggregation in alzheimer's disease and other tauopathies, and possible neuroprotective strategies. *Biomolecules* vol. 6 2–28 (2016).
38. Giunti, P. *et al.* Spinocerebellar ataxia type 11. in *Handbook of Clinical Neurology* vol. 103 521–534 (Elsevier B.V., 2012).
39. Ikezu, S. & Ikezu, T. Tau-tubulin kinase. *Frontiers in Molecular Neuroscience* **7**, (2014).
40. Sato, S., Cerny, R. L., Buescher, J. L. & Ikezu, T. Tau-tubulin kinase 1 (TTBK1), a neuron-specific tau kinase candidate, is involved in tau phosphorylation and aggregation. *Journal of Neurochemistry* **98**, 1573–1584 (2006).
41. Jiang, K. *et al.* A proteome-wide screen for mammalian SxIP motif-containing microtubule plus-end tracking proteins. *Current Biology* **22**, 1800–1807 (2012).
42. Takahashi, M. *et al.* Involvement of T Protein Kinase I in Paired Helical Filament-Like Phosphorylation of the Juvenile T in Rat Brain. *J. Neurochem* **64**, 1759–1768 (1995).
43. Tomizawa, K., Omori, A., Ohtake, A., Sato, K. & Takahashi, M. Tau-tubulin kinase phosphorylates tau at Ser-208 and Ser-210, sites found in paired helical filament-tau. *FEBS Letters* **492**, 221–227 (2001).
44. Kitano-Takahashi, M. *et al.* Expression, purification and crystallization of a human tau-tubulin kinase 2 that phosphorylates tau protein. *Acta Crystallographica Section F: Structural Biology and Crystallization Communications* **63**, 602–604 (2007).
45. Evangelista, M. *et al.* Kinome siRNA screen identifies regulators of ciliogenesis and hedgehog signal transduction. *Science Signaling* **1**, (2008).
46. Goetz, S. C., Liem, K. F. & Anderson, K. v. The spinocerebellar ataxia-associated gene tau tubulin kinase 2 controls the initiation of ciliogenesis. *Cell* **151**, 847–858 (2012).
47. Goetz, S. C. & Anderson, K. v. The primary cilium: A signalling centre during vertebrate development. *Nature Reviews Genetics* **11**, 331–344 (2010).

48. Watanabe, T. *et al.* TTBK2 with EB1/3 regulates microtubule dynamics in migrating cells through KIF2A phosphorylation. *Journal of Cell Biology* **210**, 737–751 (2015).
49. Almilaji, A., Munoz, C., Hosseinzadeh, Z. & Lang, F. Upregulation of Na,Cl - -coupled betaine/γ-amino-butyric acid transporter BGT1 by tau tubulin kinase 2. *Cellular Physiology and Biochemistry* **32**, 334–343 (2013).
50. Alesutan, I. *et al.* Upregulation of Na+-coupled Glucose transporter SGLUT1 bu Tau Tubulin Kinase 2. *Cellular Physiology and Biochemistry* **30**, 458–465 (2012).
51. Nieding, K. *et al.* Tau Tubulin Kinase TTBK2 Sensitivity of Glutamate Receptor GluK2. *Cellular Physiology and Biochemistry* **39**, 1444–1452 (2016).
52. Liachko, N. F. *et al.* The Tau Tubulin Kinases TTBK1/2 Promote Accumulation of Pathological TDP-43. *PLoS Genetics* **10**, (2014).
53. Prasad, A., Bharathi, V., Sivalingam, V., Girdhar, A. & Patel, B. K. Molecular mechanisms of TDP-43 misfolding and pathology in amyotrophic lateral sclerosis. *Frontiers in Molecular Neuroscience* **12**, 1–36 (2019).
54. Bender, C. & Ullrich, A. PRKX, TTBK2 and RSK4 expression causes sunitinib resistance in kidney carcinoma- and melanoma-cell lines. *International Journal of Cancer* **131**, (2012).
55. Qi, H. *et al.* Asator, a tau-tubulin kinase homolog in Drosophila localizes to the mitotic spindle. *Developmental Dynamics* **238**, 3248–3256 (2009).
56. Chaki, M. *et al.* Exome capture reveals ZNF423 and CEP164 mutations, linking renal ciliopathies to DNA damage response signaling. *Cell* **150**, 533–548 (2012).
57. Bowie, E. & Goetz, S. C. Ttbk2 and primary cilia are essential for the connectivity and survival of cerebellar purkinje neurons. *eLife* **9**, (2020).
58. Noble, W. *et al.* Inhibition of glycogen synthase kinase-3 by lithium correlates with reduced tauopathy and degeneration in vivo. *PNAS* **102**, 6990–6995 (2005).
59. Zhang, N. *et al.* Phosphorylation of synaptic vesicle protein 2A at Thr84 by casein kinase 1 family kinases controls the specific retrieval of synaptotagmin-1. *Journal of Neuroscience* **35**, 2492–2507 (2015).
60. Wang, L. & Dynlacht, B. D. The regulation of cilium assembly and disassembly in development and disease. *Development (Cambridge)* **145**, 1–13 (2018).
61. Badano, J. L., Mitsuma, N., Beales, P. L. & Katsanis, N. The ciliopathies: An emerging class of human genetic disorders. *Annual Review of Genomics and Human Genetics* **7**, 125–148 (2006).
62. Čajánek, L. & Nigg, E. A. Cep164 triggers ciliogenesis by recruiting Tau tubulin kinase 2 to the mother centriole. *Proceedings of the National Academy of Sciences of the United States of America* **111**, (2014).
63. Oda, T., Chiba, S., Nagai, T. & Mizuno, K. Binding to Cep164, but not EB1, is essential for centriolar localization of TTBK2 and its function in ciliogenesis. *Genes to Cells* **19**, 927–940 (2014).
64. Huang, N. *et al.* M-Phase Phosphoprotein 9 regulates ciliogenesis by modulating CP110-CEP97 complex localization at the mother centriole. *Nature Communications* **9**, (2018).
65. Lo, C. H. *et al.* Phosphorylation of CEP83 by TTBK2 is necessary for cilia initiation. *Journal of Cell Biology* **218**, 3489–3505 (2019).
66. Bernatik, O. *et al.* Phosphorylation of multiple proteins involved in ciliogenesis by Tau Tubulin kinase 2. *Molecular Biology of the Cell* **31**, 1032–1046 (2020).
67. Bah, A. *et al.* Folding of an intrinsically disordered protein by phosphorylation as a regulatory switch. *Nature* **519**, 106–109 (2015).
68. Bah, A. & Forman-Kay, J. D. Modulation of intrinsically disordered protein function by post-translational modifications. *Journal of Biological Chemistry* **291**, 6696–6705 (2016).
69. Xu, Q. *et al.* Phosphatidylinositol phosphate kinase PIPKIγ and phosphatase INPP5E coordinate initiation of ciliogenesis. *Nature Communications* **7**, (2016).
70. Spektor, A., Tsang, W. Y., Khoo, D. & Dynlacht, B. D. Cep97 and CP110 Suppress a Cilia Assembly Program. *Cell* **130**, 678–690 (2007).
71. Bowie, E., Norris, R., Anderson, K. v. & Goetz, S. C. Spinocerebellar ataxia type 11-associated alleles of Ttbk2 dominantly interfere with ciliogenesis and cilium stability. *PLoS Genetics* **14**, (2018).
72. McLaren, W. *et al.* The Ensembl Variant Effect Predictor. *Genome Biology* **17**, (2016).
73. Schwarz, J. M., Cooper, D. N., Schuelke, M. & Seelow, D. MutationTaster2: mutation prediction for the deep-sequencing age. *Nature Methods* **11**, 361–362 (2014).
74. Reva, B., Antipin, Y. & Sander, C. Predicting the functional impact of protein mutations: Application to cancer genomics. *Nucleic Acids Research* **39**, 1–14 (2011).

75. Pejaver, V., Mooney, S. D. & Radivojac, P. Missense variant pathogenicity predictors generalize well across a range of function-specific prediction challenges. *Human Mutation* **38**, 1092–1108 (2017).
76. Pejaver, V. *et al.* Inferring the molecular and phenotypic impact of amino acid variants with MutPred2. *Nature Communications* **11**, 1–13 (2020).
77. Shihab, H. A. *et al.* Predicting the Functional, Molecular, and Phenotypic Consequences of Amino Acid Substitutions using Hidden Markov Models. *Human Mutation* **34**, 57–65 (2013).
78. Shihab, H. A. *et al.* An integrative approach to predicting the functional effects of non-coding and coding sequence variation. *Bioinformatics* **31**, 1536–1543 (2015).
79. Rogers, M. F. *et al.* FATHMM-XF: Accurate prediction of pathogenic point mutations via extended features. *Bioinformatics* **34**, 511–513 (2018).
80. Chun, S. & Fay, J. C. Identification of deleterious mutations within three human genomes. *Genome Research* **19**, 1553–1561 (2009).
81. Raimondi, D. *et al.* DEOGEN2: Prediction and interactive visualization of single amino acid variant deleteriousness in human proteins. *Nucleic Acids Research* **45**, W201–W206 (2017).
82. Ionita-Laza, I., Mccallum, K., Xu, B. & Buxbaum, J. D. A spectral approach integrating functional genomic annotations for coding and noncoding variants. *Nature Genetics* **48**, 214–220 (2016).
83. Sim, N. L. *et al.* SIFT web server: Predicting effects of amino acid substitutions on proteins. *Nucleic Acids Research* **40**, W452–W457 (2012).
84. Choi, Y., Sims, G. E., Murphy, S., Miller, J. R. & Chan, A. P. Predicting the Functional Effect of Amino Acid Substitutions and Indels. *PLoS ONE* **7**, 1–13 (2012).
85. Choi, Y. & Chan, A. P. PROVEAN web server: A tool to predict the functional effect of amino acid substitutions and indels. *Bioinformatics* **31**, 2745–2747 (2015).
86. Qi, H. *et al.* MVP predicts the pathogenicity of missense variants by deep learning. *Nature Communications* **12**, 1–9 (2021).
87. Ioannidis, N. M. *et al.* REVEL: An Ensemble Method for Predicting the Pathogenicity of Rare Missense Variants. *American Journal of Human Genetics* **99**, 877–885 (2016).
88. Sundaram, L. *et al.* Predicting the clinical impact of human mutation with deep neural networks. *Nature Genetics* **50**, 1161–1170 (2018).
89. Dong, C. *et al.* Comparison and integration of deleteriousness prediction methods for nonsynonymous SNVs in whole exome sequencing studies. *Human Molecular Genetics* **24**, 2125–2137 (2015).
90. Jagadeesh, K. A. *et al.* M-CAP eliminates a majority of variants of uncertain significance in clinical exomes at high sensitivity. *Nature Genetics* **48**, 1581–1586 (2016).
91. Adzhubei, I. A. *et al.* A method and server for predicting damaging missense mutations. *Nature Methods* **7**, 248–249 (2010).
92. Fadista, J., Oskolkov, N., Hansson, O. & Groop, L. LoFtool: A gene intolerance score based on loss-of-function variants in 60 706 individuals. *Bioinformatics* **33**, 471–474 (2017).
93. González-Pérez, A. & López-Bigas, N. Improving the assessment of the outcome of nonsynonymous SNVs with a consensus deleteriousness score, Condel. *American Journal of Human Genetics* **88**, 440–449 (2011).
94. Feng, B. J. PERCH: A Unified Framework for Disease Gene Prioritization. *Human Mutation* **38**, 243–251 (2017).
95. Alirezaie, N., Kernohan, K. D., Hartley, T., Majewski, J. & Hocking, T. D. ClinPred: Prediction Tool to Identify Disease-Relevant Nonsynonymous Single-Nucleotide Variants. *American Journal of Human Genetics* **103**, 474–483 (2018).
96. Malhis, N., Jacobson, M., Jones, S. J. M. & Gsponer, J. LIST-S2: Taxonomy based sorting of deleterious missense mutations across species. *Nucleic Acids Research* **48**, W154–W161 (2020).
97. Carter, H., Douville, C., Stenson, P. D., Cooper, D. N. & Karchin, R. Identifying Mendelian disease genes with the variant effect scoring tool. *BMC genomics* **14**, 1–16 (2013).
98. Douville, C. *et al.* Assessing the Pathogenicity of Insertion and Deletion Variants with the Variant Effect Scoring Tool (VEST-Indel). *Human Mutation* **37**, 28–35 (2016).
99. Quang, D., Chen, Y. & Xie, X. DANN: A deep learning approach for annotating the pathogenicity of genetic variants. *Bioinformatics* **31**, 761–763 (2015).
100. Kircher, M. *et al.* A general framework for estimating the relative pathogenicity of human genetic variants. *Nature Genetics* **46**, 310–315 (2014).

101. Rentzsch, P., Witten, D., Cooper, G. M., Shendure, J. & Kircher, M. CADD: Predicting the deleteriousness of variants throughout the human genome. *Nucleic Acids Research* **47**, D886–D894 (2019).
102. Karczewski, K. J. *et al.* The mutational constraint spectrum quantified from variation in 141,456 humans. *Nature* **581**, 434–443 (2020).
103. Auton, A. *et al.* A global reference for human genetic variation. *Nature* **526**, 68–74 (2015).
104. Sherry, S. T., Ward, M. & Sirotkin, K. dbSNP-Database for Single Nucleotide Polymorphisms and Other Classes of Minor Genetic Variation. *Genome Res.* **9**, 677–679 (1999).
105. Pollard, K. S., Hubisz, M. J., Rosenbloom, K. R. & Siepel, A. Detection of nonneutral substitution rates on mammalian phylogenies. *Genome Research* **20**, 110–121 (2010).
106. Siepel, A. *et al.* Evolutionarily conserved elements in vertebrate, insect, worm, and yeast genomes. *Genome Research* **15**, 1034–1050 (2005).
107. Gulko, B., Hubisz, M., Gronau, I. & Siepel, A. Probabilities of Fitness Consequences for Point Mutations Across the Human Genome. *Nature Genetics* **47**, 276–283 (2015).
108. Davydov, E. v. *et al.* Identifying a high fraction of the human genome to be under selective constraint using GERP++. *PLoS Computational Biology* **6**, 1–13 (2010).
109. Rodrigues, C. H. M., Pires, D. E. V. & Ascher, D. B. DynaMut2: Assessing changes in stability and flexibility upon single and multiple point missense mutations. *Protein Science* **30**, 60–69 (2021).
110. Rodrigues, C. H. M., Pires, D. E. V. & Ascher, D. B. DynaMut: Predicting the impact of mutations on protein conformation, flexibility and stability. *Nucleic Acids Research* **46**, W350–W355 (2018).
111. Frappier, V. & Najmanovich, R. J. A Coarse-Grained Elastic Network Atom Contact Model and Its Use in the Simulation of Protein Dynamics and the Prediction of the Effect of Mutations. *PLoS Computational Biology* **10**, (2014).
112. Frappier, V., Chartier, M. & Najmanovich, R. J. ENCoM server: Exploring protein conformational space and the effect of mutations on protein function and stability. *Nucleic Acids Research* **43**, W395–W400 (2015).
113. Pires, D. E. V., Ascher, D. B. & Blundell, T. L. MCSM: Predicting the effects of mutations in proteins using graph-based signatures. *Bioinformatics* **30**, 335–342 (2014).
114. Pandurangan, A. P., Ochoa-Montaño, B., Ascher, D. B. & Blundell, T. L. SDM: A server for predicting effects of mutations on protein stability. *Nucleic Acids Research* **45**, W229–W235 (2017).
115. Pires, D. E. V., Ascher, D. B. & Blundell, T. L. DUET: A server for predicting effects of mutations on protein stability using an integrated computational approach. *Nucleic Acids Research* **42**, W314–W319 (2014).
116. Ormo, M. *et al.* Crystal Structure of the Aequorea victoria Green Fluorescent Protein The structure of GFP was determined by. *Science* **273**, 1392–1395 (1996).
117. Berman, H. M. *et al.* The Protein Data Bank. *Nucleic Acids Research* **28**, 235–242 (2000).
118. Mauthe, M. *et al.* Chloroquine inhibits autophagic flux by decreasing autophagosome-lysosome fusion. *Autophagy* **14**, 1435–1455 (2018).
119. Ran, F. A. *et al.* Genome engineering using the CRISPR-Cas9 system. *Nature Protocols* **8**, 2281–2308 (2013).
120. Bressan, R. B. *et al.* Efficient CRISPR/cas9-assisted gene targeting enables rapid and precise genetic manipulation of mammalian neural stem cells. *Development (Cambridge)* **144**, 635–648 (2017).
121. Riesenberg, S. *et al.* Simultaneous precise editing of multiple genes in human cells. *Nucleic acids research* **47**, e116 (2019).
122. Kostyushev, D. *et al.* Suppressing the NHEJ pathway by DNA-PKcs inhibitor NU7026 prevents degradation of HBV cccDNA cleaved by CRISPR/Cas9. *Scientific Reports* **9**, 1–11 (2019).
123. Hall & T. BioEdit : a user-friendly biological sequence alignment editor and analysis program for Windows 95/98/NT. *Nucleic Acids Symp. Ser.* **41**, 95–98 (1999).
124. Roberts, B. *et al.* Systematic gene tagging using CRISPR/Cas9 in human stem cells to illuminate cell organization. *Molecular Biology of the Cell* **28**, 2854–2874 (2017).
125. Livak, K. J. & Schmittgen, T. D. Analysis of Relative Gene Expression Data Using Real-Time Quantitative PCR and the 2−ΔΔCT Method. *Methods* **25**, 402–408 (2001).
126. Schmittgen, T. D. & Livak, K. J. Analyzing real-time PCR data by the comparative CT method. *Nature Protocols* **3**, 1101–1108 (2008).
127. Hughes, C. S. *et al.* Single-pot, solid-phase-enhanced sample preparation for proteomics experiments. *Nature Protocols* **14**, 68–85 (2019).

128. Osório, H. *et al.* Proteomics analysis of gastric cancer patients with diabetes mellitus. *Journal of Clinical Medicine* **10**, 1–14 (2021).
129. Wang, J., Vasaikar, S., Shi, Z., Greer, M. & Zhang, B. WebGestalt 2017: A more comprehensive, powerful, flexible and interactive gene set enrichment analysis toolkit. *Nucleic Acids Research* **45**, W130–W137 (2017).
130. Ashburner, M. *et al.* Gene ontology: Tool for the unification of biology. *Nature Genetics* **25**, 25–29 (2000).
131. Carbon, S. *et al.* The Gene Ontology resource: Enriching a GOld mine. *Nucleic Acids Research* **49**, D325–D334 (2021).
132. Kanehisa, M. & Goto, S. KEGG: Kyoto Encyclopedia of Genes and Genomes. *Nucleic Acids Research* **28**, 27–30 (2000).
133. Kanehisa, M., Furumichi, M., Sato, Y., Ishiguro-Watanabe, M. & Tanabe, M. KEGG: Integrating viruses and cellular organisms. *Nucleic Acids Research* **49**, D545–D551 (2021).
134. Thomas, P. D. *et al.* PANTHER: A library of protein families and subfamilies indexed by function. *Genome Research* **13**, 2129–2141 (2003).
135. Wu, G. & Haw, R. Functional interaction network construction and analysis for disease discovery. in *Methods in Molecular Biology* vol. 1558 235–253 (Humana Press Inc., 2017).
136. Griss, J. *et al.* ReactomeGSA - Efficient Multi-Omics Comparative Pathway Analysis. *Molecular and Cellular Proteomics* **19**, 2115–2124 (2020).
137. Martens, M. *et al.* WikiPathways: Connecting communities. *Nucleic Acids Research* **49**, D613–D621 (2021).
138. Piñero, J. *et al.* The DisGeNET knowledge platform for disease genomics: 2019 update. *Nucleic Acids Research* **48**, D845–D855 (2020).
139. Jourquin, J., Duncan, D., Shi, Z. & Zhang, B. GLAD4U: deriving and prioritizing gene lists from PubMed literature. *BMC genomics* **13**, 1–12 (2012).
140. Hamosh, A., Scott, A. F., Amberger, J. S., Bocchini, C. A. & McKusick, V. A. Online Mendelian Inheritance in Man (OMIM), a knowledgebase of human genes and genetic disorders. *Nucleic Acids Research* **33**, D514–D517 (2005).
141. Hornbeck, P. v. *et al.* PhosphoSitePlus, 2014: Mutations, PTMs and recalibrations. *Nucleic Acids Research* **43**, D512–D520 (2015).
142. Dinkel, H. *et al.* Phospho.ELM: A database of phosphorylation sites-update 2011. *Nucleic Acids Research* **39**, D261–D267 (2011).
143. Safaei, J., Maňuch, J., Gupta, A., Stacho, L. & Pelech, S. Prediction of 492 human protein kinase substrate specificities. *Proteome Science* **9**, 1–13 (2011).
144. Marcotte, D. J. *et al.* The crystal structure of the catalytic domain of tau tubulin kinase 2 in complex with a small-molecule inhibitor. *Acta Crystallographica Section F: Structural Biology Communications* **76**, 103–108 (2020).
145. Liao, J. C., Yang, T. T., Weng, R. R., Kuo, C. te & Chang, C. W. TTBK2: A tau protein kinase beyond tau phosphorylation. *BioMed Research International* **2015**, 1–10 (2015).
146. Xu, Z. *et al.* Microtubules acquire resistance from mechanical breakage through intralumenal acetylation. *Science* **356**, 328–332 (2017).
147. Eshun-Wilson, L. *et al.* Effects of α-tubulin acetylation on microtubule structure and stability. *Proceedings of the National Academy of Sciences of the United States of America* **116**, 10366–10371 (2019).
148. Menzies, F. M. *et al.* Autophagy and Neurodegeneration: Pathogenic Mechanisms and Therapeutic Opportunities. *Neuron* vol. 93 1015–1034 (2017).
149. Darios, F. & Stevanin, G. Impairment of Lysosome Function and Autophagy in Rare Neurodegenerative Diseases. *Journal of Molecular Biology* vol. 432 2714–2734 (2020).
150. Shaw, G., Morse, S., Ararat, M. & Graham, F. L. Preferential transformation of human neuronal cells by human adenoviruses and the origin of HEK 293 cells. *The FASEB journal : official publication of the Federation of American Societies for Experimental Biology* **16**, 869–871 (2002).
151. Lin, Y. C. *et al.* Genome dynamics of the human embryonic kidney 293 lineage in response to cell biology manipulations. *Nature Communications* **5**, 1–12 (2014).
152. Boldt, K. *et al.* An organelle-specific protein landscape identifies novel diseases and molecular mechanisms. *Nature Communications* **7**, 1–13 (2016).
153. Paquet, D. *et al.* Efficient introduction of specific homozygous and heterozygous mutations using CRISPR/Cas9. *Nature* **533**, 125–129 (2016).

154. Auzmendi-Iriarte, J. & Matheu, A. Impact of Chaperone-Mediated Autophagy in Brain Aging: Neurodegenerative Diseases and Glioblastoma. *Frontiers in Aging Neuroscience* **12**, 1–17 (2021).
155. Wu, H. *et al.* Crosstalk Between Macroautophagy and Chaperone-Mediated Autophagy: Implications for the Treatment of Neurological Diseases. *Molecular Neurobiology* **52**, 1284–1296 (2015).
156. Patel, B. & Cuervo, A. M. Methods to study chaperone-mediated autophagy. *Methods* **75**, 133–140 (2015).
157. Lee, C. R., Park, Y. H., Kim, Y. R., Peterkofsky, A. & Seok, Y. J. Phosphorylation-dependent mobility shift of proteins on SDS-PAGE is due to decreased binding of SDS. *Bulletin of the Korean Chemical Society* **34**, 2063–2066 (2013).
158. Lee, C. R., Park, Y. H., Min, H., Kim, Y. R. & Seok, Y. J. Determination of protein phosphorylation by polyacrylamide gel electrophoresis. *Journal of Microbiology* **57**, 93–100 (2019).
159. Bao, C. *et al.* Mechanisms of Regulation and Diverse Activities of Tau-Tubulin Kinase (TTBK) Isoforms. *Cellular and Molecular Neurobiology* **41**, 669–685 (2021).
160. Janssen, L. M. E. *et al.* Loss of Kif18A Results in Spindle Assembly Checkpoint Activation at Microtubule-Attached Kinetochores. *Current Biology* **28**, 2685–2696 (2018).
161. Noda, Y. *et al.* Phosphatidylinositol 4-phosphate 5-kinase alpha (PIPKα) regulates neuronal microtubule depolymerase kinesin, KIF2A and suppresses elongation of axon branches. *Proceedings of the National Academy of Sciences of the United States of America* **109**, 1725–1730 (2012).
162. Ogawa, T. & Hirokawa, N. Microtubule Destabilizer KIF2A Undergoes Distinct Site-Specific Phosphorylation Cascades that Differentially Affect Neuronal Morphogenesis. *Cell Reports* **12**, 1774–1788 (2015).
163. Broix, L. *et al.* Ciliogenesis and cell cycle alterations contribute to KIF2A-related malformations of cortical development. *Human Molecular Genetics* **27**, 224–238 (2018).
164. Uehara, R. *et al.* Aurora B and Kif2A control microtubule length for assembly of a functional central spindle during anaphase. *Journal of Cell Biology* **202**, 623–636 (2013).
165. Miyamoto, T. *et al.* The Microtubule-Depolymerizing activity of a mitotic kinesin protein KIF2A drives primary cilia disassembly coupled with cell proliferation. *Cell Reports* **10**, 664–673 (2015).
166. Janke, C. & Montagnac, G. Causes and Consequences of Microtubule Acetylation. *Current Biology* **27**, R1287–R1292 (2017).
167. Al-Bassam, J. & Chang, F. Regulation of microtubule dynamics by TOG-domain proteins XMAP215/Dis1 and CLASP. *Trends in Cell Biology* **21**, 604–614 (2011).
168. Lim, A. C. B., Tiu, S. Y., Li, Q. & Qi, R. Z. Direct Regulation of Microtubule Dynamics by Protein Kinase CK2. *Journal of Biological Chemistry* **279**, 4433–4439 (2004).
169. Mitsopoulos, C., Zihni, C., Garg, R., Ridley, A. J. & Morris, J. D. H. The prostate-derived sterile 20-like kinase (PSK) regulates microtubule organization and stability. *Journal of Biological Chemistry* **278**, 18085–18091 (2003).
170. Morelli, G. *et al.* p27Kip1 Modulates Axonal Transport by Regulating α-Tubulin Acetyltransferase 1 Stability. *Cell Reports* **23**, 2429–2442 (2018).
171. Even, A. *et al.* ATAT1-enriched vesicles promote microtubule acetylation via axonal transport. *Sciences Advances* **5**, 1–15 (2019).
172. Creppe, C. *et al.* Elongator Controls the Migration and Differentiation of Cortical Neurons through Acetylation of α-Tubulin. *Cell* **136**, 551–564 (2009).
173. Li, L. *et al.* MEC-17 deficiency leads to reduced α-tubulin acetylation and impaired migration of cortical neurons. *Journal of Neuroscience* **32**, 12673–12683 (2012).
174. Nekooki-Machida, Y. & Hagiwara, H. Role of tubulin acetylation in cellular functions and diseases. *Medical Molecular Morphology* **53**, 191–197 (2020).
175. Nekooki-Machida, Y. *et al.* Dynamic localization of α-tubulin acetyltransferase ATAT1 through the cell cycle in human fibroblastic KD cells. *Medical Molecular Morphology* **51**, 217–226 (2018).
176. Geeraert, C. *et al.* Starvation-induced hyperacetylation of tubulin is required for the stimulation of autophagy by nutrient deprivation. *Journal of Biological Chemistry* **285**, 24184–24194 (2010).
177. Pankiv, S. *et al.* p62/SQSTM1 binds directly to Atg8/LC3 to facilitate degradation of ubiquitinated protein aggregates by autophagy. *Journal of Biological Chemistry* **282**, 24131–24145 (2007).
178. Yamazaki, H., Tanji, K., Wakabayashi, K., Matsuura, S. & Itoh, K. Role of the Keap1/Nrf2 pathway in neurodegenerative diseases. *Pathology International* **65**, 210–219 (2015).

179. Taguchi, K., Motohashi, H. & Yamamoto, M. Molecular mechanisms of the Keap1-Nrf2 pathway in stress response and cancer evolution. *Genes to Cells* **16**, 123–140 (2011).
180. Kehl, S. R. *et al.* TAK 1 converts Sequestosome 1/p62 from an autophagy receptor to a signaling platform . *EMBO reports* **20**, 1–17 (2019).
181. Linares, J. F. *et al.* K63 polyubiquitination and activation of mTOR by the p62-TRAF6 complex in nutrient-activated cells. *Molecular Cell* **51**, 283–296 (2013).
182. Linares, J. F., Amanchy, R., Diaz-Meco, M. T. & Moscat, J. Phosphorylation of p62 by cdk1 Controls the Timely Transit of Cells through Mitosis and Tumor Cell Proliferation. *Molecular and Cellular Biology* **31**, 105–117 (2011).
183. Piras, A., Collin, L., Grüninger, F., Graff, C. & Rönnbäck, A. Autophagic and lysosomal defects in human tauopathies: analysis of post-mortem brain from patients with familial Alzheimer disease, corticobasal degeneration and progressive supranuclear palsy. *Acta neuropathologica communications* **4**, 1–13 (2016).
184. Bain, H. D. C. *et al.* The role of lysosomes and autophagosomes in frontotemporal lobar degeneration. *Neuropathology and Applied Neurobiology* **45**, 244–261 (2019).
185. Xia, Q. *et al.* TDP -43 loss of function increases TFEB activity and blocks autophagosome–lysosome fusion . *The EMBO Journal* **35**, 121–142 (2016).
186. Sun, L. *et al.* TAR DNA binding protein-43 loss of function induced by phosphorylation at S409/410 blocks autophagic flux and participates in secondary brain injury after intracerebral hemorrhage. *Frontiers in Cellular Neuroscience* **12**, 1–12 (2018).
187. Budini, M., Buratti, E., Morselli, E. & Criollo, A. Autophagy and its impact on neurodegenerative diseases: New roles for TDP-43 and C9orf72. *Frontiers in Molecular Neuroscience* **10**, 1–21 (2017).
188. Tsai, K. J. *et al.* Elevated expression of TDP-43 in the forebrain of mice is sufficient to cause neurological and pathological phenotypes mimicking FTLD-U. *Journal of Experimental Medicine* **207**, 1661–1673 (2010).
189. Talbert, P. B. & Henikoff, S. Histone variants ancient wrap artists of the epigenome. *Nature Reviews Molecular Cell Biology* **11**, 264–275 (2010).
190. Xiang, C., Zhang, S., Dong, X., Ma, S. & Cong, S. Transcriptional dysregulation and post-translational modifications in polyglutamine diseases: From pathogenesis to potential therapeutic strategies. *Frontiers in Molecular Neuroscience* **11**, 1–16 (2018).
191. Lehmkuhl, E. M. & Zarnescu, D. C. Lost in translation: Evidence for protein synthesis deficits in ALS/FTD and related neurodegenerative diseases. *Advances in Neurobiology* **20**, 283–301 (2018).
192. Funaba, M., Zimmerman, C. M. & Mathews, L. S. Modulation of Smad2-mediated signaling by extracellular signal-regulated kinase. *Journal of Biological Chemistry* **277**, 41361–41368 (2002).
193. Meyers, E. A. & Kessler, J. A. TGF-β family signaling in neural and neuronal differentiation, development, and function. *Cold Spring Harbor Perspectives in Biology* **9**, 1–25 (2017).
194. Wu, C. The PINCH-ILK-parvin complexes: Assembly, functions and regulation. *Biochimica et Biophysica Acta - Molecular Cell Research* **1692**, 55–62 (2004).
195. Kovalevich, J., Tracy, B. & Langford, D. PINCH: More than just an adaptor protein in cellular response. *Journal of Cellular Physiology* **226**, 940–947 (2011).
196. Kim, J. E., Lee, D. S., Kim, M. J. & Kang, T. C. PLPP/CIN-mediated NEDD4-2 S448 dephosphorylation regulates neuronal excitability via GluA1 ubiquitination. *Cell Death and Disease* **10**, 1–18 (2019).

ANNEX I

PCR protocol:

- PCR amplification was performed with a mix of:

Reagents	
H_2O	1,6 µL
TTBK2_Ex8_mix	2,4 µL
Ranger mix 2x	5 µL
DNA (~20 ng)	1 µL
Final reaction volume	10 µL

- PCR amplification parameters and annealing temperature for each primer pair (Tables 2.1 and 2.2) were as follow:

TTBK2 (clonal cell lines genotyping) and CRISPR/cas9 off-targets (*TAFA1, PIBF1, NEBL, DEPDC5, TCF4* and *KALRN*):

95ºC	15 min	
95ºC	45 sec	30x
60ºC	60 sec	
72ºC	60 sec	
72ºC	10 min	

TTBK2 2-15 exons and the CRISPR/Cas9 off target *STAT5B*:

95ºC	15 min	
95ºC	45 sec	30x
58ºC	60 sec	
72ºC	60 sec	
72ºC	10 min	

TTBK2 8-9 intron:

95ºC	15 min	
95ºC	45 sec	35x
60ºC	60 sec	
72ºC	90 sec	
72ºC	5 min	

Sequencing protocol:

After samples were obtained directly from PCR amplification, an additional step of purification before sequencing was required. To purify these products, 2 µL of PCR product was added to 0,5 µL of ExoSAP (GRiSP). The mixture was exposed to a temperature of 37ºC for 5 minutes and then, inactivated at 85ºC for 10 minutes.

- Sequencing reactions were performed with a mix of:

Reagents	
H_2O	5 µL
Primer (10 µM)	0,5 µL
BigDye v1.1 (1:1)	2 µL
PCR product	2,5 µL
Final reaction volume	10 µL

- Sequencing parameters were as followed:

95ºC	5 min	
96ºC	10 sec	35x
50ºC	5 sec	
60ºC	4 min	

RT-qPCR protocol:

- Quantitative Reverse-Transcription PCR was performed to measure *TTBK2* and *β-actin* mRNA levels (primers shown in Table 2.3) with a mix of:

Reagents	
H_2O	3,8 µL
Primer Mix (10 µM)	1,2 µL
PowerUP™ SYBR Green Master Mix	10 µL
cDNA (1:5)	5 µL
Final reaction volume	20 µL

- RT-qPCR parameters were as followed:

50 ºC	2 min	
95 ºC	10 min	
95 ºC	15 s	x40
58 ºC	1 min	
95 ºC	15 s	
60 ºC	1 min	
95 ºC	30 s	
60 ºC	15 s	

ANNEX II

Table S3.1 The TTBK2 variant (c.625C>T; p.Leu209Phe) nucleotide conservation and pathogenicity prediction scores.

Tool	Score
Nucleotide Conservation	
GERP++ RS	5,57
PhyloP100way (vertebrate)	10,003
PhyloP30way (mammalian)	1,176
PhyloP17way (primate)	0,676
PhastCons100way (vertebrate)	1,000
PhastCons30way (mammalian)	1,000
PhastCons17way (primate)	0,999
Integrated fitCons	0,7063
Pathogenicity Prediction	
MutationTaster	Disease-causing (1)
Mutation assessor	Medium (1,95)
FATHMM	Tolerated (1,89)
FATHMM-MKL	Damaging (0,97102)
FATHMM-XF	Damaging (0,845963)
LRT	Deleterious (0,0)
DEOGEN2	Tolerated (0,097979)
EIGEN	Pathogenic (13,96179)
EIGEN PC	Pathogenic (16,42539)
SIFT	Deleterious (0,01)
Provean	Damaging (-3,87)
MVP	Benign (0,533107066423)
REVEL	Pathogenic (0,638)
Primate AI	Damaging (0,905742049217)
MetaSVM	Tolerated (-0,5563)
MetaLR	Tolerated (0,2289)
M-CAP	Damaging (0,035096)
Polyphen	Probably damaging (0,999)
LoFtool	Probably damaging (0,435)
Condel	Deleterious (0,896)

BayesDel addAF	Damaging (0,244987)
BayesDel noAF	Damaging (0,11413)
ClinPred	Damaging (0,995844900608063)
LIST-S2	Damaging (0,991087)
VEST4	0,773
MutPred	0,6
DANN	0,999077798
CADD Score	28

CADD, Mutpred, DANN and VEST4 scores are considered as pathogenic above 20, 0,5, 0,5 and 0,5, respectively. In nucleotide conservation scores, the larger the score, the more conserved the site. GERP++ RS, PhastCons (17, 30 and 100way), PhyloP100way, Phylo30way, Phylo17way, and integrated fitCons scores range from -12,3 to 6,17; 0 to 1; -20 to 10,003; -20 to 1,312; -13,362 to 0,756; and 0 to 1, respectively.

ANNEX II

Table S3.2 The ORA complete data before the processing step of redundancy reduction.

	Gene Set	Description	Gene Symbol	Size	Expect	Ratio	P-value	FDR
+	WP4320	The effect of progerin on the involved genes in Hutchinson-Gilford Progeria Syndrome	H3F3B;H3F3A;HIST2H3D;HIST2H3C;HIST2H3A;MBD2	37	0,0995	60,318	6,0778E-10	0,000012913
+	R-HSA-73728	RNA Polymerase I Promoter Opening	H3F3B;H3F3A;HIST2H3D;HIST2H3C;HIST2H3A;MBD2	63	0,1694	35,425	1,6847E-08	0,00017898
+	WP4553	FBXL10 enhancement of MAP/ERK signaling in diffuse large B-cell lymphoma	H3F3B;H3F3A;HIST2H3D;HIST2H3C;HIST2H3A	35	0,0941	53,137	3,5075E-08	0,00024842
+	R-HSA-1266738	Developmental Biology	PIAS2;SLIT2;KRT1;KRT10;GAP43;PFN2;KRT9;H3F3B;H3F3A;SMAD4;SMAD2;HIST2H3D;HIST2H3C;HIST2H3A;PIK3R3	1074	2,8874	5,195	8,2996E-08	0,00044086
+	R-HSA-427413	NoRC negatively regulates rRNA expression	H3F3B;H3F3A;HIST2H3D;HIST2H3C;HIST2H3A;MBD2	106	0,2850	21,054	3,8752E-07	0,0013522
+	R-HSA-5250941	Negative epigenetic regulation of rRNA expression	H3F3B;H3F3A;HIST2H3D;HIST2H3C;HIST2H3A;MBD2	109	0,2930	20,475	4,5721E-07	0,0013522
+	R-HSA-73854	RNA Polymerase I Promoter Clearance	H3F3B;H3F3A;HIST2H3D;HIST2H3C;	109	0,2930	20,475	4,5721E-07	0,0013522

			HIST2H3A; MBD2					
+	R-HSA-73864	RNA Polymerase I Transcription	H3F3B;H3F3A;HIST2H3D;HIST2H3C; HIST2H3A; MBD2	111	0,2984	20,106	5,0914E-07	0,0013522
+	R-HSA-5334118	DNA methylation	H3F3B;H3F3A;HIST2H3D;HIST2H3C; HIST2H3A	65	0,1748	28,612	8,3992E-07	0,0014924
+	R-HSA-5617472	Activation of anterior HOX genes in hindbrain development during early embryogenesis	PIAS2;H3F3B;H3F3A;HIST2H3D;HIST2H3C;HIST2H3A	122	0,3280	18,293	8,8878E-07	0,0014924
+	R-HSA-5619507	Activation of HOX genes during differentiation	PIAS2;H3F3B;H3F3A;HIST2H3D;HIST2H3C;HIST2H3A	122	0,3280	18,293	8,8878E-07	0,0014924
+	R-HSA-5625886	Activated PKN1 stimulates transcription of AR (androgen receptor) regulated genes KLK2 and KLK3	H3F3B;H3F3A;HIST2H3D;HIST2H3C; HIST2H3A	67	0,1801	27,758	9,7809E-07	0,0014924
+	WP2369	Histone Modifications	H3F3B;H3F3A;HIST2H3D;HIST2H3C; HIST2H3A	67	0,1801	27,758	9,7809E-07	0,0014924
+	R-HSA-2559580	Oxidative Stress Induced Senescence	H3F3B;H3F3A;HIST2H3D;HIST2H3C; HIST2H3A;TNIK	125	0,3361	17,854	0,000001025	0,0014924
+	R-HSA-427359	SIRT1 negatively regulates rRNA expression	H3F3B;H3F3A;HIST2H3D;HIST2H3C; HIST2H3A	68	0,1828	27,350	0,000001054	0,0014924
+	R-HSA-212300	PRC2 methylates histones and DNA	H3F3B;H3F3A;HIST2H3D;HIST2H3C; HIST2H3A	73	0,1963	25,477	0,000001503	0,0019957
+	R-HSA-2299718	Condensation of Prophase Chromosomes	H3F3B;H3F3A;HIST2H3D;HIST2H3C; HIST2H3A	74	0,1990	25,132	0,000001609	0,0020104
+	R-HSA-427389	ERCC6 (CSB) and EHMT2 (G9a) positively regulate rRNA expression	H3F3B;H3F3A;HIST2H3D;HIST2H3C; HIST2H3A	76	0,2043	24,471	0,000001837	0,0021688
+	R-HSA-1266695	Interleukin-7 signaling	H3F3B;H3F3A;HIST2H3D;HIST2H3C; HIST2H3A;PIK3R3	36	0,0968	41,329	0,000002561	0,002864
+	R-HSA-212165	Epigenetic regulation of gene expression	H3F3B;H3F3A;HIST2H3D;HIST2H3C;	148	0,3979	15,079	0,000002747	0,0029183

			HIST2H3A; MBD2					
+	R-HSA-912446	Meiotic recombination	H3F3B;H3F3A;HIST2H3D;HIST2H3C; HIST2H3A	86	0,2312	21,626	0,000003394	0,0034341
+	R-HSA-73777	RNA Polymerase I Chain Elongation	H3F3B;H3F3A;HIST2H3D;HIST2H3C; HIST2H3A	90	0,2420	20,664	0,000004249	0,0039721
+	R-HSA-201722	Formation of the β-catenin:TCF transactivating complex	H3F3B;H3F3A;HIST2H3D;HIST2H3C; HIST2H3A	91	0,2447	20,437	0,000004487	0,0039721
+	R-HSA-5250924	B-WICH complex positively regulates rRNA expression	H3F3B;H3F3A;HIST2H3D;HIST2H3C; HIST2H3A	91	0,2447	20,437	0,000004487	0,0039721
+	R-HSA-1912408	Pre-NOTCH Transcription and Translation	H3F3B;H3F3A;HIST2H3D;HIST2H3C; HIST2H3A	93	0,2500	19,998	0,000004994	0,0042443
+	GO:0051253	negative regulation of RNA metabolic process	HEXIM1;ZIC2;H3F3A;MECOM;FOXM1;SMAD4;SQSTM1;ARID5B;SMAD2;HIST2H3C; NEDD4L;DHX36;MBD2; MBD1	1295	3,4815	4,021	0,000005253	0,0042924
+	R-HSA-5625740	RHO GTPases activate PKNs	H3F3B;H3F3A;HIST2H3D;HIST2H3C; HIST2H3A	95	0,2554	19,577	0,000005545	0,0043636
-	R-HSA-446353	Cell-extracellular matrix interactions	LIMS1;ILK;PARVB;PARVA	18	0,0541	73,957	2,1717E-07	0,0046143
+	R-HSA-8936459	RUNX1 regulates genes involved in megakaryocyte differentiation and platelet function	H3F3B;H3F3A;HIST2H3D;HIST2H3C; HIST2H3A	97	0,2608	19,173	0,000006143	0,0046614
+	PA446493	Hyperkeratosis, Epidermolytic	KRT1;KRT10;KRT9	14	0,0376	79,706	0,000006526	0,0047811
+	GO:0045892	negative regulation of transcription, DNA-templated	HEXIM1;ZIC2;H3F3A;MECOM;FOXM1;SMAD4;SQSTM1;ARID5B;SMAD2;HIST2H3C; NEDD4L;MBD2;MBD1	1167	3,1374	4,144	0,000008964	0,0059276
+	R-HSA-5578749	Transcriptional regulation by small RNAs	H3F3B;H3F3A;HIST2H3D;HIST2H3C; HIST2H3A	105	0,2823	17,712	0,000009056	0,0059276
+	GO:2000113	negative regulation of cellular macromolecule biosynthetic process	HEXIM1;ZIC2;H3F3A;MECOM;FOXM1;SMAD4;SQSTM1;ARI	1359	3,6536	3,832	0,000009155	0,0059276

			D5B;SMAD2;HIST2H3C;NEDD4L;DHX36;MBD2;MBD1					
+	R-HSA-5250913	Positive epigenetic regulation of rRNA expression	H3F3B;H3F3A;HIST2H3D;HIST2H3C;HIST2H3A	106	0,2850	17,545	0,000009486	0,0059276
+	R-HSA-977225	Amyloid fiber formation	H3F3B;H3F3A;HIST2H3D;HIST2H3C;HIST2H3A	106	0,2850	17,545	0,000009486	0,0059276
+	GO:0000183	chromatin silencing at rDNA	H3F3A;HIST2H3C;MBD2	16	0,0430	69,743	0,000010002	0,0060716
+	R-HSA-3214842	HDMs demethylate histones	ARID5B;HIST2H3D;HIST2H3C;HIST2H3A	51	0,1371	29,173	0,000010547	0,006225
+	R-HSA-1912422	Pre-NOTCH Expression and Processing	H3F3B;H3F3A;HIST2H3D;HIST2H3C;HIST2H3A	109	0,2930	17,062	0,000010869	0,0062415
+	R-HSA-2559582	Senescence-Associated Secretory Phenotype (SASP)	H3F3B;H3F3A;HIST2H3D;HIST2H3C;HIST2H3A	110	0,2957	16,907	0,000011364	0,0063538
+	GO:0072359	circulatory system development	SLIT2;HEXIM1;ANXA1;KRT1;SMAD4;SHB;SMAD2;AMOT;BBS7;PIK3R3;DHX36;MBD2	1026	2,7584	4,350	0,000013133	0,0071122
+	R-HSA-2559583	Cellular Senescence	H3F3B;H3F3A;HIST2H3D;HIST2H3C;HIST2H3A;TNIK	195	0,5243	11,445	0,000013390	0,0071122
+	GO:1903507	negative regulation of nucleic acid-templated transcription	HEXIM1;ZIC2;H3F3A;MECOM;FOXM1;SMAD4;SQSTM1;ARID5B;SMAD2;HIST2H3C;NEDD4L;MBD2;MBD1	1215	3,2665	3,980	0,000013823	0,0071169
+	GO:1902679	negative regulation of RNA biosynthetic process	HEXIM1;ZIC2;H3F3A;MECOM;FOXM1;SMAD4;SQSTM1;ARID5B;SMAD2;HIST2H3C;NEDD4L;MBD2;MBD1	1217	3,2719	3,973	0,000014068	0,0071169
+	GO:0045934	negative regulation of nucleobase-containing compound metabolic process	HEXIM1;ZIC2;H3F3A;MECOM;FOXM1;SMAD4;SQSTM1;ARID5B;SMAD2	1418	3,8122	3,672	0,000014856	0,0073404

			;HIST2H3C;NEDD4L;DHX36;MBD2;MBD1					
+	R-HSA-1500620	Meiosis	H3F3B;H3F3A;HIST2H3D;HIST2H3C;HIST2H3A	118	0,3172	15,761	0,000015984	0,0077187
+	GO:0010558	negative regulation of macromolecule biosynthetic process	HEXIM1;ZIC2;H3F3A;MECOM;FOXM1;SMAD4;SQSTM1;ARID5B;SMAD2;HIST2H3C;NEDD4L;DHX36;MBD2;MBD1	1434	3,8552	3,631	0,000016866	0,0079634
+	PA446275	Epidermolysis Bullosa Simplex	KRT1;KRT10;KRT9	21	0,0565	53,137	0,000023530	0,010868
+	R-HSA-8939236	RUNX1 regulates transcription of genes involved in differentiation of HSCs	H3F3B;H3F3A;HIST2H3D;HIST2H3C;HIST2H3A	130	0,3495	14,306	0,000025525	0,011539
+	GO:0031327	negative regulation of cellular biosynthetic process	HEXIM1;ZIC2;H3F3A;MECOM;FOXM1;SMAD4;SQSTM1;ARID5B;SMAD2;HIST2H3C;NEDD4L;DHX36;MBD2;MBD1	1492	4,0112	3,490	0,000026331	0,011655
+	hsa05322	Systemic lupus erythematosus	H3F3B;H3F3A;HIST2H3D;HIST2H3C;HIST2H3A	133	0,3576	13,983	0,000028487	0,012352
+	R-HSA-211000	Gene Silencing by RNA	H3F3B;H3F3A;HIST2H3D;HIST2H3C;HIST2H3A	135	0,3629	13,776	0,000030605	0,012854
+	R-HSA-2173795	Downregulation of SMAD2/3:SMAD4 transcriptional activity	SMAD4;SMAD2;NEDD4L	23	0,0618	48,517	0,000031213	0,012854
+	GO:0009890	negative regulation of biosynthetic process	HEXIM1;ZIC2;H3F3A;MECOM;FOXM1;SMAD4;SQSTM1;ARID5B;SMAD2;HIST2H3C;NEDD4L;DHX36;MBD2;MBD1	1516	4,0757	3,435	0,000031458	0,012854
+	GO:0010629	negative regulation of gene expression	CTIF;HEXIM1;ZIC2;H3F3A;MECOM;FOXM1;SMAD4;SQSTM1;ARID5B;SMAD2;HIST2H	1733	4,6591	3,220	0,000032464	0,013014

			3C;NEDD4L;DHX36;MBD2;MBD1					
+	R-HSA-68875	Mitotic Prophase	H3F3B;H3F3A;HIST2H3D;HIST2H3C;HIST2H3A	141	0,3791	13,190	0,000037701	0,014834
-	R-HSA-446388	Regulation of cytoskeletal remodeling and cell spreading by IPP complex components	LIMS1;PARVB;PARVA	8	0,0240	124,800	0,000001425	0,015139
+	R-HSA-3214841	PKMTs methylate histone lysines	MECOM;HIST2H3D;HIST2H3C;HIST2H3A	71	0,1909	20,956	0,000039417	0,015227
+	R-HSA-1474165	Reproduction	H3F3B;H3F3A;HIST2H3D;HIST2H3C;HIST2H3A	144	0,3871	12,915	0,000041696	0,01582
+	R-HSA-9018519	Estrogen-dependent gene expression	H3F3B;H3F3A;HIST2H3D;HIST2H3C;HIST2H3A	150	0,4033	12,399	0,000050666	0,018886
+	GO:0010639	negative regulation of organelle organization	MID1;SEC22B;SLIT2;PFN2;LMAN1;H3F3A;SMAD4	371	0,9974	7,018	0,000057082	0,020596
+	PA165109021	Congenital ichthyosiform erythroderma	KRT1;KRT10;KRT9	28	0,0753	39,853	0,000057193	0,020596
+	GO:0006342	chromatin silencing	H3F3A;HIST2H3C;MBD2;MBD1	79	0,2124	18,833	0,000059995	0,021245
+	R-HSA-8939211	ESR-mediated signaling	H3F3B;H3F3A;HIST2H3D;HIST2H3C;HIST2H3A	156	0,4194	11,922	0,000061060	0,021268
+	PA444062	Epidermolysis Bullosa	KRT1;KRT10;KRT9	29	0,0780	38,479	0,000063671	0,02182
+	GO:0001667	ameboidal-type cell migration	SLIT2;ANXA1;PFN2;ARID5B;AMOT;PIK3R3;AMOTL2	381	1,0243	6,834	0,000067475	0,022756
+	PA165108896	Ichthyosis bullosa of Siemens	KRT1;KRT10	5	0,0134	148,780	0,000070499	0,023405
+	R-HSA-983231	Factors involved in megakaryocyte development and platelet production	H3F3B;H3F3A;HIST2H3D;HIST2H3C;HIST2H3A	166	0,4463	11,204	0,000081963	0,026792
+	R-HSA-2173789	TGF-beta receptor signaling activates SMADs	SMAD4;SMAD2;NEDD4L	32	0,0860	34,871	0,000085938	0,027666
+	GO:0060021	roof of mouth development	SMAD4;ARID5B;SMAD2;BBS7	89	0,2393	16,717	0,000095586	0,030312
+	hsa05034	Alcoholism	H3F3B;H3F3A;HIST2H3D;HIST2H3C;HIST2H3A	180	0,4839	10,332	0,000120020	0,0375

+	GO:0045814	negative regulation of gene expression, epigenetic	H3F3A;HIST2H3C;MBD2;MBD1	95	0,2554	15,662	0,000123160	0,037925
+	R-HSA-2262752	Cellular responses to stress	H3F3B;H3F3A;TXNRD1;HIST2H3D;HIST2H3C;HIST2H3A;TNIK	426	1,1453	6,112	0,000135270	0,041058
+	hsa05202	Transcriptional misregulation in cancer	H3F3B;H3F3A;HIST2H3D;HIST2H3C;HIST2H3A	186	0,5001	9,999	0,000139950	0,041797
+	C0079153	Hyperkeratosis, Epidermolytic	KRT1;KRT10	7	0,0188	106,270	0,000147540	0,041797
+	GO:0071141	SMAD protein complex	SMAD4;SMAD2	7	0,0188	106,270	0,000147540	0,041797
+	R-HSA-3304349	Loss of Function of SMAD2/3 in Cancer	SMAD4;SMAD2	7	0,0188	106,270	0,000147540	0,041797
+	R-HSA-3315487	SMAD2/3 MH2 Domain Mutants in Cancer	SMAD4;SMAD2	7	0,0188	106,270	0,000147540	0,041797

A P-value ≤ 0.05 was considered with adjustment using the Benjamini–Hochberg approach.

Table S3.3 The GSEA complete information, before the processing step of redundancy reduction.

Gene Set	Description	Size	LEN	NES	P-value	FDR
GO:Biological Process						
GO:0098927	vesicle-mediated transport between endosomal compartments	22	17	3,1446	0	0
GO:0044380	protein localization to cytoskeleton	33	20	2,8154	0	0,00127
GO:0016482	cytosolic transport	73	43	2,7786	0	0,00085
GO:1903311	regulation of mRNA metabolic process	185	162	2,7630	0	0,00095
GO:0097485	neuron projection guidance	50	26	2,7300	0	0,00127
GO:0032147	activation of protein kinase activity	102	57	2,7033	0	0,00106
GO:0051493	regulation of cytoskeleton organization	212	123	2,6415	0	0,002
GO:0006397	mRNA processing	346	237	2,4897	0	0,01114
GO:0008380	RNA splicing	297	205	2,4562	0	0,01273
GO:0030323	respiratory tube development	33	25	2,4036	0	0,01693
GO:0045088	regulation of innate immune response	101	53	2,3127	0,00199	0,02847
GO:0044782	cilium organization	139	81	2,2931	0,00417	0,03045
GO:0061564	axon development	128	62	2,2722	0	0,03193
GO:0042176	regulation of protein catabolic process	156	91	2,2383	0	0,03983
GO:0031023	microtubule organizing center organization	65	43	2,2252	0	0,04074
GO:0071103	DNA conformation change	146	108	2,2245	0	0,03851
GO:0031098	stress-activated protein kinase signaling cascade	109	56	2,2052	0	0,04142
GO:0009895	negative regulation of catabolic process	127	74	2,1995	0,00404	0,04074

GO:0006605	protein targeting	188	106	-2,2427	0	0,03212
GO:0009141	nucleoside triphosphate metabolic process	118	62	-2,2674	0,00198	0,03069
GO:0002181	cytoplasmic translation	65	47	-2,4747	0	0,00762
GO:0034470	ncRNA processing	258	217	-2,5665	0	0,0045
GO:0006091	generation of precursor metabolites and energy	166	82	-2,8683	0	0
GO:0070972	protein localization to endoplasmic reticulum	99	67	-2,9691	0	0
GO:0006413	translational initiation	145	102	-3,0212	0	0
GO:0022613	ribonucleoprotein complex biogenesis	341	292	-3,1128	0	0
GO:Cellular Component						
GO:0044441	ciliary part	102	56	2,4996	0	0,01976
GO:0031227	intrinsic component of endoplasmic reticulum membrane	38	28	-2,0114	0,00612	0,0319
GO:0070069	cytochrome complex	12	10	-2,3120	0	0,00444
GO:0005759	mitochondrial matrix	228	161	-2,3361	0	0,00382
GO:0101031	chaperone complex	17	10	-2,4111	0	0,00293
GO:0070469	respiratory chain	31	22	-2,6928	0	0,00036
GO:0044455	mitochondrial membrane part	82	53	-3,2805	0	0
GO:0098798	mitochondrial protein complex	128	73	-3,4443	0	0
GO:0005840	ribosome	165	114	-3,4889	0	0
GO:0044445	cytosolic part	147	99	-3,5318	0	0
GO:0005743	mitochondrial inner membrane	177	135	-3,5869	0	0
GO:1990204	oxidoreductase complex	44	35	-3,7770	0	0
GO:Molecular Function						
GO:0017056	structural constituent of nuclear pore	17	16	-2,2212	0	0,03644
GO:0070003	threonine-type peptidase activity	14	12	-2,2866	0,00198	0,03411
GO:0019843	rRNA binding	46	37	-2,4642	0	0,01448
GO:0003735	structural constituent of ribosome	116	87	-3,9336	0	0
KEGG						
hsa05322	Systemic lupus erythematosus	45	32	4,5817	0	0
hsa05034	Alcoholism	62	40	4,4201	0	0
hsa04360	Axon guidance	44	30	2,6887	0	0,00252
hsa05203	Viral carcinogenesis	103	73	2,5737	0	0,00347
hsa05214	Glioma	28	25	2,4885	0,00188	0,00732
hsa04012	ErbB signaling pathway	42	34	2,4017	0	0,01094
hsa05225	Hepatocellular carcinoma	58	44	2,3366	0,00205	0,01461
hsa04650	Natural killer cell mediated cytotoxicity	25	18	2,3119	0	0,01405
hsa04660	T cell receptor signaling pathway	37	24	2,2409	0	0,0188
hsa05223	Non-small cell lung cancer	31	26	2,2123	0,002	0,01957
hsa01521	EGFR tyrosine kinase inhibitor resistance	33	27	2,1876	0,00197	0,02146
hsa05205	Proteoglycans in cancer	73	52	2,1457	0,00195	0,02714
hsa03040	Spliceosome	111	81	2,1313	0,00416	0,02777
hsa04722	Neurotrophin signaling pathway	49	22	2,1284	0	0,02624

hsa05220	Chronic myeloid leukemia	37	18	2,0953	0,00197	0,03215
hsa05130	Pathogenic Escherichia coli infection	29	22	2,0893	0,00418	0,0314
hsa05010	Alzheimer disease	58	33	-2,2392	0	0,021
hsa03022	Basal transcription factors	27	18	-2,3946	0	0,00698
hsa03013	RNA transport	125	86	-2,4132	0	0,00734
hsa04714	Thermogenesis	81	44	-2,4890	0	0,00441
hsa03010	Ribosome	100	76	-3,8302	0	0
Panther						
P00047	PDGF signaling pathway	52	44	2,4389	0	0,00517
P00005	Angiogenesis	51	18	2,1939	0,00626	0,02263
Wikipathway						
WP2369	Histone Modifications	50	32	3,5679	0	0
WP4553	FBXL10 enhancement of MAP/ERK signaling in diffuse large B-cell lymphoma	27	21	3,3847	0	0
WP4320	The effect of progerin on the involved genes in Hutchinson-Gilford Progeria Syndrome	33	20	3,0253	0	0
WP481	Insulin Signaling	78	44	2,8462	0	0
WP51	Regulation of Actin Cytoskeleton	58	33	2,5035	0	0,00873
WP673	ErbB Signaling Pathway	45	36	2,3914	0	0,01713
WP4656	Joubert Syndrome	28	22	2,3527	0	0,01871
WP1449	Regulation of toll-like receptor signaling pathway	39	24	2,3207	0,00406	0,01989
WP4685	Melanoma	26	22	2,1821	0	0,0485
WP4297	Thiamine metabolic pathways	6	6	-2,2664	0	0,04053
WP477	Cytoplasmic Ribosomal Proteins	74	56	-3,4191	0	0
Reactome						
R-HSA-73728	RNA Polymerase I Promoter Opening	35	33	5,6718	0	0
R-HSA-5625886	Activated PKN1 stimulates transcription of AR (androgen receptor) regulated genes KLK2 and KLK3	35	32	5,6012	0	0
R-HSA-977225	Amyloid fiber formation	35	31	5,3247	0	0
R-HSA-2299718	Condensation of Prophase Chromosomes	43	35	5,2690	0	0
R-HSA-427359	SIRT1 negatively regulates rRNA expression	36	31	5,2606	0	0
R-HSA-5334118	DNA methylation	36	31	5,1924	0	0
R-HSA-1912408	Pre-NOTCH Transcription and Translation	49	36	5,0483	0	0
R-HSA-1912422	Pre-NOTCH Expression and Processing	51	36	4,9144	0	0
R-HSA-8936459	RUNX1 regulates genes involved in megakaryocyte differentiation and platelet function	51	38	4,9104	0	0

R-HSA-201722	Formation of the beta-catenin:TCF transactivating complex	50	36	4,7210	0	0
R-HSA-212300	PRC2 methylates histones and DNA	42	31	4,7082	0	0
R-HSA-5625740	RHO GTPases activate PKNs	56	36	4,6426	0	0
R-HSA-912446	Meiotic recombination	45	32	4,6229	0	0
R-HSA-2559582	Senescence-Associated Secretory Phenotype (SASP)	54	35	4,4847	0	0
R-HSA-427389	ERCC6 (CSB) and EHMT2 (G9a) positively regulate rRNA expression	47	33	4,4624	0	0
R-HSA-5617472	Activation of anterior HOX genes in hindbrain development during early embryogenesis	64	39	4,3208	0	0
R-HSA-5619507	Activation of HOX genes during differentiation	64	39	4,3208	0	0
R-HSA-2559580	Oxidative Stress Induced Senescence	68	42	4,3197	0	0
R-HSA-3214842	HDMs demethylate histones	44	29	4,1140	0	0
R-HSA-5250924	B-WICH complex positively regulates rRNA expression	54	32	4,0192	0	0
R-HSA-73777	RNA Polymerase I Chain Elongation	54	32	3,9701	0	0
R-HSA-1474165	Reproduction	62	34	3,9290	0	0
R-HSA-1500620	Meiosis	62	34	3,9290	0	0
R-HSA-3214858	RMTs methylate histone arginines	55	30	3,6263	0	0
R-HSA-3214841	PKMTs methylate histone lysines	58	31	3,5371	0	0
R-HSA-211000	Gene Silencing by RNA	80	37	3,5025	0	0
R-HSA-427413	NoRC negatively regulates rRNA expression	69	36	3,4847	0	0
R-HSA-73854	RNA Polymerase I Promoter Clearance	70	36	3,4823	0	0
R-HSA-2559583	Cellular Senescence	103	50	3,4784	0	0
R-HSA-8939211	ESR-mediated signaling	87	47	3,4778	0	0
R-HSA-5578749	Transcriptional regulation by small RNAs	68	33	3,4579	0	0
R-HSA-73864	RNA Polymerase I Transcription	71	36	3,4528	0	0
R-HSA-171306	Packaging Of Telomere Ends	21	16	3,4467	0	0
R-HSA-5250941	Negative epigenetic regulation of rRNA expression	72	41	3,4387	0	0
R-HSA-3214815	HDACs deacetylate histones	57	31	3,4311	0	0
R-HSA-9018519	Estrogen-dependent gene expression	84	46	3,3685	0	0
R-HSA-1266695	Interleukin-7 signaling	20	15	3,3282	0	0

R-HSA-5250913	Positive epigenetic regulation of rRNA expression	68	34	3,3248	0	0
R-HSA-68875	Mitotic Prophase	95	46	3,2931	0	0
R-HSA-8939236	RUNX1 regulates transcription of genes involved in differentiation of HSCs	79	35	3,1417	0	0
R-HSA-157118	Signaling by NOTCH	120	45	3,1158	0	0
R-HSA-9006931	Signaling by Nuclear Receptors	97	47	3,0585	0	0
R-HSA-8878171	Transcriptional regulation by RUNX1	139	51	3,0154	0	0
R-HSA-606279	Deposition of new CENPA-containing nucleosomes at the centromere	34	19	2,9874	0	0
R-HSA-774815	Nucleosome assembly	34	19	2,9874	0	0
R-HSA-3214847	HATs acetylate histones	91	36	2,9009	0	4,7E-05
R-HSA-194315	Signaling by Rho GTPases	246	145	2,7524	0	0,00023
R-HSA-162582	Signal Transduction	705	367	2,7415	0	0,00025
R-HSA-201681	TCF dependent signaling in response to WNT	115	42	2,7337	0	0,00027
R-HSA-195258	RHO GTPase Effectors	196	117	2,7150	0	0,0003
R-HSA-72172	mRNA Splicing	158	127	2,4717	0	0,00171
R-HSA-881907	Gastrin-CREB signalling pathway via PKC and MAPK	7	7	2,4390	0	0,00209
R-HSA-72163	mRNA Splicing - Major Pathway	155	124	2,4078	0	0,00267
R-HSA-373755	Semaphorin interactions	28	23	2,3428	0	0,00429
R-HSA-5693538	Homology Directed Repair	78	68	2,2544	0	0,00807
R-HSA-73886	Chromosome Maintenance	63	47	2,2196	0	0,01029
R-HSA-5357786	TNFR1-induced proapoptotic signaling	6	6	2,1968	0	0,01217
R-HSA-1660514	Synthesis of PIPs at the Golgi membrane	10	9	2,1716	0,002	0,01462
R-HSA-73614	Pyrimidine salvage	5	5	2,0832	0,00637	0,02669
R-HSA-168638	NOD1/2 Signaling Pathway	13	11	2,0770	0,00969	0,02727
R-HSA-73857	RNA Polymerase II Transcription	508	299	2,0693	0	0,028
R-HSA-186763	Downstream signal transduction	12	7	2,0372	0,01018	0,03329
R-HSA-199977	ER to Golgi Anterograde Transport	75	66	1,9709	0,00443	0,04596
R-HSA-380320	Recruitment of NuMA to mitotic centrosomes	57	36	1,9558	0,00415	0,04907
R-HSA-1483249	Inositol phosphate metabolism	17	14	1,9525	0,00426	0,04956
R-HSA-8949664	Processing of SMDT1	10	8	-1,8970	0,01193	0,04525
R-HSA-389958	Cooperation of Prefoldin and TriC/CCT in actin and tubulin folding	17	8	-1,9217	0,0037	0,0397
R-HSA-200425	Import of palmitoyl-CoA into the mitochondrial matrix	6	5	-1,9334	0,00611	0,0377
R-HSA-418346	Platelet homeostasis	14	8	-1,9550	0,00398	0,03384

R-HSA-1234176	Oxygen-dependent proline hydroxylation of Hypoxia-inducible Factor Alpha	45	33	-1,9572	0,00197	0,03377
R-HSA-69202	Cyclin E associated events during G1/S transition	61	52	-2,0643	0	0,01808
R-HSA-5368286	Mitochondrial translation initiation	58	32	-2,1820	0,00195	0,00893
R-HSA-163200	Respiratory electron transport, ATP synthesis by chemiosmotic coupling, and heat production by uncoupling proteins,	46	27	-2,2507	0	0,00578
R-HSA-389661	Glyoxylate metabolism and glycine degradation	11	10	-2,3047	0	0,00408
R-HSA-162587	HIV Life Cycle	106	81	-2,4041	0,00208	0,00187
R-HSA-159231	Transport of Mature mRNA Derived from an Intronless Transcript	35	31	-2,7452	0	7,1E-05
R-HSA-180746	Nuclear import of Rev protein	29	22	-2,7516	0	7,2E-05
R-HSA-927802	Nonsense-Mediated Decay (NMD)	95	63	-2,7564	0	7,3E-05
R-HSA-975957	Nonsense Mediated Decay (NMD) enhanced by the Exon Junction Complex (EJC)	95	63	-2,7564	0	7,3E-05
R-HSA-180910	Vpr-mediated nuclear import of PICs	29	22	-2,7583	0	7,7E-05
R-HSA-4085377	SUMOylation of SUMOylation proteins	27	23	-2,7675	0	7,8E-05
R-HSA-168333	NEP/NS2 Interacts with the Cellular Export Machinery	27	26	-2,7767	0	8E-05
R-HSA-176033	Interactions of Vpr with host cellular proteins	32	26	-2,7881	0	6,4E-05
R-HSA-159234	Transport of Mature mRNAs Derived from Intronless Transcripts	36	32	-2,7925	0	6,6E-05
R-HSA-159230	Transport of the SLBP Dependant Mature mRNA	30	28	-2,8224	0	4,5E-05
R-HSA-168274	Export of Viral Ribonucleoproteins from Nucleus	28	27	-2,8315	0	4,6E-05
R-HSA-170822	Regulation of Glucokinase by Glucokinase Regulatory Protein	25	22	-2,8382	0	4,7E-05
R-HSA-177243	Interactions of Rev with host cellular proteins	32	30	-2,8659	0	4,8E-05
R-HSA-70326	Glucose metabolism	56	39	-2,8839	0	5E-05
R-HSA-8953854	Metabolism of RNA	536	390	-2,8976	0	5,1E-05
R-HSA-70171	Glycolysis	47	34	-2,9133	0	5,2E-05
R-HSA-6784531	tRNA processing in the nucleus	48	32	-2,9305	0	5,4E-05
R-HSA-162909	Host Interactions of HIV factors	97	74	-2,9754	0	5,6E-05
R-HSA-72306	tRNA processing	77	45	-2,9921	0	5,7E-05
R-HSA-1430728	Metabolism	642	378	-3,0306	0	5,9E-05
R-HSA-162906	HIV Infection	163	125	-3,0314	0	6,1E-05

R-HSA-72312	rRNA processing	172	141	-3,0539	0	3,2E-05
R-HSA-1643685	Disease	431	300	-3,0988	0	0
R-HSA-6791226	Major pathway of rRNA processing in the nucleolus and cytosol	156	130	-3,1198	0	0
R-HSA-390450	Folding of actin by CCT/TriC	8	8	-3,1671	0	0
R-HSA-8868773	rRNA processing in the nucleus and cytosol	165	138	-3,2500	0	0
R-HSA-9010553	Regulation of expression of SLITs and ROBOs	130	97	-3,4062	0	0
R-HSA-72649	Translation initiation complex formation	55	45	-3,4263	0	0
R-HSA-72662	Activation of the mRNA upon binding of the cap-binding complex and eIFs, and subsequent binding to 43S	55	45	-3,4263	0	0
R-HSA-72702	Ribosomal scanning and start codon recognition	55	45	-3,4442	0	0
R-HSA-72695	Formation of the ternary complex, and subsequently, the 43S complex	48	41	-3,4963	0	0
R-HSA-1799339	SRP-dependent cotranslational protein targeting to membrane	88	71	-3,5551	0	0
R-HSA-975956	Nonsense Mediated Decay (NMD) independent of the Exon Junction Complex (EJC)	78	63	-3,5751	0	0
R-HSA-156842	Eukaryotic Translation Elongation	77	63	-3,6228	0	0
R-HSA-192823	Viral mRNA Translation	73	57	-3,6359	0	0
R-HSA-2408557	Selenocysteine synthesis	74	58	-3,6493	0	0
R-HSA-156902	Peptide chain elongation	73	58	-3,7561	0	0
R-HSA-72764	Eukaryotic Translation Termination	74	59	-3,7928	0	0
R-HSA-168254	Influenza Infection	125	90	-3,8447	0	0
R-HSA-2408522	Selenoamino acid metabolism	93	71	-3,8720	0	0
R-HSA-5663205	Infectious disease	265	204	-3,8920	0	0
R-HSA-168255	Influenza Life Cycle	117	86	-3,9197	0	0
R-HSA-168273	Influenza Viral RNA Transcription and Replication	109	83	-4,1139	0	0
R-HSA-72766	Translation	226	151	-4,1307	0	0
R-HSA-71291	Metabolism of amino acids and derivatives	178	134	-4,1372	0	0
R-HSA-72613	Eukaryotic Translation Initiation	101	79	-4,1618	0	0
R-HSA-72737	Cap-dependent Translation Initiation	101	79	-4,1618	0	0
R-HSA-72706	GTP hydrolysis and joining of the 60S ribosomal subunit	96	81	-4,3037	0	0
R-HSA-156827	L13a-mediated translational silencing of Ceruloplasmin expression	95	77	-4,3605	0	0
R-HSA-72689	Formation of a pool of free 40S subunits	85	71	-4,4571	0	0

GLAD4U						
PA447172	Mitochondrial Diseases	153	89	-2,9815	0	0,00086
Disgenet						
C0030567	Parkinson Disease	12	12	-2,4787	0,00204	0,04888
C1836440	Increased serum lactate	31	26	-3,0848	0	0,00154

A *P*-value ≤ 0.05 was considered with adjustment using the Benjamini–Hochberg approach. Due to the extent of the GSEA enrichment data, the complete set of enriched proteins can be seen in https://drive.google.com/file/d/1bQumR96QB5H0y6e7oCoNu6nALWnxXfv0/view?usp=sharing.